INFORMATION TO USERS

8116985

PALMA, RUSSELL LUMIR

INERT GASES IN FIFTEEN IRON METEORITES

Rice University   PH.D.   1981

University
Microfilms
International 300 N. Zeeb Road, Ann Arbor, MI 48106

RICE UNIVERSITY

INERT GASES IN FIFTEEN IRON METEORITES

by

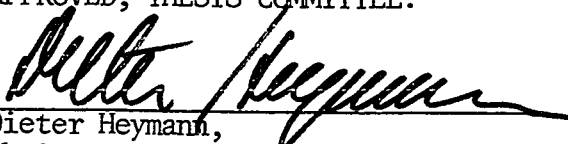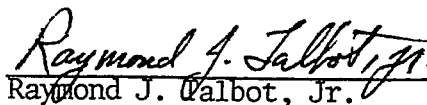Russell L. Palma

A THESIS SUBMITTED
IN PARTIAL FULFILLMENT OF THE
REQUIREMENTS FOR THE DEGREE

DOCTOR OF PHILOSOPHY

APPROVED, THESIS COMMITTEE:

Dieter Heymann,
Chairman, Department of Geology,
Professor of Geology and of Space
Physics and Astronomy
Chairman

Raymond J. Talbot, Jr.
Associate Professor of Space Physics
and Astronomy

Calvin M. Class
Professor of Physics

HOUSTON, TEXAS

July, 1980

ABSTRACT

Inert Gases in Fifteen Iron Meteorites

by

Russell L. Palma

The inert gases helium, neon, argon, krypton, and xenon were meas-
ured mass-spectrometrically in the metal phases of fifteen iron meteorites
and in graphite and troilite mineral separates from the Odessa iron mete-
orite. The meteorites analyzed were chosen because of their low cosmic
ray exposure ages; most had known exposure ages of less than 200 million
years. The hope was that the prominent spallation component seen in prior
iron meteorite inert gas measurements would be reduced enough to allow
detection of a trapped gas component, should one exist.

Approximately three gram samples were fused in a thoroughly out-
gassed alumina crucible. Surface contamination was removed from the sam-
ples by acid treatment and by preheating the samples for two days at 300
°C. Blank measurements were made for correction purposes before and after
each sample.

All of the meteorite samples show evidence of having a cosmogenic
inert gas component. Small variations attributable to different trace
element abundances and cosmic ray shielding are seen. Large deviations
from the predicted cosmogenic compositions correlate with short cosmic
ray exposure ages and often indicate the presence of a trapped atmospher-
ic-like inert gas component. Those samples showing anomalous behavior
in one inert gas tend to show anomalous behavior for all the inert gases.

The inert gas data from most samples are consistent with the heli-
um, neon, and argon concentrations being largely of cosmogenic origin and

the krypton and xenon resulting from a mix of solar wind, atmospheric, and cosmogenic compositions. However, there are several meteorites which are anomalous with respect to the above interpretation.

Krypton and xenon measurements had only been made in the metal phase of five iron meteorites, so determining the composition of those two gases was an important result of this work. The light krypton isotopes ^{78}Kr and ^{80}Kr are enriched in many samples relative to a mixture of atmospheric-solar wind and cosmogenic krypton. Prior investigations of xenon in iron meteorites had assumed only the presence of cosmogenic and atmospheric xenon, but the data from this study suggest that many xenon components may be trapped in the metal phase.

The Braunau inert gas data indicate strongly that this meteorite contains primordial trapped gas. Furthermore, the Braunau xenon composition includes the admixture of a xenon component not hitherto seen in any meteorite, stony or iron. This new component is marked by a low ^{128}Xe/^{132}Xe ratio.

The inert gases in the mineral separates from the Odessa iron meteorite also show contributions from spallation, but have distinctive components not seen in the metal phase. There are enrichments at ^{80}Kr, ^{82}Kr, and ^{83}Kr in the troilite phase which are consistent with neutron capture on ^{79}Br, ^{81}Br, and ^{82}Se, respectively, while a ^{129}Xe excess results from ^{129}I decay. A trapped gas component is strikingly evident in the neon and argon data from the graphite phase of Odessa.

ACKNOWLEDGEMENTS

INERT GASES IN FIFTEEN IRON METEORITES

Table of Contents

I. INTRODUCTION

Due to their spectacular mode of arrival on earth, meteorites have always been objects which have generated curiosity. The scientist's interest is piqued by the implications meteorites hold concerning the origin and evolution of the solar system. It is the intent of this work to uncover further clues from these objects, with the hope that it will better our understanding of this complex topic.

Meteorites are classified into three macroscopic groups: irons, stony-irons, and stones. These three broad classes are further broken into many finer divisions based on mineralogical and structural differences in the extraterrestrial material. Terrestrial samples have undergone extensive metamorphism during the earth's formation and subsequent evolution, but despite their wide ranging differences, chemical and isotopic studies of meteorites indicate that at least some of the classes have not developed beyond primitive stages. Thus meteoritic samples are well suited for investigations attempting to at least partially unravel the solar system's history.

The rare gases, helium, neon, argon, krypton, and xenon are of particular interest in these studies. Their indigenous concentrations are usually so low in meteorite samples that very small contributions from _in situ_ production processes may be detected. The chemical inertness of these elements simplifies their physical behavior and aids in their analysis, with the possibility of abundances being determined with high precision in samples of less than a tenth of a gram. This is

important since some extremely crucial meteorite classes consist of only a few members with little total mass.

For these reasons, the investigation of the inert gases in meteorites has produced an abundance of data. These data show that if the isotopic composition of the inert gases varies slightly from the terrestrial, solar or cosmic isotopic abundance ratios, they tend to follow predictable patterns caused by fairly well understood processes. However, anomalous concentrations and isotopic results have been discovered which do not fit these patterns. These results are crucial in that they may represent surviving records of an early solar system period from which modern theories and models of solar system formation may be derived.

A number of these isotopic anomalies in inert gases have been found in stony meteorites, in particular, in a special subclass called carbonaceous chondrites. The isotopic composition of the light rare gases, helium, neon, and argon, have also been examined in a large number of iron meteorites. The heavy inert gases, krypton and xenon, on the other hand, had only been studied in the metal phase of six iron meteorites prior to this work, and all five inert gases in only three of these. The object of this project was to determine the abundances and compositions of all five inert gases, but especially krypton and xenon, in a survey of iron meteorites of a number of different subclassifications.

One might wonder why krypton and xenon have not been measured in a greater number of iron meteorites. Due to iron meteorites being

highly differentiated, the theoretical prediction is that the concentrations of the heavy inert gases should be quite low, even if the parent object had had a significant concentration. This is true not only for krypton and xenon, but for the light inert gases as well. If there is gas in iron meteorites, it is most likely to be formed as a result of cosmic rays interacting with iron and nickel, since the gross composition of iron meteorites is about 90% iron and 10% nickel. Cosmic ray protons will form gas by spallation, but since the spallation products must be lighter than the target nucleus and krypton and xenon are heavier than iron, only the heavy trace elements in these meteorites will provide spallation targets for the production of those heavy inert gases. Thus the likelihood is that there will be little inert gas from any source, and that that does appear will be of normal cosmic ray composition. The low concentrations of krypton and xenon require melting large iron meteorite metal samples to get detectable amounts of gas. This involves considerable experimental difficulties.

On the positive side, iron meteorites are known to be much more difficult to outgas than are stony meteorites, so if they formed by melting under relatively large ambient gas pressures in a parent body, perhaps they would not be totally outgassed. Secondly, the few meteorites which have been examined were not the best candidates to show evidence for the isotopic anomalies detected elsewhere. In this study the meteorites were selected in general on the basis of low published cosmic ray exposure ages so that the gas produced from that source would be kept to a

minimum. Gas from spallation will tend to mask any other gas components, which are likely to be in low concentration if present at all.

By doing a large survey relative to that already published, it was hoped that perhaps one or two unusual meteorites might show up. A survey is unlikely to provide the precise data required to come to fundamental conclusions, but it can indicate those meteorites which deserve a more in-depth study.

Finally, the analysis made of mineral separates from the Odessa iron meteorite represents only the second time one investigator has done measurements of all five inert gases concurrently in metal, graphite, and troilite phases of a single iron meteorite. Compiling data from adjacent samples of different minerals can test formation theories of the iron meteorites themselves.

II. INSTRUMENTATION AND MEASUREMENT TECHNIQUES

A. Introduction

John Reynolds first described the design of a high sensitivity mass spectrometer for noble gas analysis (Reynolds, 1956). The instrument used for the present measurements was a Reynolds-type mass spectrometer with an all Pyrex glass vacuum envelope (Figure 1). Its small volume can be baked at temperatures of approximately 300-325 °C to attain the pressures necessary to measure extremely low abundances ($^{124, 126}$Xe as low as 6 x 10^{-15} cm^{3}STP/g in iron meteorite metal samples). Pressures as low as 2 x 10^{-11} mm Hg were obtained while the mass spectrometer was open to the ion pump. These pressures were measured with an ion gauge in the regulated mode. Electrons flowing from the gauge's filament ionized neutral atoms, and the resultant current to the grid is proportional to the system's pressure.

Briefly, the instrument operates in the following manner: neutral gas atoms which have been released from the sample by heating are ionized in the source region by bombardment with electrons from a filament. The ions are now collimated and accelerated by passing through a series of slits in parallel plates with a voltage drop. The resulting ion beam enters the field of an electromagnet where it is split due to the varying charge to mass ratio in the beam. Those ions whose charge to mass ratio is such that they will enter the analyzer slit impinge on an ion collector. The signal thus received is then amplified and recorded on a strip chart.

FIGURE CAPTION

Figure 1. Schematic diagram of the mass spectrometer and the sample
preparation line used for these analyses.

FIGURE 1

MASS SPECTROMETER

SAMPLE PREPARATION LINE
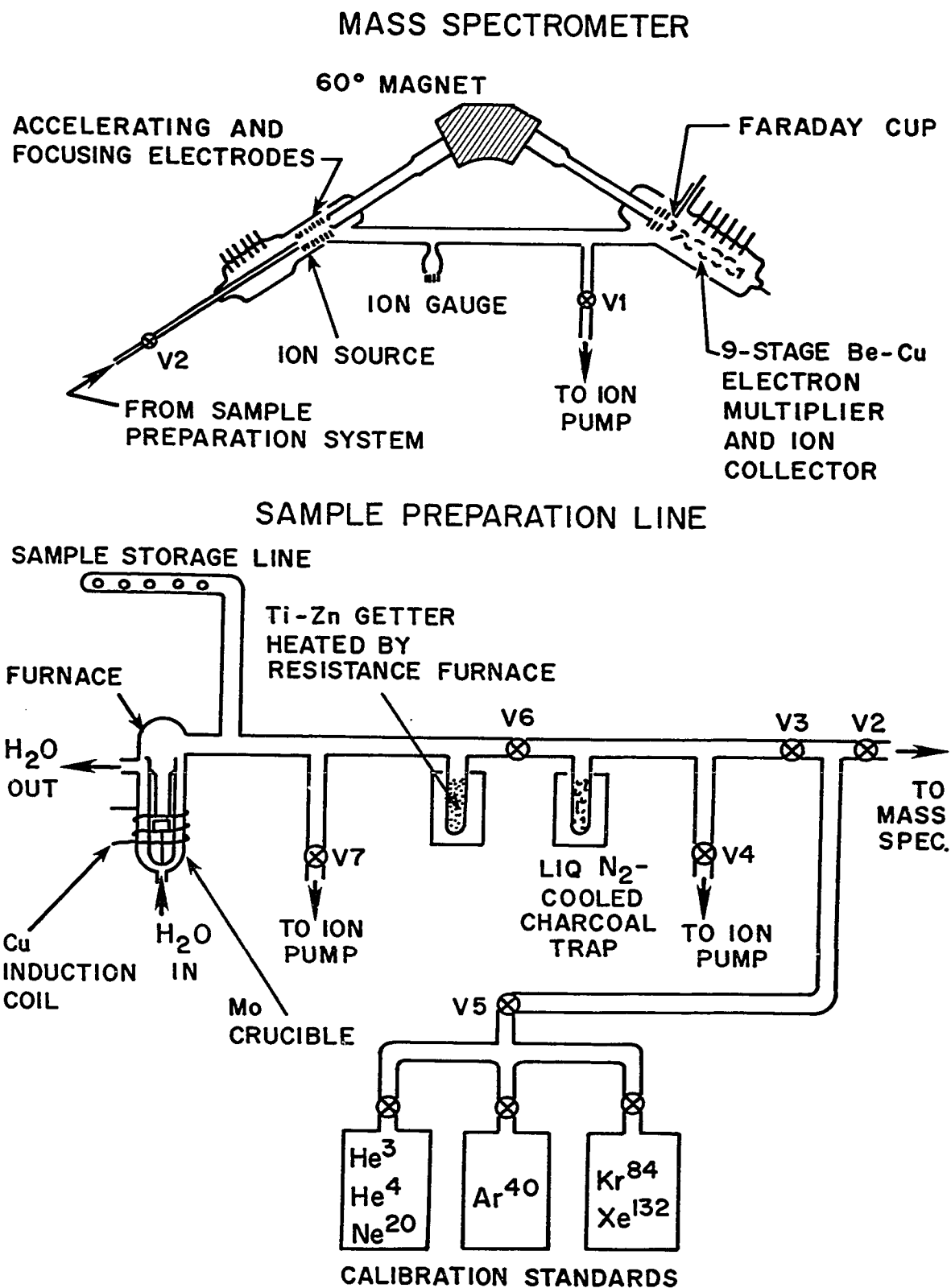
B. Focusing and Mass Separation Theory

If a charged particle enters a uniform magnetic field, and its motion is perpendicular to the direction of the field, it will be acted on by a force which is always at right angles to both the magnetic field and the direction of motion of the particle. When such a particle is traveling at a uniform velocity, this force will cause it to bend in a circular arc. By equating the centripetal force to that due to the magnetic field, one gets:

$$\frac{mv^2}{r} = qvB \qquad \qquad \text{II. (1)}$$

where   m = mass of the particle

v = velocity of the particle

r = radius of curvature of the circular arc

q = charge of the particle

B = magnetic field strength

This yields

$$v = \frac{Bqr}{m} \qquad \qquad \text{II. (2)}$$

The velocity with which the charged particle enters the magnetic field depends upon the voltage through which it has been accelerated in the ion source. The kinetic energy of the ion is equal to the electrostatic potential difference through which it has been accelerated, so that

$$\frac{1}{2}mv^2 = qV \qquad \qquad \text{II. (3)}$$

where m, q, v as before and V = accelerating potential ,

or

$$v = \frac{2qV}{m} \qquad\qquad \text{II. (4)}$$

Equating II. (2) and II. (4) and solving for q/m gives

$$\frac{q}{m} = \frac{2V}{B^2 r^2} \ . \qquad\qquad \text{II. (5)}$$

In a mass spectrometer r is the radius of curvature of the analyzer tube, which for the instrument used in these analyses is 4.5 inches. In the present measurements the accelerating voltage V was fixed at 2000 volts, and the magnetic field strength B was varied to let different values of q/m into the ion collector slit.

C. Detailed Description of Operation

The neutral gas to be measured enters the ionization chamber after the valve separating the sample prepline and the mass spectrometer is opened. The electron beam of the ion source is produced by electrons emitted from a tungsten filament. There is a potential difference of 75 volts between the filament and the ionization chamber walls called the electron voltage. The escaping electrons cause an emission current which is held constant by an emission regulator. The emission current can be preset manually at different values to increase the sensitivity of the mass spectrometer. For the iron meteorite metal samples the emission current used for krypton and xenon was ten times that used for the much more abundant helium, neon, and argon gases. The ion gauge acts as a safeguard for the filament while in the regulated mode in that if the pressure rises above 5×10^{-4} mm Hg in the gauge, the filament current is shut off to prevent oxidation.

The electron voltage was maintained at 75 volts for all measurements. For the inert gases, single ionization probabilities are much higher than for multiple ionization at this voltage. However, at certain masses the background abundances are high enough to warrant a correction factor. This is the case for masses 20 and 22, where double ionization of ^{40}Ar and CO_2 contributes to the ^{20}Ne and ^{22}Ne peaks, respectively.

After the ions are formed, they are accelerated and collimated by passing through a series of plates with slits. As noted before, in the present measurements this accelerating voltage was fixed at 2000 volts.

The 60° sector magnetic analyzer is an electromagnet with opposite poles on either side of the analyzer tube. A magnet regulator and power supply allow the field to be altered by varying the current through the magnet coils up to 250 milliamps. This current will produce a field of about 7000 gauss in the 7/16-inch gap between the poles. As seen from the mass spectrometer equation earlier [equation II. (5)], increasing the magnetic field strength increases the mass of the ions which will have the proper orbit to enter the ion collector. Also, as the field strength increases, the charge to mass ratios differ by less and less, making the resolution at higher masses more difficult.

In the ion collector the resolved beam passes through a defining slit and strikes the first plate of a nine stage electron multiplier with beryllium-copper dynodes. At the conversion dynode the ions produce secondary electrons which are focused and accelerated to the second dynode and so on through the nine stages. The interdynode potentials of approximately 200 volts are produced by passing a string current of about 40 microamperes through a series of 5 megaohm resistors. These potentials govern the amount of gain, magnifying the small ion current. The gain of the multiplier used is about 10^3.

The last dynode collects all the secondary electrons and the current passes to a vibrating reed electrometer. The emission of secondary electrons from the collecting dynode is suppressed 100% with an electrode at -45 volts relative to the potential of the collecting dynode. The vibrating reed electrometer derives its name from the input

signal modulator, which is a capacitor consisting of one stationary and one vibrating plate. The latter, called the reed, is moved through a predetermined distance by an electromagnet, at a constant frequency, to create a cyclically varying capacitor. The result is an alternating current output from the original direct current signal. The electrometer is capable of detecting currents as small as 10^{-15} amperes by measuring the potential difference across a high value input resistor. This input resistor's value was changed from 10^9 ohms for helium, neon, and argon, to 10^{12} ohms for greater sensitivity when measuring krypton and xenon. The potential difference across the input resistor is recorded on a strip chart for later readout.

D. Sample Preparation and Melting

The iron meteorite samples which were analyzed were obtained from a number of different sources (see Table 3). Unfortunately, none of the samples received from elsewhere were large enough or fortuitous enough to have large inclusions of graphite, troilite or silicate in them. However, in the laboratory there was already a large piece of the Odessa iron meteorite, and when it was cut in half, several large graphite and troilite inclusions were discovered.

The bulk of the measurements were done on the metal phase of the meteorites. These samples of approximately 2 to 4 grams were cut by hand with a hacksaw from the initial piece provided. The roughly 3 gram sample size was predicated by the few previous examples of heavy inert gas concentrations (especially the limiting isotopes of xenon, masses 124 and 126) in such material, the lower cosmic ray exposure ages of those meteorites being investigated here, and the practical limitations for melting in the present system (see below). The fusion crust was filed away from those samples on which it appeared. To remove surface contamination, the samples were placed in a solution of half concentrated nitric acid and half water in an ultrasonic cleaner for about 30 seconds. They were then placed in acetone in the ultrasound for about 30 seconds, weighed and stored in a vacuum dessicator.

The samples of graphite and troilite from the Odessa meteorite were obtained by slow, careful excavation of the individual inclusions. The troilite and graphite inclusions were often adjoining, which made

perfect separation virtually impossible. The material from the troilite inclusions was separated magnetically into two aliquots. The non-magnetic portion had a much greater percentage of graphite and impurities than did the magnetic sample. The graphite mined from the inclusions was washed in nitric acid to remove metal and troilite contamination. Another graphite sample was obtained by dissolving the sawings from the initial cut through the meteorite in a combination of hydrochloric and nitric acid. Since the cut passed through several graphite inclusions, the sawings contained a significant amount of graphite which was recovered.

The iron meteorite metal samples were loaded in a side arm of the preparation line as shown in Figure 1. Both the mass spectrometer and the sample preparation line have hoods which can be lowered over the glassware of the system. The glassware and samples can be baked out to remove contamination and background gases by means of variable transformers and heating elements under these hoods. The bakeout temperatures and durations were approximately 300 $^{\circ}$C for two days for the iron meteorite metal samples. In this time the pressure in the system was successively lowered by using first a mechanical fore pump and then a large charcoal trap at liquid nitrogen temperatures. When the pressure fell below 5 x 10^{-4} mm Hg, the charcoal trap was isolated from the system and the ion pump was turned on.

The graphite and troilite samples were put in a sample arm of the preparation line which was above the hood, since a significant

portion of their inert gases could be lost at temperatures of 300 ^{o}C over a two day period. Instead, the glassware enclosing these samples was wrapped with heating tapes and baked at approximately 100 ^{o}C for the two days.

The mass spectrometer did not require baking out as frequently as the preparation line since the valve connecting the two was closed before opening the system to air to load samples or make repairs. However, repairs on the filament and mass spectrometer did necessitate occasional bakeouts. This requires moving the magnet and the vibrating reed electrometer and readjusting them for the proper focus when operating pressures are again reached.

There are a number of experimental problems involved in the inert gas analysis of iron meteorite metal samples. First of all, the usual molybdenum crucibles used in the melting of lunar and stony meteorite samples cannot be used without modification. When one approaches the melting temperature of the metal (roughly 10% nickel, 90% iron), the metal will alloy with the crucible, and it will all melt. This is true for other types of metal crucibles as well. A number of alternate melting schemes were investigated. Since it is paramount to have extremely low background gas abundances, crucibles of graphite and other notoriously gassy possibilities must be discarded. The first alternative tested was the use of silica crucibles, which have the advantages of being readily available and the ability to be outgassed very well. Unfortunately, the silica crucibles always ruptured upon the remelting

of samples, no matter how carefully or cleverly the remelting was done
or the crucible was shaped. A second method examined was to coat the
inside of the molybdenum crucible with zirconium oxide. After slow
sintering this coating prevents alloy formation (Schultz et al., 1971)
with the molybdenum. However, this coating is very difficult to outgas
and, although successful for the 50-100 milligram samples needed by
Schultz et al., dropping 3 gram iron meteorite samples into the crucible
caused the protective coating to flake off.

The classic technique used in most cases to investigate the
light noble gases in iron meteorites is to use an alumina crucible in-
side of a molybdenum crucible. The 10 milliliter Coors alumina crucible
used for the present analyses can withstand temperatures of 1900 $^{\circ}$C, but
its drawback is again the difficulty in outgassing. This is of much
greater importance in the study of krypton and xenon than in helium,
neon, and argon and the only solution seemed to be extremely long out-
gassing times at temperatures above the melting point of the metal.
Heating at about 1800 $^{\circ}$C for approximately 50 hours brought down the
background blank gas values, but also brought up another serious experi-
mental problem: The high temperatures required for thorough outgassing
of the crucible and samples.

Quite a number of furnace designs were tried. The two main dif-
ficulties are the prolonged heating at high temperature and the large
sample size required due to the low gas concentrations. Even after the
crucible is well outgassed, a sample requires heating to at least

1600 ^{O}C for it to be totally fused. Since the furnace is glass, this places a large strain on the system. The vacuum in the instrument will pull on the glass when it becomes hot enough to flow. The two most successful furnace designs are shown in Figures 2 and 3. These represent the end result of months of experimentation and innumerable failures. The inner sleeves surrounding the crucible and supporting it in Figure 2 are made of quartz Vycor glass, which is necessary at these temperatures and protects the exterior vacuum envelope. The exterior is also Vycor in the region of the external radio frequency heating element (see below), but grades into Pyrex for easier reworking and sample loading. The water cooling cup helps lower the glass temperatures below the coil. The samples are guided by a magnet until directly above the crucible at the top of the furnace and then released.

The furnace in Figure 2, while successful for a number of samples, did not fully solve the heat problem and did not begin to deal with the problem of the large sample size. The samples, when fused, coated the exterior walls of the furnace with metal. In addition to this metal heating the exterior walls, it built up after just two or three samples to the point where new samples could not get through to the crucible. There is a difficult trade off here: if one protects the exterior wall of the furnace by extending the inner sleeve higher, then the volume to which the metal can be deposited is lessened, making it impossible to do many samples before clogging the furnace. This problem is obviated in analyses of only helium, neon and argon, because

FIGURE CAPTIONS

FIGURE 2. Schematic diagram of the furnace melting system used initially for iron meteorite metal samples.

FIGURE 3. Schematic diagram of the final and most successful furnace melting system used for iron meteorite metal samples.

FIGURE 4. Schematic diagram of the furnace melting system used for the mineral separate samples from the Odessa meteorite.

FIGURE 2   19

TO SAMPLE LOADING
& PREPARATION LINES

PYREX

QUARTZ VYCOR
TO PYREX GLASS
GRADED SEAL

VYCOR

ALUMINA CRUCIBLE

COPPER
INDUCTION
HEATING
COIL

MOLYBDENUM
CRUCIBLE

H_2O
OUT

QUARTZ VYCOR
PROTECTIVE SLEEVES

WATER COOLING CUP

H_2O IN
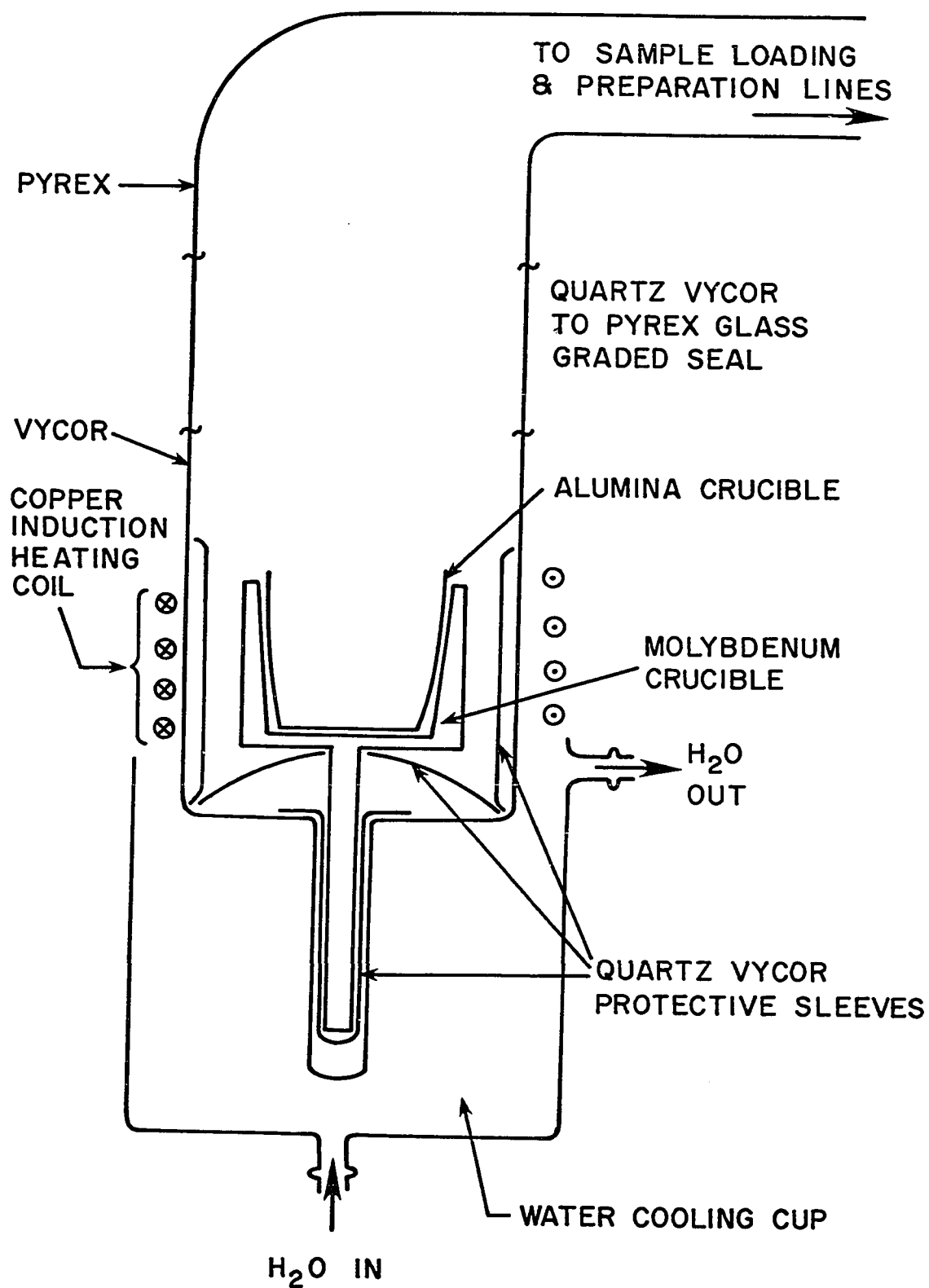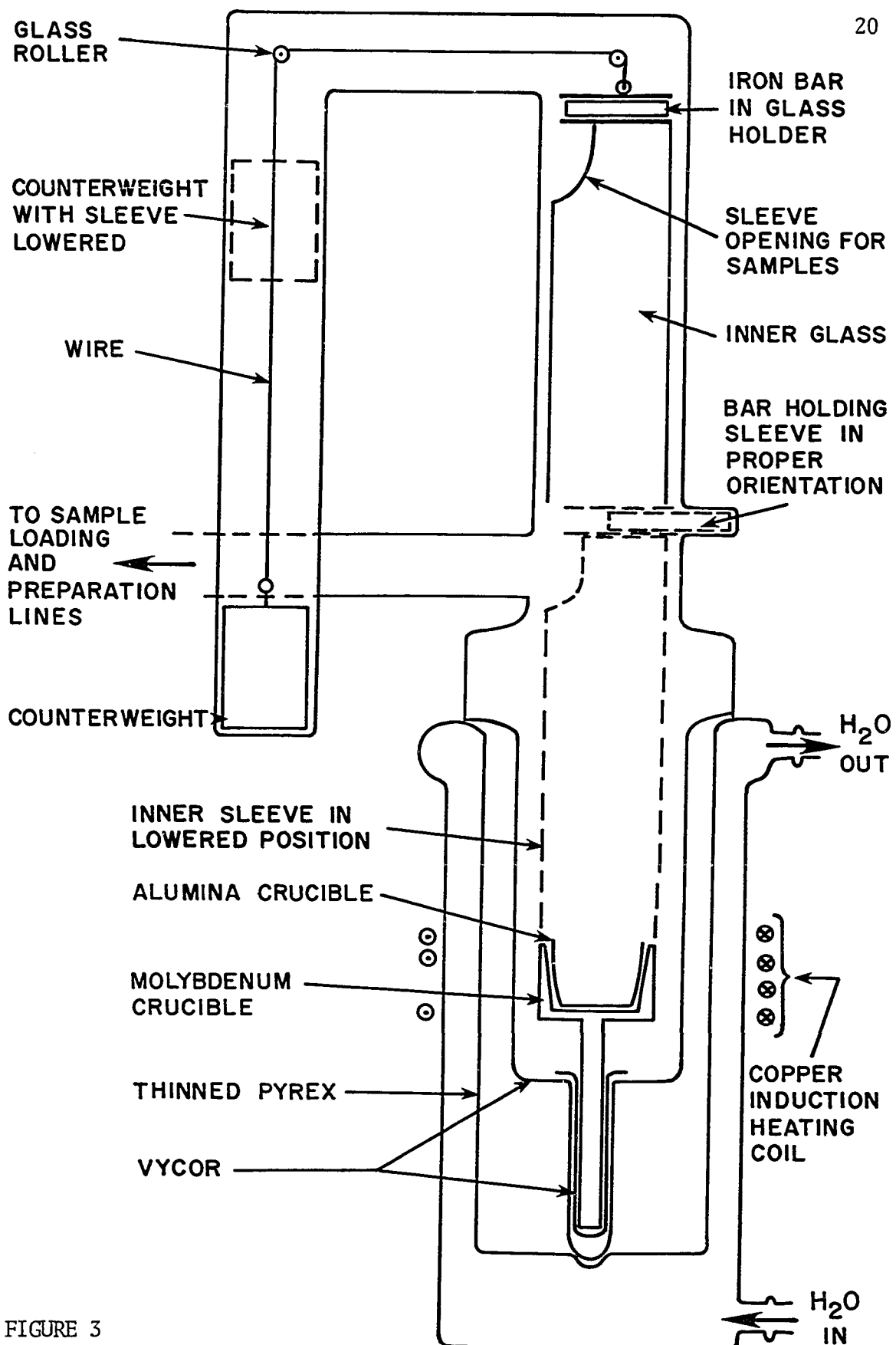
FIGURE 3

FIGURE 4
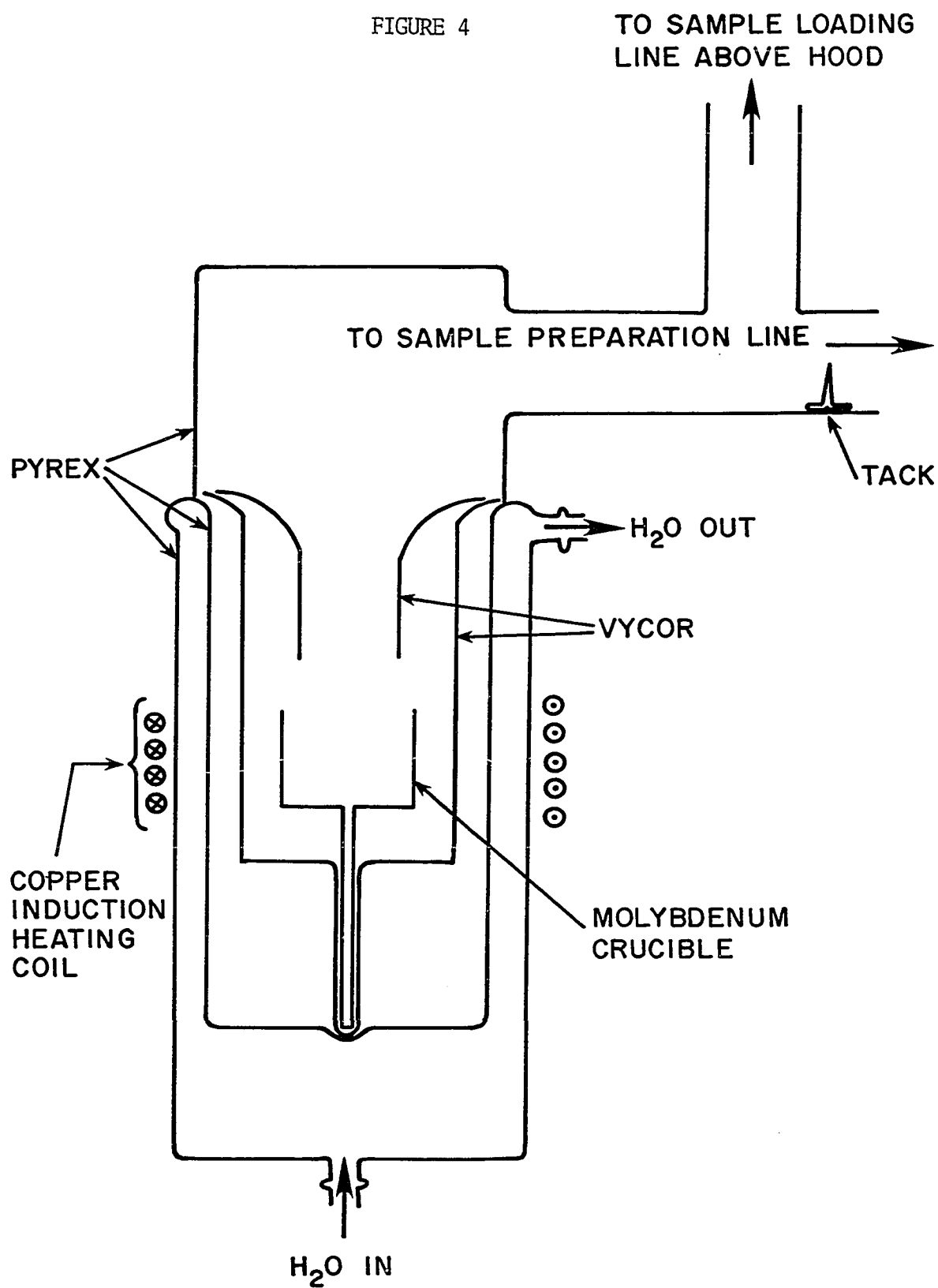
samples of only about 200 milligrams are needed (e.g.; Fisher and Schaeffer, 1960; Voshage and Feldman, 1978). It also happened that some of the samples did not land directly in the alumina crucible, which was unobservable due to the deposited metal. Some of these samples rested on the lip of the alumina crucible and upon melting alloyed with the molybdenum, while others were only partially outgassed.

An attempt to solve these problems and better deal with the high temperatures is shown in Figure 3. Here, to combat the heat problem, the water cooling jacket extends throughout the entire heating region. Since the jacket is a closed loop, more water can be forced through the system to provide better cooling. Also, the inside wall of the cooling jacket has been thinned so that the temperature gradient across the glass is lessened, again improving cooling efficiency. It is possible with this design to build the entire furnace from Pyrex glass except for the quartz Vycor holder in which the crucible rests. Besides reducing cost and simplifying reworking, this eliminates the need for graded seals from Pyrex to Vycor, which were a continual source of glass failures and leaks.

In an effort to reduce the uncertainty of the samples making it to the crucible, a sliding sleeve with a counterweight was added. By raising the weight with a magnet, the sleeve was lowered until it rested on the crucible. A small bar on top of the sleeve could be manipulated with the magnet so that the opening at the top of the sleeve corresponded to the opening from the sample loading line. Once the sample was

guided to the top of the sleeve by the magnet, it was constrained to fall in the alumina crucible.

This design solved many of the difficulties associated with the large samples, but there was still the unavoidable buildup of residue from the fused samples. However, with the sleeve as a guide, the sample was prevented from being caught in the residue as some of the previous samples had been when simply dropped from above the crucible. Also, lowering the sleeve acted as a sort of "battering ram" which kept the residue restricted to the wall of the crucible holder. Nevertheless, after approximately six samples it was necessary to open the system and clean it out, due not only to the fused residue, but also because the background gas levels began to seriously interfere with the accuracy of the measurements at this point.

Although the effectiveness of this design in improving cooling and reliability cannot be overemphasized, it does have the drawback of increasing the distance from the radio frequency heating element to the crucible and sample. This increased distance reduces coupling, which necessitated a coil with a greater number of turns and required increasing the output from the power supply to fuse the samples. Also, the glassblowing expertise required to build a furnace of this design is considerable.

For the graphite and troilite samples the problem of alloy formation with the crucible does not apply. Because of this, the furnace design and system set up used for lunar sample analysis could be

adopted. In these instances the alumina inner crucible was not required. Without this inner crucible, the molybdenum crucible could be built with a smaller diameter. This reduces the total diameter of the furnace and thus a smaller induction heating coil and less power are needed. More important, however, is that outgassing was much easier with so much less molybdenum and no alumina to trap gas. This furnace design is shown in Figure 4.

The graphite and troilite samples had much greater concentrations of the inert gases (see Table 3), so their sample size was on the order of 90 milligrams. Since these samples involve loose material, they were wrapped in small pieces of aluminum foil. The aluminum foil is known to have negligible amounts of the inert gases. These samples could not be maneuvered about directly with a magnet as could the iron meteorite metal samples, so two tacks were also loaded with the samples. The tack in the sample loading line above the hood could be moved to direct the samples down near the crucible. The other tack was used at this point to push the sample into the molybdenum crucible. A Vycor "funnel", similar to the one in Figure 4, cannot be used to direct the metal samples because the bottom opening would rapidly become clogged with fused residue.

Once the sample had been put in the crucible, it was fused, and the gas released, by radio frequency heating with an external coil. An alternating current passes through the copper coil surrounding the furnace. This current has an alternating magnetic field associated

with it from Ampere's circuital law. From Faraday's induction law this changing magnetic field induces an electric field in the region of a conductor, here both the molybdenum crucible and the iron meteorite sample itself. The electric field induced sets conduction electrons in motion, generating heat by eddy currents. The crucible was heated to approximately 1700 $^{\circ}$C for fifteen minutes. In the cases where it was possible to see the sample melt, melting was completed within six minutes. Maintaining the maximum temperature for fifteen minutes was done only as a precaution to insure that the sample was entirely fused. During the heating phase, the gas was exposed to a titanium-zirconium getter heated by a resistance furnace to about 900 $^{\circ}$C. The Ti-Zr getter removes hydrocarbons and other contaminants by reacting with them.

Following the heating, the gas was allowed to equilibrate for ten minutes while the radio frequency power supply cooled down. At this point the evolved gas was confined to a small portion of the sample preparation line by two high vacuum valves, one to the ion pump and the other to the remainder of the system. At the end of the ten minutes the resistance furnace around the Ti-Zr getter was turned off, and hydrogen removed from the system by being absorbed into the Ti-Zr alloy. Immediately after turning off the resistance furnace, a Dewar with liquid nitrogen was placed around a charcoal trap and the valve to the remainder of the preparation line opened. The system was now filled for the most part with the inert gases helium, neon, argon, krypton, and xenon from the sample and small background amounts of these and other gases.

A charcoal trap acts as a very efficient absorber of the heavy inert gases argon, krypton, and xenon at the liquid nitrogen temperature of -180 $^{\circ}$C. After a period of 45 minutes these gases were frozen onto the charcoal and measurements of the helium and neon isotopes could begin.

E.   Inert Gas Measurements

The mass spectrometer was closed off from the sample prepara-
tion line and open to the ion pump prior to admitting the helium and
neon portions of the sample. To determine the rate at which ^{4}He dif-
fuses through the glass walls of the mass spectrometer during a meas-
urement, the linear increase of ^{4}He was monitored for approximately
five minutes with the mass spectrometer isolated (both the valves to
the sample preparation line and the ion pump closed). The amount of
^{4}He in the sample was later adjusted by subtracting the diffusion com-
ponent and the value of ^{4}He when the sample was admitted. These and
other corrections were incorporated into the computerized data reduc-
tion program.

The mass spectrometer was operated in the static mode where the
valve to the ion pump was left closed during the sample analysis. The
ion gauge grid was floated after the ion pump was closed off from the
system to prevent pumping effects from ion implantation into the glass
walls.

1)   Helium and Neon

While on the ^{4}He peak due solely to diffusion, the valve between
the sample prepline and the mass spectrometer was opened to admit the
helium and neon gas from the sample. The millivolt signals of ^{3}He, ^{4}He,
^{20}Ne, ^{21}Ne and ^{22}Ne were measured following the equilibration of the gases in
the mass spectrometer. At least six peaks of each mass were recorded,

usually in two groups of three, where the two groups of three were sep-
arated by a significant time interval. These time-peak height data sets
allow the signal to be extrapolated back to the time at which the gas
was admitted into the mass spectrometer.

Peaks of three other masses were also measured since they con-
stitute corrections to the peaks of the inert gas isotopes. These
masses were 18, 40, and 44. Mass 18 is predominantly $H_2^{16}O$, and assum-
ing $H_2^{16}O/H_2^{18}O$ is equal to the isotopic ratio $^{16}O/^{18}O$ of approximately
1/500, then 1/500 of the 18 peak equals the amount of $H_2^{18}O$ which will
contribute to the mass 20 peak. Also contributing to the 20 peak is
doubly ionized ^{40}Ar. Although most of the ^{40}Ar will have been absorbed
on the charcoal at liquid nitrogen temperatures, a small equilibrium
amount will appear in the system. It has been experimentally determined
that for this mass spectrometer $^{40}Ar^{++}/^{40}Ar^{+}$ is approximately 1/6, so
that 1/6 of the mass 40 peak will appear at mass 20. A small amount of
mass 44, essentially all CO_2, also appears in the system during the
helium and neon measurements. In the mass spectrometer it has been
found that CO_2^{++}/CO_2^{+} is approximately 1/70, so that 1/70 of the mass 44
peak will appear at mass 22.

The contributions to the ^{20}Ne and ^{22}Ne peak heights due to the
concentrations of masses 18 and 44 were always less than 0.1% of the
total ^{20}Ne and ^{22}Ne abundances, respectively. The correction of ^{20}Ne
due to ^{40}Ar was usually less than 5% of the ^{20}Ne concentration.

2) Argon, Krypton, and Xenon

After measuring the helium and neon isotopes and those masses required for corrections, the valve between the sample preparation line and the mass spectrometer was closed and the valve to the ion pump was opened. The liquid nitrogen was taken from the charcoal trap and replaced by hot water (about 60 $^{\circ}$C) so that while the mass spectrometer was evacuated, the heavier inert gases argon, krypton, and xenon equilibrated in the sample prepline.

After waiting thirty minutes, the valve from the mass spectrometer to the ion pump was closed, mass 40 was found to record the very small amount of background ^{40}Ar still remaining in the mass spectrometer, and the valve from the sample preparation line was opened to admit the argon, krypton, and xenon isotopes. Argon isotopes ^{36}Ar, ^{38}Ar, and ^{40}Ar were measured in the same manner as the helium and neon isotopes were, following the equilibration of argon in the system.

Both the input resistor and the emission current were increased to the levels discussed earlier following the completion of the argon measurements. After allowing ten minutes for the system to equilibrate, peaks of krypton isotopes ^{78}Kr, ^{80}Kr, ^{82}Kr, ^{83}Kr, ^{84}Kr, and ^{86}Kr and xenon isotopes ^{124}Xe, ^{126}Xe, ^{128}Xe, ^{129}Xe, ^{130}Xe, ^{131}Xe, ^{132}Xe, ^{134}Xe, and ^{136}Xe were recorded.

This procedure was followed for all the iron meteorite metal samples. However, for the Odessa mineral separate samples of graphite and troilite, the krypton and xenon gas concentrations were such that

even with the much smaller sample size, increasing the emission current was no longer necessary. The input resistor was still increased from 10^9 to 10^{12} ohms.

3) Blank Runs and Calibrations

The mass spectrometer and the sample preparation line always contain a small amount of background gas from previous samples or gas trapped in the crucible or glass. Before each sample run this gas was analyzed by performing blank runs where all procedures were exactly the same, except that no sample was admitted to the crucible. This background signal must be subtracted from the total signal found during the sample measurements. For some rare gas isotopes, such as ^{3}He, the background gas was completely negligible in the present analyses, but for isotopes such as ^{78}Kr, where hydrocarbon interference often constitutes well over 90% of the signal, the background gas measurements were crucial.

To obtain the inert gas concentrations in the samples in the units of cm^3STP/gram, the sensitivity of the mass spectrometer must be determined in units of millivolts/cm^3STP. This was done by admitting accurately known amounts of ^{3}He, ^{4}He, ^{20}Ne, ^{40}Ar, ^{84}Kr, and ^{132}Xe to the system and measuring the resulting signal. The gases were introduced to pipettes in the calibration standards (see Figure 1), then released to the entire system. The volumes and typical sensitivities used are listed in Table 1.

TABLE 1

Mass	Standard Volume (cm^3 STP)	Sensitivity (mv/cm^{3}STP) Iron Samples	Mineral Separate Samples
^{3}He	8.943 x 10^{-8}	7.463 x 10^8	7.674 x 10^8
^{4}He	3.166 x 10^{-7}	7.173 x 10^8	7.506 x 10^8
^{20}Ne	1.150 x 10^{-7}	1.194 x 10^9	1.230 x 10^9
^{40}Ar	2.475 x 10^{-7}	4.236 x 10^9	4.484 x 10^9
^{84}Kr	8.390 x 10^{-10}	4.266 x 10^{13}	6.715 x 10^{12}
^{132}Xe	3.940 x 10^{-10}	4.555 x 10^{13}	7.070 x 10^{12}

Due to design alterations, calibration runs were done for each set of samples analyzed with the instrument in a particular configuration, so that the sensitivities varied slightly. A small volume correction factor was also required due to having the valve to the standards open during a calibration measurement, whereas during sample and blank runs it is not. Masses 21 and 22 are measured less sensitively than mass 20 due to mass fractionation, so the sensitivities of these masses were obtained by dividing the sensitivity of mass 20 by experimentally determined fractionation factors: 1.005 for mass 21 and 1.01 for mass 22. It was determined experimentally that for the isotopes of argon, krypton, and xenon, fractionation factors were not required, so that the sensitivity of the one isotope measured of each served as the sensitivity for all the isotopes of that gas.

As a final correction, a broad background peak at mass 80 was observed when large amounts of argon were introduced into the mass spectrometer. This background peak could either be due to Ar_2^+ molecules or to charge exchange ($Ar^{++} \rightarrow Ar^+$) between the ion source and the magnetic analyzer. This background interference was only significant when the total gas concentration (blank plus sample) of the ^{40}Ar peak exceeded about 4×10^{-7} cm^3 STP. This was true for seven of the fifteen meteorites analyzed: Arispe, Bohumiltz, Butler, Cedartown, Dayton, Sierra Gorda, and Tawallah Valley.

To calculate the adjustment necessary to correct for this addition to the ^{80}Kr peak, accurately known amounts of ^{40}Ar were released into the mass spectrometer from the calibration reservoirs while monitoring the mass 80 peak height. A plot of the ^{40}Ar concentration versus the mass 80 peak height yielded the following second order correction equation:

$$^{80}Kr_{correction} \text{ (mv)} = 6.8818 - 2.3636 \times 10^{-4} \ [^{40}Ar_{peak\ height} \text{ (mv)}]$$
$$+ 3.2 \times 10^{-6} \ [^{40}Ar_{peak\ height} \text{ (mv)}]^2 \qquad \text{II. (6)}$$

This correction factor was determined using the total signal from mass 40, so that the final ^{80}Kr signal from the sample equaled the total mass 80 signal minus the correction factor minus the blank mass 80 signal.

This correction was done on all the samples, but only on the seven meteorites listed did it alter the ^{80}Kr concentration appreciably.

Despite this correction, the combination of a large ^{40}Ar peak and a large ^{80}Kr peak in the Arispe, Bohumiltz, and Dayton iron meteorite samples make their final ^{80}Kr concentrations questionable. In these three cases the very broad background interference made the peak height determinations difficult. Because of this, calculations and results using the ^{80}Kr concentrations are marked with an asterisk in the data tables for these meteorites.

To give some idea of the relative concentrations of the inert gases in a blank versus a sample, a comparison of the two is shown in Table 2 for the Babb's Mill meteorite. The Babb's Mill iron sample was chosen as an example because it has relatively low inert gas concentrations (see also Table 3). As a result, the percentage of the net sample signal (column 3) that the blank concentration in column 2 represents is nearly the maximum value seen for any of the analyzed samples.

The background gas played the largest role by far in the case of ^{78}Kr, as mentioned earlier. The hydrocarbon background gas from C_6H_6 constituted at least 70% of the total signal, and often the contribution was over 90%. The C_6H_6 problem is not uniquely restricted to the mass spectrometer used for the present analyses, but is a widespread bane of krypton measurements in mass spectrometry. The benzene molecule is very easily formed from C- and H- containing compounds in the ion source. The only technique to successfully deal with this problem is high resolution mass spectrometry.

TABLE 2

COMPARISON OF BLANK TO SAMPLE SIGNAL

FOR THE BABB'S MILL METEORITE

Mass	Blank Concentration (cm^3 STP)	% of Net Sample Signal
^{3}He	6.31×10^{-9}	1.6
^{4}He	1.82×10^{-7}	10.0
^{20}Ne	7.00×10^{-9}	25.0
^{21}Ne	7.69×10^{-11}	1.9
^{22}Ne	7.74×10^{-10}	14.0
^{36}Ar	8.74×10^{-10}	6.7
^{38}Ar	5.72×10^{-10}	3.9
^{40}Ar	1.61×10^{-7}	13.0
^{78}Kr	1.41×10^{-11}	96.0
^{80}Kr	5.59×10^{-13}	20.0
^{82}Kr	1.73×10^{-12}	11.0
^{83}Kr	1.53×10^{-12}	10.0
^{84}Kr	7.48×10^{-12}	10.0
^{86}Kr	2.26×10^{-12}	10.0
^{124}Xe	9.39×10^{-15}	6.9
^{126}Xe	9.32×10^{-15}	4.7
^{128}Xe	1.84×10^{-13}	8.2

TABLE 2

(Continuation)

Mass	Blank Concentration (cm^3 STP)	% of Net Sample Signal
^{129}Xe	1.19×10^{-12}	3.9
^{130}Xe	2.21×10^{-13}	5.1
^{131}Xe	1.01×10^{-12}	4.1
^{132}Xe	1.40×10^{-12}	4.5
^{134}Xe	5.25×10^{-13}	4.2
^{136}Xe	4.69×10^{-13}	4.4

The correction for blank concentrations was next most signifi-
cant in the case of ^{20}Ne, where the atmospheric background is large and
the spallation produced gas is relatively small. This correction was
usually on the order of 20 to 25% of the total signal. ^{22}Ne, ^{40}Ar, and
^{80}Kr have blank concentrations ranging from 10 to 20% of the total sig-
nal, while ^{4}He, ^{82}Kr, ^{83}Kr, ^{84}Kr, and ^{86}Kr were approximately 5 to 10%.
For ^{36}Ar, ^{38}Ar and all the xenon isotopes, the background gas repre-
sented less than 5% of the total signal, while the strongly cosmic ray
produced nuclides, ^{3}He and ^{21}Ne, rarely had corrections of more than
1 or 2%.

F. Calculations and Error Analysis

The height of the peaks of each mass were measured, as was the time at which the measurement was made after the gas had been initially admitted to the mass spectrometer (time = 0). These time-peak height data sets, combined with the range of the signal in millivolts, allow a linear least squares fit to be performed. The net signal in millivolts for a given mass in a blank run is obtained by the extrapolation of the mass's least squares line to the time $t = 0$, minus all corrections due to interfering non-inert gas contributions or diffusion through the glass in the case of ^{4}He. The error in an isotope's signal in a blank run is due to the linear least squares fit, and one standard deviation is the error quoted for the signal.

Generally speaking, there are the following sources of noise in the measurements: 1) ionization fluctuations in the ion source, 2) instabilities in the accelerating voltage and the magnet current, 3) the multiplier, 4) the preamplification portion of the electrometer, and 5) the main amplification system and the strip-chart recorder. Studies of these sources have shown that 90% or more of the noise comes from the multiplier and the resistor of the electrometer. The multiplier was therefore operated well below its maximum gain. From the point of view of peak-to-noise ratio, the best way of increasing the sensitivity of this mass spectrometer is to increase the emission current of the ion source, but this has the disadvantage of reducing the filament's lifetime. As a compromise, the emission current was increased somewhat, but most

of the increased sensitivity was obtained by increasing the electro-meter's resistor.

In a calibration, one seeks the sensitivity in millivolts/cm^3STP. The millivolt signal and its error are determined as for a mass in a blank run. The standard's volume, the volume of the pipette to which the standard is admitted before it is released into the prepline and mass spectrometer, has an error of 1%. The error in the sensitivity therefore combines these errors by the suitable propagation of error formula. The resulting errors in the sensitivities at each mass are actually one standard deviation upper limits since the different sources of error are assumed to be uncorrelated.

Finally, the gas concentration of the sample is obtained for each isotope by:

$$\text{gas concentration } (\frac{cm^3 STP}{g}) = \frac{[mv \text{ signal (sample)} - mv \text{ signal (blank)}]}{\text{sensitivity } (\frac{mv}{cm^3 STP}) \times \text{ sample weight (g)}} .$$

$$\text{II. (7)}$$

The error in the millivolt signal of an isotope in the sample is found as for those in the blanks. Instrumental (i.e. balance) uncertainties provide the error in the sample weight. The error in the gas concentration is found by again combining all errors using the propagation of error technique and assuming uncorrelated sources of error.

It is often useful in the study of inert gases in meteorites to determine various isotopic ratios. These ratios are reproduced in

Tables 3 through 7, and their error properly combines the errors in the individual gas concentrations of the isotopes involved.

III. RESULTS

The data from these experiments are presented in Tables 3
through 7. In Table 3 an alphabetical meteorite-by-meteorite compila-
tion of data is made. First the sample number and source are cited.
The structural and chemical classifications of the meteorites are from
the Handbook of Iron Meteorites (Buchwald, 1975), and the various de-
terminations of the cosmic ray exposure age are as referenced. Also
listed is the sample mass fused during the experimental procedure.
Tabulated in units of cm^3STP/g is the concentration of one isotope of
each of the five inert gases, and with them are the isotopic ratios of
interest. Besides the error estimates, determined as reported in the
previous section (II. F.), the data from all prior inert gas investiga-
tions on each of the individual meteorites are also listed. These com-
parison data are found only for the light inert gases helium, neon, and
argon since the present experiments yielded the first krypton and xenon
data for any of these meteorites as far as metal samples are concerned.
The data obtained from the various graphite and troilite samples mined
from the Odessa inclusions, and recovered from sawings, are also pre-
sented following the Odessa metal sample results.

In Table 4 the helium, neon, and argon isotopic ratios are com-
piled for each of the fifteen meteorites analyzed in this work, the five
iron meteorites for which prior krypton and zenon data were available,
and cosmic ray spallation, solar wind, and atmospheric values. The data
for the Costilla Peak meteorite are from Munk (1967a), Carbo and Misteca

from Munk (1967b), and Xiquipilco and Cape York from Hennecke and Manuel (1977). The atmospheric ratios are taken from Eberhardt et al. (1965) and Nier (1950), and the solar wind data are from Eberhardt et al. (1970). The spallation values are averages of prior inert gas measurements in iron meteorites that investigators reported as having "normal" cosmic ray produced isotopic ratios. For the $^4He/^3He$ ratio this involved averaging 173 measurements; $^{20}Ne/^{22}Ne$ and $^{21}Ne/^{22}Ne$, 127 measurements; $^{36}Ar/^{38}Ar$, 91 measurements (Fisher and Schaeffer, 1960; Signer and Nier, 1962; Bauer, 1963; Hintenberger and Wänke, 1964; Lipschutz et al., 1965; Munk, 1967a,b; Schultz and Hintenberger, 1967; Hintenberger et al., 1967; Hennecke and Manuel, 1977; Voshage and Feldman, 1978).

In Tables 5 and 6 the krypton and xenon isotopic ratios are compiled for the same meteorites as in Table 4, respectively. Here the atmospheric values for krypton are from Hennecke and Manuel (1977), and the solar wind spectrum is from Eberhardt et al. (1970). The spallation values were calculated by Munk (1967b) and will be discussed further in section IV. C. The errors in the isotopic ratios are not reproduced in Tables 4 through 6 for clarity and compactness. Those error measurements are listed with the individual results for each meteorite in Table 3. As discussed in section II. E., the ^{80}Kr concentrations in Arispe, Bohumiltz, and Dayton are questionable, and the $^{80}Kr/^{84}Kr$ ratios for these meteorites are therefore marked with an asterisk in Tables 3 and 5.

Table 7 presents the inert gas isotopic ratios in the three different phases measured (metal, graphite and troilite) of the Odessa

meteorite. The data from the non-magnetic "troilite" aliquot was not included in the table since it had a much greater percentage of impurities in it. Also, the analysis of the graphite recovered from dissolving sawings was excluded for reasons which will be discussed in section IV. E. Again, the errors in the isotopic ratios may be found by refering to Table 3.

Also listed in Table 7 is the data from the metal, graphite, and troilite phases of the Deelfontein iron meteorite (Fireman and DeFelice, 1968), the only other meteorite to have been so analyzed. The authors listed no krypton concentrations for the metal and the graphite phases of Deelfontein, and reported the ratios only as being atmospheric within 10%.

TABLE 3

METEORITE: Arispe

SAMPLE SOURCE: Dieter Heymann, Rice University, Houston, Texas.

CLASSIFICATION: Structural—Coarse Octahedrite; Chemical—Anomalous.

COSMIC RAY EXPOSURE AGE (10^6 years): 350 ± 50, Fisher and Schaeffer (1960); 440 ± 30, Vilcsek and Wänke (1962); 905 ± 90, Voshage (1967).

FUSED SAMPLE MASS: 3.64350 ± 0.00041 grams

Concentrations in cm^3STP/g

	^3He	$\dfrac{^4He}{^3He}$	^{20}Ne	$\dfrac{^4He}{^{20}Ne}$	$\dfrac{^{20}Ne}{^{22}Ne}$	$\dfrac{^{21}Ne}{^{22}Ne}$	^{36}Ar	$\dfrac{^{20}Ne}{^{36}Ar}$	$\dfrac{^{36}Ar}{^{38}Ar}$	$\dfrac{^{40}Ar}{^{36}Ar}$	$\dfrac{^{40}Ar}{^{38}Ar}$
A	$(1.281 \pm .014)x10^{-6}$	$3.355 \pm .066$	$(1.780 \pm .037)x10^{-8}$	241.4 ± 6.4	$1.085 \pm .031$	$0.982 \pm .028$	$(5.521 \pm .057)x10^{-8}$	$0.3224 \pm .0075$	$0.6600 \pm .0096$	$2.446 \pm .036$	$1.613 \pm .024$
B	$1.96x10^{-6}$	3.83	$1.97x10^{-8}$	381	0.939	0.948	—	—	—	—	—
C	$2.70x10^{-6}$	3.45	2.3×10^{-8}	404	1.0	1.0	$5.5x10^{-8}$	0.418	0.618	2.49	1.54
D	$9.77x10^{-7}$	4.37	$[^{21}Ne]$ $1.13x10^{-8}$	—	—	—	$3.47x10^{-8}$	—	0.608	126.3	76.8

ARISPE (continued)

^{84}Kr	$^{36}Ar/^{84}Kr$	$^{78}Kr/^{84}Kr$	$*^{80}Kr/^{84}Kr$	$^{82}Kr/^{84}Kr$	$^{83}Kr/^{84}Kr$	$^{86}Kr/^{84}Kr$	$^{84}Kr/^{132}Xe$
$(1.186 \pm .021) \times 10^{-11}$	4657 ±96	0.0220 ±.0010	0.3522 ±.0097	0.356 ±.010	0.385 ±.013	0.3068 ±.0090	6.34 ±.13

^{132}Xe	$^{124}Xe/^{132}Xe$	$^{126}Xe/^{132}Xe$	$^{128}Xe/^{132}Xe$	$^{129}Xe/^{132}Xe$	$^{130}Xe/^{132}Xe$	$^{131}Xe/^{132}Xe$	$^{134}Xe/^{132}Xe$	$^{136}Xe/^{132}Xe$
$(1.87i \pm .021) \times 10^{-12}$	0.0216 ±.0008	0.0318 ±.0008	0.0968 ±.0040	1.047 ±.033	0.1449 ±.0047	0.822 ±.043	0.3627 ±.0097	0.3207 ±.0084

REFERENCES: A — This work; B — Hintenberger and Wänke, 1964; C — Schaeffer and Zähringer, 1959; D —Lipschutz et al., 1965.

TABLE 3 (continued)

METEORITE: Babb's Mill

SAMPLE NUMBER AND SOURCE: 78h; Mineralogical Museum, Harvard University; Carl A. Francis, Curator.

CLASSIFICATION: Structural — Nickel-rich Ataxite; Chemical — Anomalous.

COSMIC RAY EXPOSURE AGE: (10^6 years): 15-30, Voshage (1967).

FUSED SAMPLE MASS: 2.53990 ± 0.00029 grams

Concentrations in cm^3 STP/g

	^3He	$\frac{^4He}{^3He}$	^{20}Ne	$\frac{^4He}{^{20}Ne}$	$\frac{^{20}Ne}{^{22}Ne}$	$\frac{^{21}Ne}{^{22}Ne}$	^{36}Ar	$\frac{^{20}Ne}{^{36}Ar}$	$\frac{^{36}Ar}{^{38}Ar}$	$\frac{^{40}Ar}{^{36}Ar}$	$\frac{^{40}Ar}{^{38}Ar}$
A	$(1.544 \pm$ .016$)x10^{-7}$	4.550 ±.068	$(4.416 \pm$ .045$)x10^{-9}$	159.1 ±2.4	2.037 ±.046	0.747 ±.030	$(5.137 \pm$ .054$)x10^{-9}$	0.859 ±.012	0.941 ±.014	91.1 ±1.4	85.7 ±1.2
B	$1.3x10^{-7}$	3.76	[^{21}Ne] $1.75x10^{-9}$	[4/21] 280	—	0.926	$4.97x10^{-9}$	[21/36] 0.352	0.599	—	—

^{84}Kr	$\frac{^{36}Ar}{^{84}Kr}$	$\frac{^{78}Kr}{^{84}Kr}$	$\frac{^{80}Kr}{^{84}Kr}$	$\frac{^{82}Kr}{^{84}Kr}$	$\frac{^{83}Kr}{^{84}Kr}$	$\frac{^{86}Kr}{^{84}Kr}$	$\frac{^{84}Kr}{^{132}Xe}$
$(2.882 \pm$ .037$)x10^{-11}$	178.3 ± 3.0	0.00752 ±.00083	0.03847 ±.00095	0.2149 ±.0051	0.2140 ±.0051	0.3002 ±.0072	2.328 ±.038

BABB'S MILL (continued)

^{132}Xe	$\dfrac{^{124}Xe}{^{132}Xe}$	$\dfrac{^{126}Xe}{^{132}Xe}$	$\dfrac{^{128}Xe}{^{132}Xe}$	$\dfrac{^{129}Xe}{^{132}Xe}$	$\dfrac{^{130}Xe}{^{132}Xe}$	$\dfrac{^{131}Xe}{^{132}Xe}$	$\dfrac{^{134}Xe}{^{132}Xe}$	$\dfrac{^{136}Xe}{^{132}Xe}$
$(1.238 \pm .013) \times 10^{-11}$	0.00404 ±.00013	0.00626 ±.00023	0.0711 ±.0016	0.980 ±.022	0.1387 ±.0032	0.786 ±.018	0.3937 ±.0094	0.3421 ±.0080

REFERENCES: A — This work; B —Schultz and Hintenberger, (1967).

TABLE 3 (continued)

METEORITE: Bohumiltz

SAMPLE NUMBER AND SOURCE: Me 899; Field Museum of Natural History, Chicago, Illinois; Edward Olsen, Curator.

CLASSIFICATION: Structural — Coarse Octahedrite; Chemical — Group IA.

COSMIC RAY EXPOSURE AGE (10^6 years): 140 ± 230, Voshage (1978).

FUSED SAMPLE MASS: 3.74150 ± 0.00042 grams

Concentrations in $cm^3 STP/g$

	^3He	$\frac{^4He}{^3He}$	^{20}Ne	$\frac{^4He}{^{20}Ne}$	$\frac{^{20}Ne}{^{22}Ne}$	$\frac{^{21}Ne}{^{22}Ne}$	^{36}Ar	$\frac{^{20}Ne}{^{36}Ar}$	$\frac{^{36}Ar}{^{38}Ar}$	$\frac{^{40}Ar}{^{36}Ar}$	$\frac{^{40}Ar}{^{38}Ar}$
A	$(7.506 \pm .083) \times 10^{-7}$	$3.573 \pm .075$	$(1.098 \pm .013) \times 10^{-8}$	244.2 ± 5.2	$1.069 \pm .025$	$0.950 \pm .027$	$(3.186 \pm .049) \times 10^{-8}$	$0.3447 \pm .0066$	$0.681 \pm .012$	$7.24 \pm .17$	$4.925 \pm .099$
B	1.65×10^{-6}	3.47	2.16×10^{-8}	273	0.895	0.929	—	—	—	—	—
C	1.32×10^{-6}	3.95	1.87×10^{-8}	278	0.888	0.935	5.77×10^{-8}	0.324	0.645	2.40	1.55

BOHUMILTZ (continued)

^{84}Kr	$^{36}Ar/^{84}Kr$	$^{78}Kr/^{84}Kr$	$*^{80}Kr/^{84}Kr$	$^{82}Kr/^{84}Kr$	$^{83}Kr/^{84}Kr$	$^{86}Kr/^{84}Kr$	$^{84}Kr/^{132}Xe$
$(5.259 \pm .079)\times10^{-11}$	606 ±13	0.0697 ±.0034	0.2802 ±.0071	0.2240 ±.0069	0.2070 ±.0081	0.2971 ±.0075	4.765 ±.093

^{132}Xe	$^{124}Xe/^{132}Xe$	$^{126}Xe/^{132}Xe$	$^{128}Xe/^{132}Xe$	$^{129}Xe/^{132}Xe$	$^{130}Xe/^{132}Xe$	$^{131}Xe/^{132}Xe$	$^{134}Xe/^{132}Xe$	$^{136}Xe/^{132}Xe$
$(1.104 \pm .014)\times10^{-11}$	0.00772 ±.00025	0.00713 ±.00038	0.0821 ±.0021	1.056 ±.025	0.1686 ±.0043	0.817 ±.019	0.3801 ±.0098	0.3096 ±.0096

REFERENCES: A — This work; B — Hintenberger and Wänke (1964); C — Voshage and Feldman (1978).

TABLE 3 (continued)

METEORITE: Braunau

SAMPLE NUMBER AND SOURCE: Me 604; Field Museum of Natural History, Chicago, Illinois; Edward Olsen, Curator.

CLASSIFICATION: Structural — Hexahedrite; Chemical — Group II A.

COSMIC RAY EXPOSURE AGE (10^6 years): 4.5 ± 0.5, Vilcsek and Wänke (1962); 7.5, Cobb (1966).

FUSED SAMPLE MASS: 2.70640 ± 0.00031 grams

Concentrations in $cm^3 STP/g$

	^3He	$\frac{^4He}{^3He}$	^{20}Ne	$\frac{^4He}{^{20}Ne}$	$\frac{^{20}Ne}{^{22}Ne}$	$\frac{^{21}Ne}{^{22}Ne}$	^{36}Ar	$\frac{^{20}Ne}{^{36}Ar}$	$\frac{^{36}Ar}{^{38}Ar}$	$\frac{^{40}Ar}{^{36}Ar}$	$\frac{^{40}Ar}{^{38}Ar}$
A	$(3.974 \pm .041)x10^{-8}$	8.20 ±.12	$(2.068 \pm .026)x10^{-9}$	157.7 ± 2.6	1.657 ±.039	0.904 ±.026	$(3.316 \pm .039)x10^{-9}$	0.624 ±.011	0.799 ±.012	66.0 ±1.0	52.7 ±0.7
B	$3.92x10^{-8}$	13.18	—	—	—	—	—	—	—	—	—
C	$3.33x10^{-8}$	9.71	$3.27x10^{-9}$	100	2.02	0.827	—	—	—	—	—

BRAUNAU (continued)

^{84}Kr	^{36}Ar/^{84}Kr	^{78}Kr/^{84}Kr	^{80}Kr/^{84}Kr	^{82}Kr/^{84}Kr	^{83}Kr/^{84}Kr	^{86}Kr/^{84}Kr	^{84}Kr/^{132}Xe
$(1.302 \pm .014) \times 10^{-11}$	254.7 ± 4.1	0.0547 ±.0041	0.0428 ±.0012	0.2037 ±.0047	0.2086 ±.0048	0.2985 ±.0071	11.75 ±0.19

^{132}Xe	^{124}Xe/^{132}Xe	^{126}Xe/^{132}Xe	^{128}Xe/^{132}Xe	^{129}Xe/^{132}Xe	^{130}Xe/^{132}Xe	^{131}Xe/^{132}Xe	^{134}Xe/^{132}Xe	^{136}Xe/^{132}Xe
$(1.108 \pm .013) \times 10^{-12}$	0.0080 ±.0016	0.0093 ±.0024	0.0618 ±.0016	0.973 ±.023	0.1669 ±.0043	0.782 ±.019	0.3405 ±.0079	0.2906 ±.0074

REFERENCES: A — This work; B — Bauer (1963); C — Hintenberger and Wänke (1964).

TABLE 3 (continued)

METEORITE: Butler

SAMPLE NUMBER AND SOURCE: Me 1121; Field Museum of Natural History, Chicago, Illinois; Edward Olsen, Curator.

CLASSIFICATION: Structural — Plessitic Octahedrite; Chemical — Anomalous.

COSMIC RAY EXPOSURE AGE (10^6 years): 420-850, Voshage (1967).

FUSED SAMPLE MASS: 3.08160 ± 0.00035 grams

Concentrations in cm^3STP/g

	^3He	$\frac{^4He}{^3He}$	^{20}Ne	$\frac{^4He}{^{20}Ne}$	$\frac{^{20}Ne}{^{22}Ne}$	$\frac{^{21}Ne}{^{22}Ne}$	^{36}Ar	$\frac{^{20}Ne}{^{36}Ar}$	$\frac{^{36}Ar}{^{38}Ar}$	$\frac{^{40}Ar}{^{36}Ar}$	$\frac{^{40}Ar}{^{38}Ar}$
A	(2.090 ± .026)x10^{-6}	3.554 ±.077	(2.472 ± .026)x10^{-8}	300.5 ± 6.2	1.142 ±.027	0.965 ±.028	(7.874 ± .090)x10^{-9}	3.139 ±.048	0.714 ±.014	157.2 ± 2.4	112.3 ± 2.1
B	3.23x10^{-6}	3.94	[^{21}Ne] 3.55x10^{-8}	—	—	0.952	1.24x10^{-7}	—	0.638	—	—

	^{84}Kr	$\frac{^{36}Ar}{^{84}Kr}$	$\frac{^{78}Kr}{^{84}Kr}$	$\frac{^{80}Kr}{^{84}Kr}$	$\frac{^{82}Kr}{^{84}Kr}$	$\frac{^{83}Kr}{^{84}Kr}$	$\frac{^{86}Kr}{^{84}Kr}$	$\frac{^{84}Kr}{^{132}Xe}$
	(8.248 ± .085)x10^{-11}	95.5 ±1.5	0.0349 ±.0083	0.1250 ±.0029	0.2145 ±.0052	0.2108 ±.0048	0.3018 ±.0068	20.53 ±0.31

BUTLER (continued)

^{132}Xe	$\dfrac{^{124}Xe}{^{132}Xe}$	$\dfrac{^{126}Xe}{^{132}Xe}$	$\dfrac{^{128}Xe}{^{132}Xe}$	$\dfrac{^{129}Xe}{^{132}Xe}$	$\dfrac{^{130}Xe}{^{132}Xe}$	$\dfrac{^{131}Xe}{^{132}Xe}$	$\dfrac{^{134}Xe}{^{132}Xe}$	$\dfrac{^{136}Xe}{^{132}Xe}$
$(4.017 \pm .046) \times 10^{-12}$	0.00780 ±.00088	0.01020 ±.00043	0.0764 ±.0021	0.997 ±.024	0.1670 ±.0041	0.790 ±.020	0.3867 ±.0092	0.3191 ±.0076

REFERENCES: A — This work;   B — Schultz and Hintenberger (1967).

TABLE 3 (continued)

METEORITE: Cedartown

SAMPLE NUMBER AND SOURCE: Me 2373; Field Museum of Natural History, Chicago, Illinois; Edward Olsen, Curator.

CLASSIFICATION: Structural — Hexahedrite; Chemical — Group II A.

COSMIC RAY EXPOSURE AGE (10^6 years): 430, Bauer (1963); 180 ± 80, Voshage (1978).

FUSED SAMPLE MASS: 2.62510 ± .00030 grams

Concentrations in cm^3 STP/g

	^3He	$\frac{^4He}{^3He}$	^{20}Ne	$\frac{^4He}{^{20}Ne}$	$\frac{^{20}Ne}{^{22}Ne}$	$\frac{^{21}Ne}{^{22}Ne}$	^{36}Ar	$\frac{^{20}Ne}{^{36}Ar}$	$\frac{^{36}Ar}{^{38}Ar}$	$\frac{^{40}Ar}{^{36}Ar}$	$\frac{^{40}Ar}{^{38}Ar}$
A	$(4.997 \pm .050)\times10^{-7}$	4.372 ±.079	$(2.631 \pm .030)\times10^{-8}$	83.0 ±1.6	0.804 ±.018	0.764 ±.022	$(4.080 \pm 0.100)\times10^{-8}$	0.645 ±.018	0.613 ±.016	43.5 ±1.2	26.63 ± .38
B	2.52×10^{-6}	4.08	—	—	—	—	—	—	—	—	—
C	2.39×10^{-6}	4.02	3.14×10^{-8}	306	1.0	0.968	—	—	—	—	—
D	2.41×10^{-6}	3.98	3.16×10^{-8}	304	0.869	0.935	1.04×10^{-7}	0.304	0.640	1.40	0.90

CEDARTOWN (continued)

^{84}Kr	$^{36}Ar/^{84}Kr$	$^{78}Kr/^{84}Kr$	$^{80}Kr/^{84}Kr$	$^{82}Kr/^{84}Kr$	$^{83}Kr/^{84}Kr$	$^{86}Kr/^{84}Kr$	$^{84}Kr/^{132}Xe$
$(1.766 \pm .018)\times10^{-10}$	231.0 ± 6.2	0.00422 ±.00017	0.1584 ±.0039	0.2133 ±.0048	0.2111 ±.0048	0.3108 ±.0070	13.50 ±0.21

^{132}Xe	$^{124}Xe/^{132}Xe$	$^{126}Xe/^{132}Xe$	$^{128}Xe/^{132}Xe$	$^{129}Xe/^{132}Xe$	$^{130}Xe/^{132}Xe$	$^{131}Xe/^{132}Xe$	$^{134}Xe/^{132}Xe$	$^{136}Xe/^{132}Xe$
$(1.308 \pm .015)\times10^{-11}$	0.00856 ±.00047	0.01056 ±.00036	0.0784 ±.0019	0.984 ±.023	0.1568 ±.0039	0.795 ±.018	0.3879 ±.0094	0.3428 ±.0081

REFERENCES: A — This work; B — Bauer (1963); C — Hintenberger et al., (1967); D — Voshage and

Feldman (1978).

TABLE 3 (continued)

METEORITE: Dayton

SAMPLE NUMBER AND SOURCE: #653.1; Center for Meteorite Studies, Arizona State University;

Carlton B. Moore, Director.

CLASSIFICATION: Structural — Finest Octahedrite; Chemical — Group III D.

COSMIC RAY EXPOSURE AGE (10^6 years): 140 ± 10, Vilcsek and Wänke (1962); 218 ± 85, Voshage (1967).

FUSED SAMPLE MASS: 2.73290 ± 0.00031 grams

Concentrations in cm^3STP/g

	^3He	$\frac{^4He}{^3He}$	^{20}Ne	$\frac{^4He}{^{20}Ne}$	$\frac{^{20}Ne}{^{22}Ne}$	$\frac{^{21}Ne}{^{22}Ne}$	^{36}Ar	$\frac{^{20}Ne}{^{36}Ar}$	$\frac{^{36}Ar}{^{38}Ar}$	$\frac{^{40}Ar}{^{36}Ar}$	$\frac{^{40}Ar}{^{38}Ar}$
A	(1.434 ± .015)x10^{-6}	3.254 ±.057	(1.669 ± .017)x10^{-8}	279.6 ± 4.9	1.007 ±.025	0.980 ±.030	(2.803 ± .030)x10^{-8}	0.5954 ±.0088	0.682 ±.010	5.05 ±.10	3.443 ±.070
B	1.34x10^{-6}	3.64	1.60x10^{-8}	304	0.945	0.945	—	—	—	—	—

^{84}Kr	$\frac{^{36}Ar}{^{84}Kr}$	$\frac{^{78}Kr}{^{84}Kr}$	$\frac{^*{80}Kr}{^{84}Kr}$	$\frac{^{82}Kr}{^{84}Kr}$	$\frac{^{83}Kr}{^{84}Kr}$	$\frac{^{86}Kr}{^{84}Kr}$	$\frac{^{84}Kr}{^{132}Xe}$
(1.147 ± .014)x10^{-11}	2443 ± 40	0.0773 ±.0147	0.2790 ±.0067	0.2513 ±.0069	0.2391 ±.0059	0.3006 ±.0100	3.865 ±.081

DAYTON (continued)

^{132}Xe	$\dfrac{^{124}Xe}{^{132}Xe}$	$\dfrac{^{126}Xe}{^{132}Xe}$	$\dfrac{^{128}Xe}{^{132}Xe}$	$\dfrac{^{129}Xe}{^{132}Xe}$	$\dfrac{^{130}Xe}{^{132}Xe}$	$\dfrac{^{131}Xe}{^{132}Xe}$	$\dfrac{^{134}Xe}{^{132}Xe}$	$\dfrac{^{136}Xe}{^{132}Xe}$
$(2.969 \pm .050)\times10^{-12}$	0.00881 ±.00026	0.00599 ±.00021	0.0862 ±.0023	1.019 ±.032	0.1552 ±.0042	0.822 ±.023	0.415 ±.011	0.3435 ±.0097

REFERENCES: A — This work; B — Hintenberger and Wänke (1964).

TABLE 3 (continued)

METEORITE: Duchesne

SAMPLE NUMBER AND SOURCE: #40a; Center for Meteorite Studies, Arizona State University;

Carlton B. Moore, Director.

CLASSIFICATION: Structural — Fine Octahedrite; Chemical — Group IV A.

COSMIC RAY EXPOSURE AGE (10^6 years): 175 ± 120, 220 ± 70, Voshage (1967).

FUSED SAMPLE MASS: 0.02670 ± 0.00003 grams

Concentrations in cm^3STP/g

	^{3}He	$\frac{^4\text{He}}{^3\text{He}}$	^{20}Ne	$\frac{^4\text{He}}{^{20}\text{Ne}}$	$\frac{^{20}\text{Ne}}{^{22}\text{Ne}}$	$\frac{^{21}\text{Ne}}{^{22}\text{Ne}}$	^{36}Ar	$\frac{^{20}\text{Ne}}{^{36}\text{Ar}}$	$\frac{^{36}\text{Ar}}{^{38}\text{Ar}}$	$\frac{^{40}\text{Ar}}{^{36}\text{Ar}}$	$\frac{^{40}\text{Ar}}{^{38}\text{Ar}}$
A	(9.729 ± .098)x10^{-6}	3.87 ±.11	(1.553 ± .017)x10^{-7}	242.3 ± 6.8	1.118 ±.026	.941 ±.027	(3.540 ± .036)x10^{-7}	0.4385 ±.0065	0.6661 ±.0095	13.91 ±.39	9.26 ±.26
B	1.75x10^{-6}	3.60	[^{21}Ne] 2.32x10^{-8}	—	—	—	6.54x10^{-8}	—	0.640	73.7	47.2

^{84}Kr	$\frac{^{36}\text{Ar}}{^{84}\text{Kr}}$	$\frac{^{78}\text{Kr}}{^{84}\text{Kr}}$	$\frac{^{80}\text{Kr}}{^{84}\text{Kr}}$	$\frac{^{82}\text{Kr}}{^{84}\text{Kr}}$	$\frac{^{83}\text{Kr}}{^{84}\text{Kr}}$	$\frac{^{86}\text{Kr}}{^{84}\text{Kr}}$	$\frac{^{84}\text{Kr}}{^{132}\text{Xe}}$
(5.996 ± .060)x10^{-10}	590.4 ± 8.4	0.0507 ±.0086	0.0477 ±.0014	0.2183 ±.0065	0.2256 ±.0055	0.2954 ±.0074	28.40 ±0.42

DUCHESNE (continued)

^{132}Xe	$\dfrac{^{124}Xe}{^{132}Xe}$	$\dfrac{^{126}Xe}{^{132}Xe}$	$\dfrac{^{128}Xe}{^{132}Xe}$	$\dfrac{^{129}Xe}{^{132}Xe}$	$\dfrac{^{130}Xe}{^{132}Xe}$	$\dfrac{^{131}Xe}{^{132}Xe}$	$\dfrac{^{134}Xe}{^{132}Xe}$	$\dfrac{^{136}Xe}{^{132}Xe}$
$(2.111 \pm$ .023$) \times 10^{-11}$	0.0853 $\pm$.0189	0.0765 $\pm$.0151	0.1237 $\pm$.0069	1.010 $\pm$.042	0.144 $\pm$.022	0.821 $\pm$.040	0.398 $\pm$.032	0.325 $\pm$.020

REFERENCES: A— This work; B — Lipschutz et al. (1965).

TABLE 3 (continued)

METEORITE: Edmonton (Kentucky)

SAMPLE NUMBER AND SOURCE: USNM 1413; National Museum of Natural History, Smithsonian Institution;

Roy S. Clark, Jr., Curator, Division of Meteorites.

CLASSIFICATION: Structural – Fine Octahedrite; Chemical – Group III C.

COSMIC RAY EXPOSURE AGE (10^6 years): None reported.

FUSED SAMPLE MASS: 2.25480 ± 0.00025 grams

Concentrations in cm^3STP/g

	^3He	$\frac{^4He}{^3He}$	^{20}Ne	$\frac{^4He}{^{20}Ne}$	$\frac{^{20}Ne}{^{22}Ne}$	$\frac{^{21}Ne}{^{22}Ne}$	^{36}Ar	$\frac{^{20}Ne}{^{36}Ar}$	$\frac{^{36}Ar}{^{38}Ar}$	$\frac{^{40}Ar}{^{36}Ar}$	$\frac{^{40}Ar}{^{38}Ar}$
A	(1.569 ± .028)x10⁻⁶	3.120 ±.086	(5.769 ± .060)x10⁻⁸	84.9 ±2.0	0.896 ±.020	0.978 ±.028	(1.167 ± .012)x10⁻⁷	0.4941 ±.0071	0.6881 ±.0098	3.502 ±.050	2.410 ±.034

^{84}Kr	$^{36}Ar/^{84}Kr$	$^{78}Kr/^{84}Kr$	$^{80}Kr/^{84}Kr$	$^{82}Kr/^{84}Kr$	$^{83}Kr/^{84}Kr$	$^{86}Kr/^{84}Kr$	$^{84}Kr/^{132}Xe$
(2.031 ± .020)x10⁻¹¹	5748 ± 82	0.0573 ±.0035	0.2291 ±.0055	0.2504 ±.0061	0.2535 ±.0059	0.2835 ±.0071	7.13 ±.10

EDMONTON (continued)

^{132}Xe	$\frac{^{124}\text{Xe}}{^{132}\text{Xe}}$	$\frac{^{126}\text{Xe}}{^{132}\text{Xe}}$	$\frac{^{128}\text{Xe}}{^{132}\text{Xe}}$	$\frac{^{129}\text{Xe}}{^{132}\text{Xe}}$	$\frac{^{130}\text{Xe}}{^{132}\text{Xe}}$	$\frac{^{131}\text{Xe}}{^{132}\text{Xe}}$	$\frac{^{134}\text{Xe}}{^{132}\text{Xe}}$	$\frac{^{136}\text{Xe}}{^{132}\text{Xe}}$
$(2.849 \pm .030) \times 10^{-12}$	0.0121 $\pm.0012$	0.0171 $\pm.0011$	0.0925 $\pm.0021$	1.086 $\pm.029$	0.1755 $\pm.0051$	0.814 $\pm.022$	0.3916 $\pm.0089$	0.330 $\pm.011$

REFERENCE: A — This work.

TABLE 3 (continued)

METEORITE: El Burro

SAMPLE NUMBER AND SOURCE: #469.1x; Center for Meteorite Studies, Arizona State University;

Carlton B. Moore, Director.

CLASSIFICATION: Structural—Coarsest Octahedrite; Chemical — Group II B.

COSMIC RAY EXPOSURE AGE (10^6 years): 165 ± 115, Voshage (1978).

FUSED SAMPLE MASS: 2.45790 ± 0.00028 grams

Concentrations in cm^3STP/g

	^{3}He	$\frac{^4\text{He}}{^3\text{He}}$	^{20}Ne	$\frac{^4\text{He}}{^{20}\text{Ne}}$	$\frac{^{20}\text{Ne}}{^{22}\text{Ne}}$	$\frac{^{21}\text{Ne}}{^{22}\text{Ne}}$	^{36}Ar	$\frac{^{20}\text{Ne}}{^{36}\text{Ar}}$	$\frac{^{36}\text{Ar}}{^{38}\text{Ar}}$	$\frac{^{40}\text{Ar}}{^{36}\text{Ar}}$	$\frac{^{40}\text{Ar}}{^{38}\text{Ar}}$
A	(4.558 ± .048)x10^{-7}	3.446 ±.067	(4.286 ± .102)x10^{-9}	366.4 ±10.6	0.932 ±.029	0.984 ±.030	(1.527 ± .017)x10^{-8}	0.2807 ±.0074	0.6455 ±.0097	5.31 ±.10	3.429 ±.066
B	4.5x10^{-7}	4.02	4.79x10^{-9}	379	0.870	0.926	1.63x10^{-8}	0.294	0.609	4.98	3.03

^{84}Kr	$\frac{^{36}\text{Ar}}{^{84}\text{Kr}}$	$\frac{^{78}\text{Kr}}{^{84}\text{Kr}}$	$\frac{^{80}\text{Kr}}{^{84}\text{Kr}}$	$\frac{^{82}\text{Kr}}{^{84}\text{Kr}}$	$\frac{^{83}\text{Kr}}{^{84}\text{Kr}}$	$\frac{^{86}\text{Kr}}{^{84}\text{Kr}}$	$\frac{^{84}\text{Kr}}{^{132}\text{Xe}}$
(5.991 ± .077)x10^{-12}	2548 ± 43	0.069 ±.018	0.1104 ±.0039	0.2539 ±.0064	0.2500 ±.0066	0.2995 ±.0073	17.48 ±0.36

EL BURRO (continued)

^{132}Xe	$\dfrac{^{124}Xe}{^{132}Xe}$	$\dfrac{^{126}Xe}{^{132}Xe}$	$\dfrac{^{128}Xe}{^{132}Xe}$	$\dfrac{^{129}Xe}{^{132}Xe}$	$\dfrac{^{130}Xe}{^{132}Xe}$	$\dfrac{^{131}Xe}{^{132}Xe}$	$\dfrac{^{134}Xe}{^{132}Xe}$	$\dfrac{^{136}Xe}{^{132}Xe}$
$(3.427 \pm .055) \times 10^{-13}$	0.0498 $\pm .0060$	0.0329 $\pm .0051$	0.0915 $\pm .0091$	1.272 $\pm .057$	0.153 $\pm .016$	0.933 $\pm .025$	0.398 $\pm .013$	0.323 $\pm .026$

REFERENCES: A — This work; B — Voshage and Feldman (1978).

TABLE 3 (continued)

METEORITE: Hoba

SAMPLE SOURCE: Edward L. Fireman, Astrophysical Observatory, Smithsonian Institution.

CLASSIFICATION: Structural — Nickel-rich Ataxite; Chemical — Group IV B.

COSMIC RAY EXPOSURE AGE (10^6 years): 190, Bauer (1963); 300 ± 110, Voshage (1967); 263 ± 40, McCorkell et al. (1968).

FUSED SAMPLE MASS: 3.25960 ± 0.00037 grams

Concentrations in cm^3STP/g

	^{3}He	$\frac{^4\text{He}}{^3\text{He}}$	^{20}Ne	$\frac{^4\text{He}}{^{20}\text{Ne}}$	$\frac{^{20}\text{Ne}}{^{22}\text{Ne}}$	$\frac{^{21}\text{Ne}}{^{22}\text{Ne}}$	^{36}Ar	$\frac{^{20}\text{Ne}}{^{36}\text{Ar}}$	$\frac{^{36}\text{Ar}}{^{38}\text{Ar}}$	$\frac{^{40}\text{Ar}}{^{36}\text{Ar}}$	$\frac{^{40}\text{Ar}}{^{38}\text{Ar}}$
A	$(3.335 \pm .035)\text{x}10^{-7}$	3.792 ±.081	$(2.509 \pm .063)\text{x}10^{-9}$	504 ±16	0.901 ±.029	0.902 ±.027	$(1.035 \pm .011)\text{x}10^{-8}$	0.2424 ±.0066	0.677 ±.010	19.35 ±.28	13.10 ± .20
B	$3.48\text{x}10^{-7}$	4.50	—	—	—	—	—	—	—	—	—
C	$4.4\text{x}10^{-7}$	4.37	$[^{21}\text{Ne}]$ $4.8\text{x}10^{-9}$	—	—	0.943	$1.88\text{x}10^{-8}$	—	0.608	—	—

HOBA (continued)

^{84}Kr	^{36}Ar/^{84}Kr	^{78}Kr/^{84}Kr	^{80}Kr/^{84}Kr	^{82}Kr/^{84}Kr	^{83}Kr/^{84}Kr	^{86}Kr/^{84}Kr	^{84}Kr/^{132}Xe
$(1.933 \pm .023) \times 10^{-11}$	535.3 ± 8.5	0.0278 ± .0019	0.1391 ± .0038	0.2518 ± .0066	0.2606 ± .0061	0.2916 ± .0088	9.63 ± .24

^{132}Xe	^{124}Xe/^{132}Xe	^{126}Xe/^{132}Xe	^{128}Xe/^{132}Xe	^{129}Xe/^{132}Xe	^{130}Xe/^{132}Xe	^{131}Xe/^{132}Xe	^{134}Xe/^{132}Xe	^{136}Xe/^{132}Xe
$(2.007 \pm .044) \times 10^{-12}$	0.0110 ± .0031	0.01154 ± .00042	0.0792 ± .0068	1.035 ± .037	0.1541 ± .0052	0.806 ± .026	0.356 ± .030	0.3081 ± .0093

REFERENCES: A — This work;   B — Bauer (1963);   C — Schultz and Hintenberger (1967).

TABLE 3 (continued)

METEORITE: Odessa

SAMPLE SOURCE: Dieter Heymann, Rice University, Houston, Texas.

CLASSIFICATION: Structural — Coarse Octahedrite; Chemical — Group I A.

COSMIC RAY EXPOSURE AGE (10^6 years): 325 ± 25, Fisher and Schaeffer (1960); 450 ± 300, Signer and Nier (1962); 460 ± 50, Vilcsek and Wänke (1962); 890 ± 70, Voshage (1967).

FUSED SAMPLE MASS: 2.25200 ± 0.00026 grams

Concentrations in cm^3 STP/g

	^3He	$\frac{^4He}{^3He}$	^{20}Ne	$\frac{^4He}{^{20}Ne}$	$\frac{^{20}Ne}{^{22}Ne}$	$\frac{^{21}Ne}{^{22}Ne}$	^{36}Ar	$\frac{^{20}Ne}{^{36}Ar}$	$\frac{^{36}Ar}{^{38}Ar}$	$\frac{^{40}Ar}{^{36}Ar}$	$\frac{^{40}Ar}{^{38}Ar}$
A	$(4.871 \pm .050) \times 10^{-7}$	$3.606 \pm .062$	$(1.022 \pm .010) \times 10^{-8}$	171.9 ± 2.9	$1.164 \pm .026$	$0.932 \pm .026$	$(6.810 \pm .081) \times 10^{-9}$	$1.501 \pm .023$	$0.716 \pm .012$	$29.24 \pm .46$	$20.94 \pm .32$
B	2.20×10^{-6}	3.22	2.55×10^{-8}	278	1.0	0.9	7.0×10^{-8}	0.364	0.583	1.44	0.842
C	1.03×10^{-6}	4.02	1.82×10^{-8}	228	1.44	0.917	4.32×10^{-8}	0.421	0.640	46.9	30.0
D	3.47×10^{-7}	3.47	5.81×10^{-9}	208	1.21	0.940	—	—	—	—	—
E	7.1×10^{-7}	4.31	5.87×10^{-9}	377	0.843	0.989	—	—	—	—	—

ODESSA (continued)

^{84}Kr	$^{36}Ar/^{84}Kr$	$^{78}Kr/^{84}Kr$	$^{80}Kr/^{84}Kr$	$^{82}Kr/^{84}Kr$	$^{83}Kr/^{84}Kr$	$^{86}Kr/^{84}Kr$	$^{84}Kr/^{132}Xe$
$(1.084 \pm .011) \times 10^{-11}$	628.1 $\pm$ 9.9	0.0273 $\pm$.0018	0.0730 $\pm$.0018	0.2122 $\pm$.0048	0.2144 $\pm$.0056	0.2928 $\pm$.0067	1.675 $\pm$.027

^{132}Xe	$\dfrac{^{124}Xe}{^{132}Xe}$	$\dfrac{^{126}Xe}{^{132}Xe}$	$\dfrac{^{128}Xe}{^{132}Xe}$	$\dfrac{^{129}Xe}{^{132}Xe}$	$\dfrac{^{130}Xe}{^{132}Xe}$	$\dfrac{^{131}Xe}{^{132}Xe}$	$\dfrac{^{134}Xe}{^{132}Xe}$	$\dfrac{^{136}Xe}{^{132}Xe}$
$(6.475 \pm .080) \times 10^{-12}$	0.00454 $\pm$.00024	0.00578 $\pm$.00015	0.0655 $\pm$.0018	0.979 $\pm$.024	0.1534 $\pm$.0037	0.795 $\pm$.019	0.395 $\pm$.010	0.3453 $\pm$.0081

REFERENCES: A — This work; B — Schaeffer and Zähringer (1959); C — Signer and Nier (1962);

D — Hintenberger and Wänke (1964); E — Hintenberger et al. (1967).

TABLE 3 (continued)

SAMPLE: Graphite and Troilite Separates from the Odessa Meteorite.

FUSED SAMPLE MASS: Graphite — 0.094140 ± 0.000010 grams

Troilite — 0.091670 ± 0.000010 grams

Graphite from Sawings — 0.080630 ± 0.000007 grams

Non-magnetic Troilite — 0.164510 ± 0.000012 grams

Concentrations in cm^3STP/g

	^3He	$\frac{^4He}{^3He}$	^{20}Ne	$\frac{^4He}{^{20}Ne}$	$\frac{^{20}Ne}{^{22}Ne}$	$\frac{^{21}Ne}{^{22}Ne}$	^{36}Ar	$\frac{^{20}Ne}{^{36}Ar}$	$\frac{^{36}Ar}{^{38}Ar}$	$\frac{^{40}Ar}{^{36}Ar}$	$\frac{^{40}Ar}{^{38}Ar}$
A	$(4.201 \pm .043)x10^{-7}$	8.07 ±.12	$(5.735 \pm .060)x10^{-8}$	59.10 ± .91	2.967 ±.068	0.800 ±.023	$(1.029 \pm .010)x10^{-7}$	0.557 ±.081	3.989 ±.059	232.9 ± 3.3	929 ±14
B	$(1.816 \pm .018)x10^{-6}$	5.806 ±.091	$(1.212 \pm .012)x10^{-7}$	87.0 ±1.4	0.947 ±.021	0.851 ±.024	$(9.079 \pm .091)x10^{-8}$	1.335 ±.019	1.380 ±.020	155.2 ± 2.2	214.3 ± 3.2
C	$(1.209 \pm .012)x10^{-7}$	41.66 ±.74	$(3.171 \pm .035)x10^{-8}$	158.8 ±2.9	1.486 ±.044	1.144 ±.039	$(1.302 \pm .013)x10^{-7}$	0.2435 ±.0036	1.345 ±.020	228.6 ± 3.4	307.6 ± 4.7
D	$(1.641 \pm .017)x10^{-6}$	6.05 ±.11	$(1.662 \pm .018)x10^{-7}$	59.7 ±1.1	1.339 ±.030	0.816 ±.023	$(9.149 \pm .097)x10^{-8}$	1.817 ±.027	0.777 ±.012	150.1 ± 2.2	116.6 ± 1.7

GRAPHITE AND TROILITE SEPARATES FROM THE ODESSA METEORITE (continued)

	^{84}Kr	$^{36}Ar/^{84}Kr$	$^{78}Kr/^{84}Kr$	$^{80}Kr/^{84}Kr$	$^{82}Kr/^{84}Kr$	$^{83}Kr/^{84}Kr$	$^{86}Kr/^{84}Kr$	$^{84}Kr/^{132}Xe$
A	$(2.613 \pm .026)\text{x}10^{-9}$	39.39 ± .56	0.0166 ±.0020	0.0679 ±.0016	0.2052 ±.0046	0.1957 ±.0044	0.2983 ±.0067	5.873 ±.090
B	$(1.051 \pm .011)\text{x}10^{-9}$	86.4 ±1.2	1.188 ±.027	0.1059 ±.0036	0.2183 ±.0052	0.2313 ±.0052	0.2992 ±.0069	8.96 ±.13
C	$(3.569 \pm .036)\text{x}10^{-9}$	36.49 ± .52	0.4043 ±.0092	0.630 ±.014	0.1906 ±.0043	0.2112 ±.0048	0.3394 ±.0076	6.37 ±.14
D	$(1.337 \pm .014)\text{x}10^{-9}$	68.4 ±1.0	———	0.459 ±.015	0.2203 ±.0050	0.2116 ±.0048	0.3162 ±.0073	7.33 ±.11

GRAPHITE AND TROILITE SEPARATES FROM THE ODESSA METEORITE (continued)

	^{132}Xe	$\dfrac{^{124}Xe}{^{132}Xe}$	$\dfrac{^{126}Xe}{^{132}Xe}$	$\dfrac{^{128}Xe}{^{132}Xe}$	$\dfrac{^{129}Xe}{^{132}Xe}$	$\dfrac{^{130}Xe}{^{132}Xe}$	$\dfrac{^{131}Xe}{^{132}Xe}$	$\dfrac{^{134}Xe}{^{132}Xe}$	$\dfrac{^{136}Xe}{^{132}Xe}$
A	$(4.449 \pm .052) \times 10^{-10}$	0.00976 ±.00029	0.00893 ±.00051	0.0705 ±.0024	1.010 ±.023	0.1383 ±.0033	0.831 ±.022	0.3946 ±.0094	0.3199 ±.0082
B	$(1.174 \pm .012) \times 10^{-10}$	0.0174 ±.0034	0.01551 ±.00058	0.0894 ±.0027	1.114 ±.033	0.1512 ±.0067	0.816 ±.018	0.414 ±.011	0.3300 ±.0096
C	$(5.61 \pm .11) \times 10^{-10}$	0.01655 ±.00047	0.01852 ±.00090	0.1288 ±.0057	1.103 ±.032	0.1731 ±.0050	0.813 ±.023	0.409 ±.013	0.3182 ±.0089
D	$(1.823 \pm .020) \times 10^{-10}$	0.01254 ±.00050	0.01212 ±.00064	0.1253 ±.0031	1.188 ±.027	0.1768 ±.0041	0.866 ±.020	0.3674 ±.0093	0.2952 ±.0070

LEGEND: A — Graphite; B — Troilite; C — Graphite from Sawings; D — Non-magnetic Troilite.

TABLE 3 (continued)

METEORITE: Sierra Gorda

SAMPLE NUMBER AND SOURCE: USNM 1307; National Museum of Natural History, Smithsonian Institution;

Roy S. Clark, Jr., Curator, Division of Meteorites.

CLASSIFICATION: Structural — Hexahedrite; Chemical — Group II A.

COSMIC RAY EXPOSURE AGE (10^6 years): 110, Bauer (1963); 140 ± 110, Voshage (1978).

FUSED SAMPLE MASS: 2.55060 ± 0.00029 grams

Concentrations in cm^{3}STP/g

	^{3}He	$\frac{^4\text{He}}{^3\text{He}}$	^{20}Ne	$\frac{^4\text{He}}{^{20}\text{Ne}}$	$\frac{^{20}\text{Ne}}{^{22}\text{Ne}}$	$\frac{^{21}\text{Ne}}{^{22}\text{Ne}}$	^{36}Ar	$\frac{^{20}\text{Ne}}{^{36}\text{Ar}}$	$\frac{^{36}\text{Ar}}{^{38}\text{Ar}}$	$\frac{^{40}\text{Ar}}{^{36}\text{Ar}}$	$\frac{^{40}\text{Ar}}{^{38}\text{Ar}}$
A	$(4.663 \pm .048) \times 10^{-7}$	4.278 ±.063	$(5.716 \pm .059) \times 10^{-9}$	349.0 ± 5.1	0.961 ±.022	0.980 ±.028	$(4.767 \pm .048) \times 10^{-9}$	1.199 ±.017	0.6442 ±.0093	10.31 ±.20	6.64 ±.13
B	3.68×10^{-7}	4.42	—	—	—	—	—	—	—	—	—
C	3.1×10^{-7}	4.44	4.46×10^{-9}	307	0.888	0.935	1.42×10^{-8}	0.314	0.624	5.78	3.61

SIERRA GORDA (continued)

^{84}Kr	$^{36}Ar/^{84}Kr$	$^{78}Kr/^{84}Kr$	$^{80}Kr/^{84}Kr$	$^{82}Kr/^{84}Kr$	$^{83}Kr/^{84}Kr$	$^{86}Kr/^{84}Kr$	$^{84}Kr/^{132}Xe$
$(7.679 \pm .079) \times 10^{-11}$	62.08 ±0.89	0.04010 ±.00097	0.1156 ±.0027	0.2727 ±.0061	0.2695 ±.0061	0.2963 ±.0067	4.574 ±.066

^{132}Xe	$^{124}Xe/^{132}Xe$	$^{126}Xe/^{132}Xe$	$^{128}Xe/^{132}Xe$	$^{129}Xe/^{132}Xe$	$^{130}Xe/^{132}Xe$	$^{131}Xe/^{132}Xe$	$^{134}Xe/^{132}Xe$	$^{136}Xe/^{132}Xe$
$(1.679 \pm .017) \times 10^{-11}$	0.01444 ±.00036	0.01420 ±.00037	0.0963 ±.0022	1.048 ±.023	0.1776 ±.0040	0.797 ±.018	0.3457 ±.0078	0.2919 ±.0065

REFERENCES: A — This work; B — Bauer (1963); C — Voshage and Feldman (1978).

TABLE 3 (continued)

METEORITE: Tawallah Valley

SAMPLE NUMBER AND SOURCE: USNM 1458; National Museum of Natural History, Smithsonian Institution;

Roy S. Clark, Jr., Curator, Division of Meteorites.

CLASSIFICATION: Structural — Nickel-rich Ataxite; Chemical — Group IV B.

COSMIC RAY EXPOSURE AGE (10^6 years): 245 ± 85, Voshage (1967).

FUSED SAMPLE MASS: 2.99110 ± 0.00034 grams

Concentrations in cm^3STP/g

	^{3}He	$\dfrac{^4\text{He}}{^3\text{He}}$	^{20}Ne	$\dfrac{^4\text{He}}{^{20}\text{Ne}}$	$\dfrac{^{20}\text{Ne}}{^{22}\text{Ne}}$	$\dfrac{^{21}\text{Ne}}{^{22}\text{Ne}}$	^{36}Ar	$\dfrac{^{20}\text{Ne}}{^{36}\text{Ar}}$	$\dfrac{^{36}\text{Ar}}{^{38}\text{Ar}}$	$\dfrac{^{40}\text{Ar}}{^{36}\text{Ar}}$	$\dfrac{^{40}\text{Ar}}{^{38}\text{Ar}}$
A	$(1.990 \pm .020)\text{x}10^{-6}$	$3.128 \pm .078$	$(2.757 \pm .028)\text{x}10^{-8}$	225.7 ± 5.6	$1.097 \pm .025$	$0.968 \pm .028$	$(2.696 \pm .027)\text{x}10^{-8}$	$1.023 \pm .015$	$0.710 \pm .011$	$12.56 \pm .18$	$8.92 \pm .14$

^{84}Kr	$\dfrac{^{36}\text{Ar}}{^{84}\text{Kr}}$	$\dfrac{^{78}\text{Kr}}{^{84}\text{Kr}}$	$\dfrac{^{80}\text{Kr}}{^{84}\text{Kr}}$	$\dfrac{^{82}\text{Kr}}{^{84}\text{Kr}}$	$\dfrac{^{83}\text{Kr}}{^{84}\text{Kr}}$	$\dfrac{^{86}\text{Kr}}{^{84}\text{Kr}}$	$\dfrac{^{84}\text{Kr}}{^{132}\text{Xe}}$
$(1.639 \pm .021)\text{x}10^{-11}$	1645 ± 27	$0.0602 \pm .0041$	$0.196 \pm .012$	$0.3208 \pm .0078$	$0.3286 \pm .0080$	$0.2989 \pm .0077$	14.28 ± 0.23

TAWALLAH VALLEY (continued)

^{132}Xe	$\frac{^{124}\text{Xe}}{^{132}\text{Xe}}$	$\frac{^{126}\text{Xe}}{^{132}\text{Xe}}$	$\frac{^{128}\text{Xe}}{^{132}\text{Xe}}$	$\frac{^{129}\text{Xe}}{^{132}\text{Xe}}$	$\frac{^{130}\text{Xe}}{^{132}\text{Xe}}$	$\frac{^{131}\text{Xe}}{^{132}\text{Xe}}$	$\frac{^{134}\text{Xe}}{^{132}\text{Xe}}$	$\frac{^{136}\text{Xe}}{^{132}\text{Xe}}$
$(1.148 \pm .012)\text{x}10^{-12}$	0.00530 ±.00074	0.0081 ±.0013	0.0714 ±.0036	0.842 ±.019	0.1555 ±.0035	0.811 ±.029	0.3780 ±.0087	0.3294 ±.0084

REFERENCE: A — This work.

TABLE 3 (continued)

METEORITE: Tombigbee River

SAMPLE NUMBER AND SOURCE: Me 504; Field Museum of Natural History, Chicago, Illinois; Edward Olsen, Curator.

CLASSIFICATION: Structural — Hexahedrite; Chemical — Anomalous,

COSMIC RAY EXPOSURE AGE (10^6 years): 535 ± 50, Kaiser and Zähringer (1968).

FUSED SAMPLE MASS: 2.71770 ± 0.00031 grams

Concentrations in cm^3STP/g

	^3He	$\frac{^4He}{^3He}$	^{20}Ne	$\frac{^4He}{^{20}Ne}$	$\frac{^{20}Ne}{^{22}Ne}$	$\frac{^{21}Ne}{^{22}Ne}$	^{36}Ar	$\frac{^{20}Ne}{^{36}Ar}$	$\frac{^{36}Ar}{^{38}Ar}$	$\frac{^{40}Ar}{^{36}Ar}$	$\frac{^{40}Ar}{^{38}Ar}$
A	$(9.881 \pm .099)\times10^{-8}$	$3.082 \pm .088$	$(4.932 \pm .062)\times10^{-9}$	61.7 ± 1.8	$0.890 \pm .021$	$0.978 \pm .028$	$(5.279 \pm .068)\times10^{-9}$	$0.934 \pm .017$	$0.697 \pm .012$	$54.61 \pm .93$	$38.06 \pm .61$
B	4.7×10^{-8}	7.11	$[^{21}Ne]$ 7.7×10^{-10}	—	—	0.55	2.8×10^{-9}	—	0.76	—	—
C	6.93×10^{-8}	7.04	—	—	—	—	—	—	—	—	—

TOMBIGBEE RIVER (continued)

^{84}Kr	$^{36}Ar/^{84}Kr$	$^{78}Kr/^{84}Kr$	$^{80}Kr/^{84}Kr$	$^{82}Kr/^{84}Kr$	$^{83}Kr/^{84}Kr$	$^{86}Kr/^{84}Kr$	$^{84}Kr/^{132}Xe$
$(1.415 \pm .016)\times10^{-11}$	373.0 ± 6.4	0.0560 ±.0022	0.0548 ±.0016	0.2093 ±.0050	0.2036 ±.0048	0.2941 ±.0070	18.51 ±0.30

^{132}Xe	$^{124}Xe/^{132}Xe$	$^{126}Xe/^{132}Xe$	$^{128}Xe/^{132}Xe$	$^{129}Xe/^{132}Xe$	$^{130}Xe/^{132}Xe$	$^{131}Xe/^{132}Xe$	$^{134}Xe/^{132}Xe$	$^{136}Xe/^{132}Xe$
$(7.647 \pm .092)\times10^{-13}$	0.0177 ±.0050	0.0278 ±.0046	0.1336 ±.0034	0.918 ±.023	0.1426 ±.0092	0.735 ±.024	0.377 ±.022	0.308 ±.025

REFERENCES: A — This work; B — Fisher and Schaeffer (1959); C — Bauer (1963).

TABLE 4

HELIUM, NEON, AND ARGON ISOTOPIC RATIOS

Meteorite	$^4He/^3He$	$^4He/^{20}Ne$	$^{20}Ne/^{22}Ne$	$^{21}Ne/^{22}Ne$	$^{20}Ne/^{36}Ar$	$^{36}Ar/^{38}Ar$	$^{40}Ar/^{36}Ar$	$^{40}Ar/^{38}Ar$
Arispe	3.355	241.4	1.085	0.982	0.3224	0.6600	2.446	1.613
Babb's Mill	4.550	159.1	2.037	0.747	0.859	0.941	91.1	85.7
Bohumiltz	3.573	244.2	1.069	0.950	0.3447	0.681	7.24	4.925
Braunau	8.20	157.7	1.657	0.904	0.624	0.799	66.0	52.7
Butler	3.554	300.5	1.142	0.965	3.139	0.714	157.2	112.3
Cedartown	4.372	83.0	0.804	0.764	0.645	0.613	43.5	26.63
Dayton	3.254	279.6	1.007	0.980	0.5954	0.682	5.05	3.443
Duchesne	3.87	242.3	1.118	0.941	0.4385	0.6661	13.91	9.26
Edmonton	3.120	84.9	0.896	0.978	0.4941	0.6881	3.502	2.410
El Burro	3.446	366.4	0.932	0.984	0.2807	0.6455	5.31	3.429
Hoba	3.792	504	0.901	0.902	0.2424	0.677	19.35	13.10
Odessa	3.606	171.9	1.164	0.932	1.501	0.716	29.24	20.94
Sierra Gorda	4.278	349.0	0.961	0.980	1.199	0.6442	10.31	6.64
Tawallah Valley	3.128	225.7	1.097	0.968	1.023	0.710	12.56	8.92

TABLE 4 (continued)

Meteorite	$^4He/^3He$	$^4He/^{20}Ne$	$^{20}Ne/^{22}Ne$	$^{21}Ne/^{22}Ne$	$^{20}Ne/^{36}Ar$	$^{36}Ar/^{38}Ar$	$^{40}Ar/^{36}Ar$	$^{40}Ar/^{38}Ar$
Tombigbee River	3.082	61.7	0.890	0.978	0.934	0.697	54.61	38.06
Costilla Peak	—	—	0.909	0.89	0.332	0.641	4.06	2.60
Carbo	—	—	0.846	0.89	0.48	0.599	4.6	2.77
Misteca	—	—	0.942	0.89	0.60	0.582	24.6	15.6
Xiquipilco	—	—	—	—	—	1.42	189	269
Cape York	—	—	—	—	—	1.57	206	219
Spallation	3.80 ± .03	—	0.935 ± .043	0.958 ± .031	—	0.641 ± .026	—	—
Atmosphere	7690	—	9.80	0.029	—	5.35	295.5	1581
Solar Wind	2700	—	12.85	0.0321	—	5.32	—	—

TABLE 5

KRYPTON ISOTOPIC RATIOS

Meteorite	$^{36}Ar/^{84}Kr$	$^{78}Kr/^{84}Kr$	$^{80}Kr/^{84}Kr$	$^{82}Kr/^{84}Kr$	$^{83}Kr/^{84}Kr$	$^{86}Kr/^{84}Kr$	$^{84}Kr/^{132}Xe$
Arispe	4657	0.0220	*0.3522	0.356	0.385	0.3068	6.34
Babb's Mill	178.3	0.00752	0.0385	0.2149	0.2140	0.3002	2.328
Bohumiltz	606	0.0697	*0.2802	0.2240	0.2070	0.2971	4.765
Braunau	254.7	0.0547	0.0428	0.2037	0.2086	0.2985	11.75
Butler	95.5	0.0349	0.1250	0.2145	0.2108	0.3018	20.53
Cedartown	231.0	0.00422	0.1584	0.2133	0.2111	0.3108	13.50
Dayton	2443	0.0773	*0.2790	0.2513	0.2391	0.3006	3.865
Duchesne	590.4	0.0507	0.0477	0.2183	0.2256	0.2954	28.40
Edmonton	5748	0.0573	0.2291	0.2504	0.2535	0.2835	7.13
El Burro	2548	0.069	0.1104	0.2539	0.2500	0.2995	17.48
Hoba	535.3	0.0278	0.1391	0.2518	0.2606	0.2916	9.63
Odessa	628.1	0.0273	0.0730	0.2122	0.2144	0.2928	1.675
Sierra Gorda	62.08	0.04010	0.1156	0.2727	0.2695	0.2963	4.574
Tawallah Valley	1645	0.0602	0.196	0.3208	0.3286	0.2989	14.28

TABLE 5 (continued)

Meteorite	^{36}Ar/^{84}Kr	^{78}Kr/^{84}Kr	^{80}Kr/^{84}Kr	^{82}Kr/^{84}Kr	^{83}Kr/^{84}Kr	^{86}Kr/^{84}Kr	^{84}Kr/^{132}Xe
Tombigbee River	373.0	0.0560	0.0548	0.2093	0.2036	0.2941	18.51
Costilla Peak	6660	0.077	0.165	0.357	0.381	0.298	5.85
Carbo	2297	0.062	0.156	0.357	0.389	0.290	8.54
Misteca	213	0.0094	0.0422	0.206	0.206	0.307	2.52
Xiquipilco	144	0.0063	0.0417	0.208	0.204	0.301	11.28
Cape York	143	0.00625	0.0405	0.204	0.202	0.303	4.28
Spallation	—	2.144	4.644	6.424	7.576	0.001	—
Atmosphere	—	0.00616	0.0396	0.202	0.202	0.306	—
Solar Wind	—	0.00615	0.0397	0.203	0.202	0.307	—

TABLE 6

XENON ISOTOPIC RATIOS

Meteorite	$\frac{124_{Xe}}{132_{Xe}}$	$\frac{126_{Xe}}{132_{Xe}}$	$\frac{128_{Xe}}{132_{Xe}}$	$\frac{129_{Xe}}{132_{Xe}}$	$\frac{130_{Xe}}{132_{Xe}}$	$\frac{131_{Xe}}{132_{Xe}}$	$\frac{134_{Xe}}{132_{Xe}}$	$\frac{136_{Xe}}{132_{Xe}}$
Arispe	0.0216	0.0318	0.0968	1.047	0.1449	0.822	0.3627	0.3207
Babb's Mill	0.00404	0.00626	0.0711	0.980	0.1387	0.786	0.3937	0.3421
Bohumiltz	0.00772	0.00713	0.0821	1.056	0.1686	0.817	0.3801	0.3096
Braunau	0.0080	0.0093	0.0618	0.973	0.1669	0.782	0.3405	0.2906
Butler	0.00780	0.01020	0.0764	0.997	0.1670	0.790	0.3867	0.3191
Cedartown	0.00856	0.01056	0.0784	0.984	0.1568	0.795	0.3879	0.3428
Dayton	0.00881	0.00599	0.0862	1.019	0.1552	0.822	0.415	0.3435
Duchesne	0.0853	0.0765	0.1237	1.010	0.144	0.821	0.398	0.325
Edmonton	0.0121	0.0171	0.0925	1.086	0.1755	0.814	0.3916	0.330
El Burro	0.0498	0.0329	0.0915	1.272	0.153	0.933	0.398	0.323
Hoba	0.0110	0.01154	0.0792	1.035	0.1541	0.806	0.356	0.3081
Odessa	0.00454	0.00578	0.0655	0.979	0.1534	0.795	0.395	0.3453
Sierra Gorda	0.01444	0.01420	0.0963	1.048	0.1776	0.797	0.3457	0.2919

TABLE 6 (continued)

Meteorite	$\frac{124Xe}{132Xe}$	$\frac{126Xe}{132Xe}$	$\frac{128Xe}{132Xe}$	$\frac{129Xe}{132Xe}$	$\frac{130Xe}{132Xe}$	$\frac{131Xe}{132Xe}$	$\frac{134Xe}{132Xe}$	$\frac{136Xe}{132Xe}$
Tawallah Valley	0.00580	0.0081	0.0714	0.842	0.1555	0.811	0.3780	0.3294
Tombigbee River	0.0177	0.0278	0.1336	0.918	0.1426	0.735	0.377	0.308
Costilla Peak	0.136	0.153	0.236	1.136	0.152	0.965	0.389	0.320
Carbo	0.101	0.109	0.190	1.295	0.152	0.961	0.372	0.322
Misteca	0.0043	0.0042	0.072	0.971	0.151	0.787	0.387	0.325
Xiquipilco	0.0043	0.0041	0.076	1.04	0.157	0.805	0.381	0.312
Cape York	0.0040	0.0038	0.074	1.00	0.154	0.790	0.384	0.321

TABLE 7

INERT GAS ISOTOPIC RATIOS IN DIFFERENT

PHASES OF THE ODESSA IRON METEORITE

Sample	$^4He/^3He$	$^4He/^{20}Ne$	$^{20}Ne/^{22}Ne$	$^{21}Ne/^{22}Ne$	$^{20}Ne/^{36}Ar$	$^{36}Ar/^{38}Ar$	$^{40}Ar/^{36}Ar$	$^{40}Ar/^{38}Ar$
ODESSA								
Metal	3.606	171.9	1.164	0.932	1.501	0.716	29.24	20.94
Graphite	8.07	59.10	2.967	0.800	0.557	3.989	232.9	929
Troilite	5.806	87.0	0.947	0.851	1.335	1.380	155.2	214.3
DEELFONTEIN								
Metal	3.85	284	0.99	0.96	0.34	0.640	2.73	1.75
Graphite	4.65	213	2.50	0.76	0.26	1.82	133	242
Troilite	5.41	106	0.92	0.86	1.65	0.673	22.0	14.8

TABLE 7 (continued)

	$^{36}Ar/^{84}Kr$	$^{78}Kr/^{84}Kr$	$^{80}Kr/^{84}Kr$	$^{82}Kr/^{84}Kr$	$^{83}Kr/^{84}Kr$	$^{86}Kr/^{84}Kr$	$^{84}Kr/^{132}Xe$
ODESSA							
Metal	628.1	0.0273	0.0730	0.2122	0.2144	0.2928	1.675
Graphite	39.39	0.0166	0.0679	0.2052	0.1957	0.2983	5.873
Troilite	86.4	1.188	0.1059	0.2183	0.2313	0.2992	8.96
DEELFONTEIN							
Metal	—	←———— Atmospheric within 10% ————→					↗
Graphite	—	←———— Atmospheric within 10% ————→					↗
Troilite	359	—	0.10	0.22	0.61	0.30	25

TABLE 7 (continued)

Sample	$\frac{^{124}Xe}{^{132}Xe}$	$\frac{^{126}Xe}{^{132}Xe}$	$\frac{^{128}Xe}{^{132}Xe}$	$\frac{^{129}Xe}{^{132}Xe}$	$\frac{^{130}Xe}{^{132}Xe}$	$\frac{^{131}Xe}{^{132}Xe}$	$\frac{^{134}Xe}{^{132}Xe}$	$\frac{^{136}Xe}{^{132}Xe}$
ODESSA								
Metal	0.00454	0.00578	0.0655	0.979	0.1534	0.795	0.395	0.3453
Graphite	0.00976	0.00893	0.0705	1.010	0.1383	0.831	0.3946	0.3199
Troilite	0.0174	0.01551	0.0894	1.114	0.1512	0.816	0.414	0.330
DEELFONTEIN								
Metal	0.10	0.07	0.31	0.99	0.14	0.83	0.38	0.32
Graphite	0.005	0.005	0.078	1.04	0.156	0.79	0.39	0.33
Troilite	<0.01	<0.01	0.25	3.45	0.15	1.31	0.37	0.31

IV. DATA INTERPRETATION

A. Sources of Inert Gases in Iron Meteorites

The components of the inert gases in meteorites are conventionally organized into four broad categories: radiogenic, fissiogenic, spallogenic (or cosmogenic), and trapped. The components belonging to the first three categories are nucleogenic; that is, they originate in the nuclear processes of radioactive decay, fission, high energy spallation, and neutron capture. Trapped gas is usually the designation given to inert gas components in which contributions from in situ nuclear processes are either absent or have been corrected for. Of course, the atoms of trapped gas ultimately come from nuclear processes in stars.

Some of these inert gas sources will be briefly reviewed here, but in the discussion of individual meteorites more careful analysis will be given of possible production mechanisms. It is important to remember that the siting and elemental composition of any sample is crucial to its inert gas abundances and isotopic spectrum.

1) Radiogenic Components

Radiogenic ^{4}He will be produced in iron meteorites by the decay of ^{238}U, ^{235}U, and ^{232}Th:

$$^{238}U \rightarrow {}^{205}Pb + 8\ {}^4He \qquad t_{\frac{1}{2}} = 4.47 \times 10^9\ yr$$

$$^{235}U \rightarrow \, ^{207}Pb + 7 \, ^{4}He \qquad\qquad t_{\frac{1}{2}} = 7.04 \times 10^{8} \; yr$$

$$^{232}Th \rightarrow \, ^{208}Pb + 6 \, ^{4}He \qquad\qquad t_{\frac{1}{2}} = 1.40 \times 10^{10} \; yr$$

where $t_{\frac{1}{2}}$ indicates the half life of the original nucleus. The abundances of uranium and thorium in iron meteorites have only been determined for a handful of metal samples. The concentrations measured were extremely low, so the difficult analysis has not been widely undertaken. Bate et al. (1958) found the thorium abundance in two iron meteorites to be less than 10^{-2} parts per billion. Morgan (1971) estimated the concentration of uranium in the metal phase of iron meteorites as between 10^{-1} and 10^{-3} parts per billion based on a review of the uranium data. Although there have been investigators who have reported possible radiogenic ^{4}He components in their helium data (Lipschutz et al., 1965; Schaeffer and Fisher, 1959), in general this component provides a negligible contribution to the total helium concentration because of the large amounts of ^{4}He produced by other processes.

Another inert gas isotope which may be the result of radioactive decay is ^{40}Ar. Radiogenic ^{40}Ar will be produced from electron capture by ^{40}K 11.2% of the time. The other 88.8% of the time ^{40}K decays to ^{40}Ca by β^{-} emission, where the combined half life for these two processes is 1.28×10^{9} years. Unfortunately, atmospheric contamination is a very serious problem in the analysis of ^{40}Ar. Schultz et al. (1971) determined an upper limit on the amount of ^{40}Ar from the metal phase of three iron meteorites which could be due to a radiogenic component.

These upper limits were on the order of 2% or less. In most studies of iron meteorites the ^{40}Ar data is discounted because of the possibility of atmospheric argon having been adsorbed by the sample.

Radiogenic ^{129}Xe from the decay of ^{129}I ($t_{\frac{1}{2}}$ = 1.59 x 10^7 years) was first detected by Reynolds (1960) in a stony meteorite, Richardton. Excess ^{129}Xe has since been seen in many types of meteoritic samples, and Munk (1967a,b) measured an excess in iron meteorite metal samples which he attributed to this same radiogenic source.

2) Fissiogenic Components

Some of the heavy isotopes of krypton and xenon may be produced by fissioning nuclides. Wetherill (1953) measured the relative spontaneous fission yields of these inert gases from uranium and thorium. He found the following two spectra for the spontaneous fission of ^{238}U:

$$^{83}Kr: \, ^{84}Kr: \, ^{86}Kr = 0.048: \, 0.159: \, \equiv 1.00$$

and

$$^{131}Xe: \, ^{132}Xe: \, ^{134}Xe: \, ^{136}Xe = 0.076: \, 0.595: \, 0.832: \, \equiv 1.00$$

The possibility that xenon from the spontaneous fission of ^{244}Pu may be detectable in meteorites was first suggested by Kuroda (1960), and the first fission-like anomalies attributed to the decay of ^{244}Pu were seen in the Pasamonte meteorite in 1965 (Rowe and Kuroda). The mass spectrum of xenon from spontaneous fission in a laboratory

sample of ^{244}Pu was determined by Alexander et al. (1971). The yield was precisely what meteoriticists had predicted it would be:

$$^{131}Xe: \; ^{132}Xe: \; ^{134}Xe: \; ^{136}Xe = 0.251: \; 0.876: \; 0.921: \; \equiv 1.00$$

The krypton yield from ^{244}Pu is not as well known. It has been estimated by Hohenberg et al. (1967) that $(^{86}Kr/^{136}Xe)_f = 0.0025$.

3) Cosmogenic Components

Galactic cosmic rays consist primarily of protons (about 85%) with the remainder made up of alpha particles, stripped nuclei of higher atomic numbers, electrons, and gamma rays. They are believed to be isotropic, to have remained constant for at least the past 10^9 years and to have originated in supernovae. This high energy radiation (approximately 500 MeV to 100 GeV) produces inert gases by spallation. The incident protons strike target nuclei which will produce secondaries of high energy. The resultant cascade can produce all nuclei lighter than any of the target nuclei, but generally the greatest yield is at nuclei with mass similar to, but below, the target nucleus in combination with very light particles such as p, n, ^{2}H, ^{3}H, ^{3}He, ^{4}He, etc. These light particles are boiled off the excited target nuclei.

From this discussion it is clear that the elemental composition of the irradiated sample will determine which nuclei will be produced. The production of a given isotope inside the meteorite will pass through a maximum where the secondary cascade peaks, and then decreases due to

the increased shielding in the meteorite. Since the incident flux that a sample will be exposed to depends on its depth in the meteorite, the elemental and isotopic spallation ratios will vary inside the meteorite. The original locations of the presently analyzed iron meteorite samples in the parent meteoroid are unknown, and theories for deducing that position are notoriously inaccurate.

The most easily detected cosmogenic nuclei in iron meteorites are ^{3}He, ^{21}Ne, and ^{38}Ar, where the abundances of these isotopes are so low in most other inert gas components that the cosmic ray component will stand out. By correlating the inert gas measurements with the chemical composition of the meteorite, production rates of these nuclei can be established.

The cosmic ray production of nuclei in iron meteorites provides alternative methods for deriving their irradiation exposure times. In one method the observed abundance of a stable cosmogenic nuclide is assumed to have built up at a constant rate over the exposure period, and its rate of production is inferred from the radioactivity level of a cosmogenic radionuclide of similar mass. Several such combinations of stable and radioactive nuclides may be used: ^{21}Ne/^{26}Al, ^{36}Ar/^{36}Cl, ^{38}Ar/^{39}Ar, and ^{41}K/^{40}K. Another method involves using the abundance ratios of several stable cosmogenic nuclei of different atomic masses as indicators of the size of the meteorite and the position of the sample within it. With this information the production rates of the isotopes involved can be normalized and used to compute the exposure age.

Cosmic rays are emitted during solar flares and are also primarily protons. However, their energies are typically much lower (less than 50 MeV), so although they may produce inert gases in iron meteorites by spallation, their contribution to the total amount of gas is much less, if not negligibly small.

4) Trapped Gas Components

The formation of iron meteorites is assumed to result from the following sequence of events in the early solar system's history (Kelly and Larimer, 1977): condensation, oxidation, and accretion in the primordial solar nebula, with melting, segregation, and fractional crystallization in a parent body. It is probable that several distinct reservoirs within the solar nebula provided inert gases which became trapped in the meteorite parent bodies during condensation and accretion. It then becomes a question of whether or not these trapped gases will have remained in the metal phase following the melting and segregation of that phase in the iron meteorite parent body.

An inert gas component which would be presumably ubiquitous in the primordial solar nebula, and therefore a strong candidate for a trapped gas component in meteorites, would be a component typifying the solar inert gas composition. The solar elemental and isotopic composition is thought to be represented by the composition of the solar wind. The solar wind consists of low energy ions, protons, electrons, and neutrons which are continually streaming from the sun. Therefore, if one assumes

that the present day solar wind inert gas composition is representative of the inert gas in the primordial solar nebula, determination of the solar wind composition may indicate the composition of a trapped gas component in meteoritic samples.

During the Apollo missions a sheet of aluminum foil was exposed to the solar wind and returned to earth. From this foil the fluxes and elemental and isotopic ratios of the particles making up the solar wind were found (Geiss et al., 1972). While in space the meteorite parent bodies can be expected to similarly trap solar wind ions. However, because these are low energy particles, they will only be implanted in the outer skin of a meteoroid. Therefore, an implanted solar wind component could only be detected if a true surface sample could be found. This is highly unlikely for meteoritic samples since ablation removes the outer surface of the meteoroid during its passage through the earth's atmosphere.

Another inert gas component seen in many meteoritic samples resembles that of the terrestrial atmosphere, at least suggesting a possible primordial trapped gas reservoir of that composition. However, it has never been established conclusively that this composition occurs anywhere but on the earth. Terrestrial-like inert gas components may be non-indigenous and arise solely from atmospheric contamination.

Many other unusual inert gas components have been detected in carbonaceous chondrites. These may represent trapped gas components from direct stellar nucleosynthesis which have been heterogeneously

injected into the early solar nebula. These compositions will be con-
sidered further as they arise in the subsequent discussion.

As a complicating factor, any of the above inert gas composi-
tions may also be altered by physical processes. This may disguise
the fact that two or more apparent components are not actually distinct,
but are related by mass fractionation. Such processes include diffusive
redistribution and loss of inert gases from solid bodies, space erosion
by sputtering and mass-dependent trapping mechanisms such as adsorption
and the previously mentioned ion implantation. Actual nucleogenic
components may be obscured by being separated from the radionuclides of
target elements from which they were produced and subsequent homogeniza-
tion with ambient gas prior to, during, or after trapping in solids.

B. Helium, Neon, and Argon

1) Introduction

The helium content in meteorites was originally attributed to the radioactive decay of uranium and thorium. However, when quantitative measurements of the inert gases were made (Arrol et al., 1942), a number of the derived ages were greater than the estimates of the age of the solar system. It was then suggested by Bauer (1947, 1948a,b) and Huntley (1948) that the meteorites may have been subjected to cosmic ray bombardment while in space, and that this radiation may have induced the production of helium. Paneth et al. (1953) showed that cosmic rays did indeed produce measurable amounts of helium and that a depth effect existed due to successively larger amounts of shielding inside the meteorite.

This result stimulated further investigations into the interaction of cosmic rays with meteoroids. Cosmic ray neon was first discovered by Reasbeck and Mayne (1955), while evidence for cosmogenic argon was reported by Gentner and Zähringer (1957).

The realization that cosmic rays produced inert gases was important to those studying iron meteorites because the inert gas composition of iron meteorites can be expected to be dominated by such gas. Since the iron meteorites are highly differentiated and are thought to have gone through stages of melting and slow cooling, trapped gas is unlikely to have remained present in large concentrations.

In the cosmic ray bombardment of iron meteorites neon and argon
are formed as spallation products, but helium is produced primarily as
evaporated particles boiled off from excited nuclei. Since the concen-
tration of this cosmogenic gas is proportional to the length of time the
meteoroid is exposed in space, most studies of the light (i.e. helium,
neon, and argon) inert gases in iron meteorites have been aimed at deter-
mining their cosmic ray exposure ages. However, the interpretation of
the measurements is complicated by the possibility that the intensity
and energy spectrum of the cosmic radiation may vary with time and posi-
tion in space and that the size of a meteoroid may change gradually or
discontinuously. Also, included in the concentrations of the inert
gases may be unknown contributions due to gas of radiogenic or primordial
origin.

Nevertheless, deducing information concerning the cosmic ray
exposure history of meteorite samples from light inert gas data has been
the focus of a number of investigations (see Table 3). An extremely
important method of analyzing these results is consideration of those
correlations which appear in a diagram where the ratio of two cosmic ray
produced nuclides is plotted against the ratio of two others. When this
is done, the wide range of exposure ages and the uncertainties in the ab-
solute values of various isotope production ratios are eliminated for
samples of different meteorites. An example of such a plot is the
$^4He/^{38}Ar$ versus $^3He/^{21}Ne$ correlation diagram derived by Signer and Nier
(1960, 1962). Based on the work of Martin (1953), Signer and Nier

calculated and presented in the form of diagrams several functional relationships describing the spatial distributions of various cosmogenic yield ratios in iron meteorites of different sizes. Schultz and Hintenberger (1967) found similar correlations between the ratio pairs $^{3}He/^{4}He$ versus $^{4}He/^{21}Ne$ and $^{38}Ar/^{21}Ne$ versus $^{4}He/^{21}Ne$. They proposed that a quantity called the "effective radiation hardness" can be determined for a sample which would characterize its location within the pre-atmospheric meteorite. Combining this quantity with the theory of Arnold et al. (1961), the energy spectrum of the particles producing the spallogenic gas can be estimated.

It has been found by the investigators above and by others (Hintenberger and Wänke, 1964; Lipschutz et al., 1965) that while the majority of iron meteorites fit into such a system of correlations, deviations from the pattern often occur. In an analysis of 15 iron meteorites, Schaeffer and Zähringer (1959) and Fisher and Schaeffer (1960) found only 7 of their samples followed the "normal" spallation pattern indicated by the correlation plots. When "abnormal" behavior occurs for a meteorite it is taken as an indication that the sample has suffered an unusual irradiation history or that it contains an additional inert gas component. Since the 15 iron meteorites presently analyzed were in general selected for their low cosmic ray exposure ages, the presence of non-cosmogenic gas is more likely to be detectable in them.

2) Correlation Diagrams

Recently Voshage and Feldman (1978) have interpreted the light

inert gas data of 16 iron meteorites in terms of the trends suggested by
the various correlation plots mentioned in the preceding section as well
as plots used by other investigators. They found that 12 of their sam-
ples had relative abundances of the spallogenic inert gas nuclides which
could be completely described by a "primary correlation system" consist-
ing of six equations. Those six equations are:

$$^3He/^4He = (0.152 \pm 0.002) + (34.1 \pm 0.7)\,(^4He/^{21}Ne)^{-1} \qquad\qquad IV.\ (1)$$

$$^3He/^{38}Ar = (20.4 \pm 1.9) - (2.68 \pm 1.1) \times 10^{-2}\,(^4He/^{21}Ne)$$
$$+ (4.45 \pm 1.7) \times 10^{-5}\,(^4He/^{21}Ne)^2 \qquad\qquad IV.\ (2)$$

$$^{20}Ne/^{21}Ne = 0.937 \pm 0.010 \qquad\qquad IV.\ (3)$$

$$^{22}Ne/^{21}Ne = 1.072 \pm 0.011 \qquad\qquad IV.\ (4)$$

$$^{36}Ar/^{38}Ar = (0.795 \pm 0.03) - (0.82 \pm 0.18) \times 10^{-3}\,(^4He/^{21}Ne)$$
$$+ (0.88 \pm 0.26) \times 10^{-6}\,(^4He/^{21}Ne)^2 \qquad\qquad IV.\ (5)$$

$$^{40}Ar/^{38}Ar = f(T) \text{ where } f \text{ is determined by the decay of spallogenic}$$
$$^{40}K \text{ into } ^{40}Ar \text{ during the cosmic ray exposure age T.} \qquad IV.\ (6)$$

Assuming these six primary correlations it is possible to derive all
secondary correlations between ratios of the stable helium, neon, and
argon isotopes. Three of these secondary correlations have been impor-
tant in the study of the light inert gases in iron meteorites:

$$^{38}\text{Ar}/^{21}\text{Ne} = (34.1 \div 0.152 \cdot {}^{4}\text{He}/^{21}\text{Ne}) / \left[20.4 - 2.68 \times 10^{-2} \cdot {}^{4}\text{He}/^{21}\text{Ne} \right.$$
$$\left. +4.45 \times 10^{-5} \cdot ({}^{4}\text{He}/{}^{21}\text{Ne})^{2} \right] \qquad \text{IV. (7)}$$

$$^{38}\text{Ar}/^{21}\text{Ne} = ({}^{3}\text{He}/^{21}\text{Ne}) / \left[28.7 - 0.307 \cdot {}^{3}\text{He}/^{21}\text{Ne} + 1.92 \times 10^{-3} \cdot \right.$$
$$\left. \cdot ({}^{3}\text{He}/^{21}\text{Ne})^{2} \right] \qquad \text{IV. (8)}$$

$$^{4}\text{He}/^{38}\text{Ar} = -6426 \cdot ({}^{3}\text{He}/^{21}\text{Ne})^{-1} + 257 - 2.45 \, ({}^{3}\text{He}/^{21}\text{Ne})$$
$$+ 0.013 \cdot ({}^{3}\text{He}/^{21}\text{Ne})^{2} \qquad \text{IV. (9)}$$

Figures 5 through 10 are plots of the correlations indicated by equations IV. (1), IV. (2), IV. (5), IV. (7), IV. (8), and IV. (9), respectively. The solid curves are the trends Voshage and Feldman found for 12 of their 16 samples, and the error bars represent the errors given for each equation.

Table 8 is a compilation of those same isotopic ratios for the 15 meteorites analyzed in this study and the two mineral separates from Odessa. Since the error for a given ratio is quite similar throughout the set of samples, only a single range of errors is tabulated for each ratio. In general, the smaller the isotopic ratio, the smaller the error. The data from Table 8 are plotted in Figures 5 through 10 and labeled by meteorite according to the following symbols: Arispe (A), Babb's Mill (BM), Bohumiltz (BO), Braunau (BR), Butler (B), Cedartown (CT), Dayton (D), Duchesne (DU), Edmonton (E), El Burro (EB), Hoba (H), Odessa (O), Odessa graphite (OG), Odessa troilite (OT), Sierra Gorda (SG), Tawallah Valley (TV), and Tombigbee River (TR). In the corner of each

figure is a typical one standard deviation error in the ratios for the 15 meteorite samples and the two mineral separates.

Although Voshage and Feldman found that their data for neon suggested that the $^{20}Ne/^{22}Ne$ and $^{21}Ne/^{22}Ne$ isotopic ratios were constants in iron meteorite metal samples (equations IV. (3) and IV. (4)), other analyses show marked variations (e.g. Signer and Nier, 1962). Figure 11 is a three isotope correlation plot of the present neon data. This representation has proven to be a powerful technique in the resolution of the neon system in a wide variety of meteoritic samples. Any mixture of two independent components will lie on the line connecting the compositions of the two components, and similarly, compositions resulting from the arbitrary mixture of three components will lie within or on the periphery of the triangle whose vertices are the compositions of the three components. Shown in the figure is the averaged iron meteorite cosmogenic neon composition (Ne_c) and mixing lines of Ne_c with solar wind neon (Ne_{sw}; Geiss et al., 1972), with the theoretical prediction of pure ^{22}Ne (Ne-E; Black, 1972) and with the atmospheric neon composition (Ne_{atm}; Geiss et al., 1972).

3) Discussion

Easily the most striking feature of the Figures 5 through 10 is the general disagreement between the experimental data of this work and the predicted "normal" spallation pattern. Only the meteorites Arispe, Bohumiltz and Duchesne show consistent agreement, and even they, like

TABLE 8

Meteorite	$^{22}Ne/^{21}Ne$	$^{20}Ne/^{21}Ne$	$^{4}He/^{21}Ne$	$^{3}He/^{38}Ar$	$^{38}Ar/^{21}Ne$	$^{3}He/^{21}Ne$	$^{4}He/^{38}Ar$	$^{3}He/^{4}He$
Arispe	1.018	1.105	266.8	15.31	5.19	79.5	51.4	0.298
Babb's Mill	1.339	2.727	434.2	28.27	3.37	95.4	128.6	0.220
Bohumiltz	1.053	1.125	274.9	16.03	4.80	76.9	57.3	0.280
Braunau	1.106	1.833	289.0	9.58	3.68	35.2	78.6	0.122
Butler	1.036	1.183	355.7	189.6	0.528	100.1	674.0	0.282
Cedartown	1.309	1.052	87.4	7.50	2.66	18.0	32.8	0.229
Dayton	1.020	1.028	287.5	34.89	2.53	88.3	113.5	0.308
Duchesne	1.063	1.188	287.8	18.30	4.07	74.4	70.8	0.258
Edmonton	1.022	0.916	77.7	9.25	2.69	24.9	28.9	0.320
El Burro	1.016	1.056	347.0	19.27	5.22	100.7	66.4	0.290
Hoba	1.109	0.999	503.4	21.82	6.09	132.8	82.7	0.264
Odessa	1.073	1.249	214.7	51.22	1.16	59.5	184.7	0.277
Sierra Gorda	1.020	0.981	342.0	63.02	1.27	79.9	269.6	0.234
Tawallah Valley	1.033	1.133	255.8	52.42	1.56	81.8	163.9	0.319
Tombigbee River	1.022	0.910	56.1	13.04	1.40	18.2	40.2	0.325

TABLE 8 (continued)

Meteorite	$^{22}Ne/^{21}Ne$	$^{20}Ne/^{21}Ne$	$^{4}He/^{21}Ne$	$^{3}He/^{38}Ar$	$^{38}Ar/^{21}Ne$	$^{3}He/^{21}Ne$	$^{4}He/^{38}Ar$	$^{3}He/^{4}He$
Odessa Troilite	1.175	1.113	96.8	27.60	0.604	16.7	160.3	0.172
Odessa Graphite	1.250	3.707	219.1	16.28	1.67	27.2	131.3	0.124
Error	±0.024 to.029	±0.022 to.028	± 5 to 10	± 0.1 to .8	±0.08 to.2	± 0.9 to 2.5	± 0.7 to 1.5	±0.004 to.009

FIGURE CAPTIONS

The lines plotted on Figures 5 through 10 are those correlations deduced by Voshage and Feldman (1978) (see text). Typical one standard deviation errors in the measurements are indicated in the corner of each figure.

FIGURE 5. Plot of ^{3}He/^{4}He versus ^{4}He/^{21}Ne.

FIGURE 6. Plot of ^{3}He/^{38}Ar versus ^{4}He/^{21}Ne.

FIGURE 7. Plot of ^{36}Ar/^{38}Ar versus ^{4}He/^{21}Ne.

FIGURE 8. Plot of ^{38}Ar/^{21}Ne versus ^{4}He/^{21}Ne.

FIGURE 9. Plot of ^{38}Ar/^{21}Ne versus ^{3}He/^{21}Ne.

FIGURE 10. Plot of ^{4}He/^{38}Ar versus ^{3}He/^{21}Ne.

FIGURE 11. Three isotope correlation diagram for neon. Mixing lines of cosmogenic neon (Ne$_c$) are plotted with atmospheric neon (Ne$_{ATM}$), solar wind neon (Ne$_{SW}$) and pure ^{22}Ne (Ne-E).
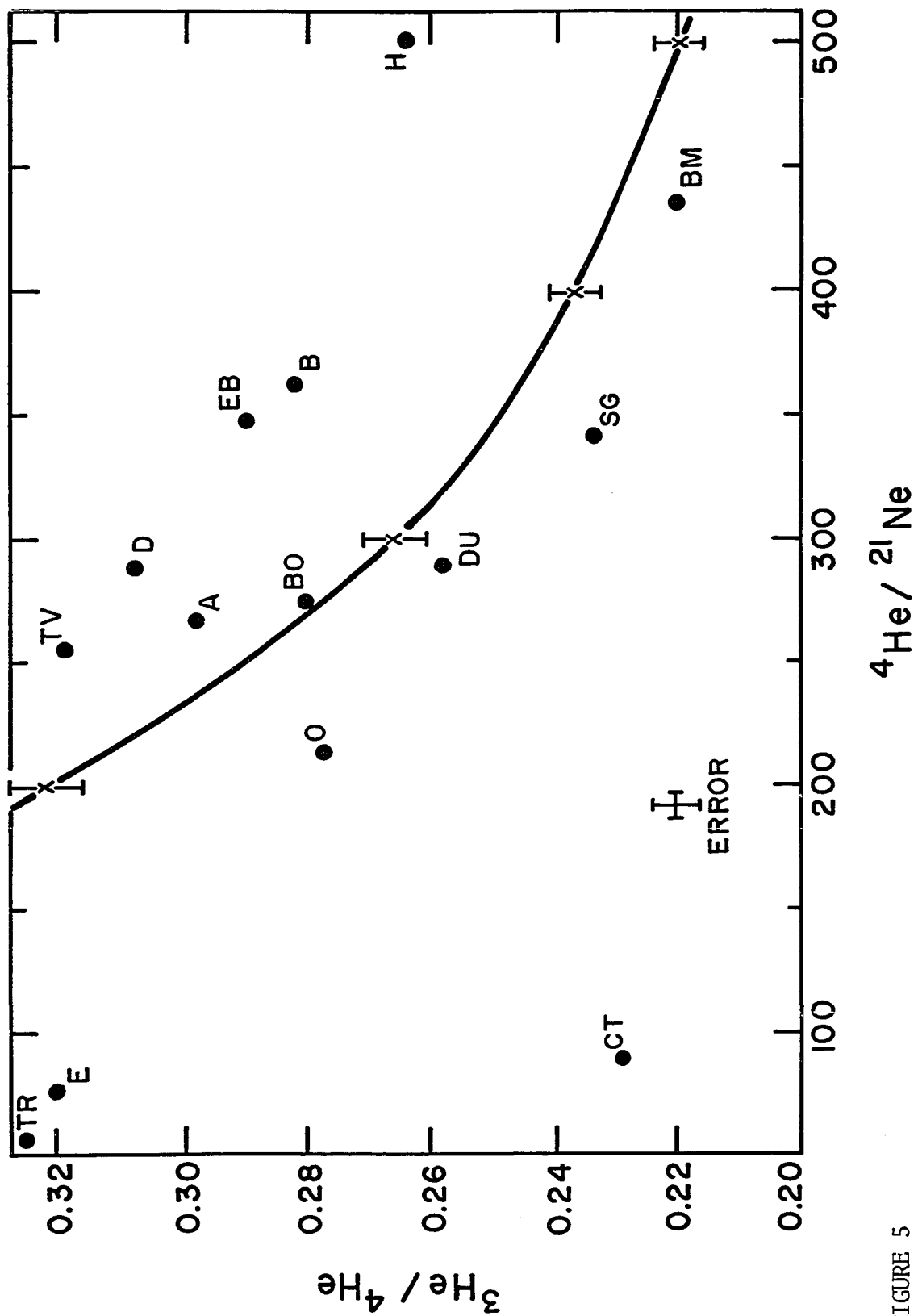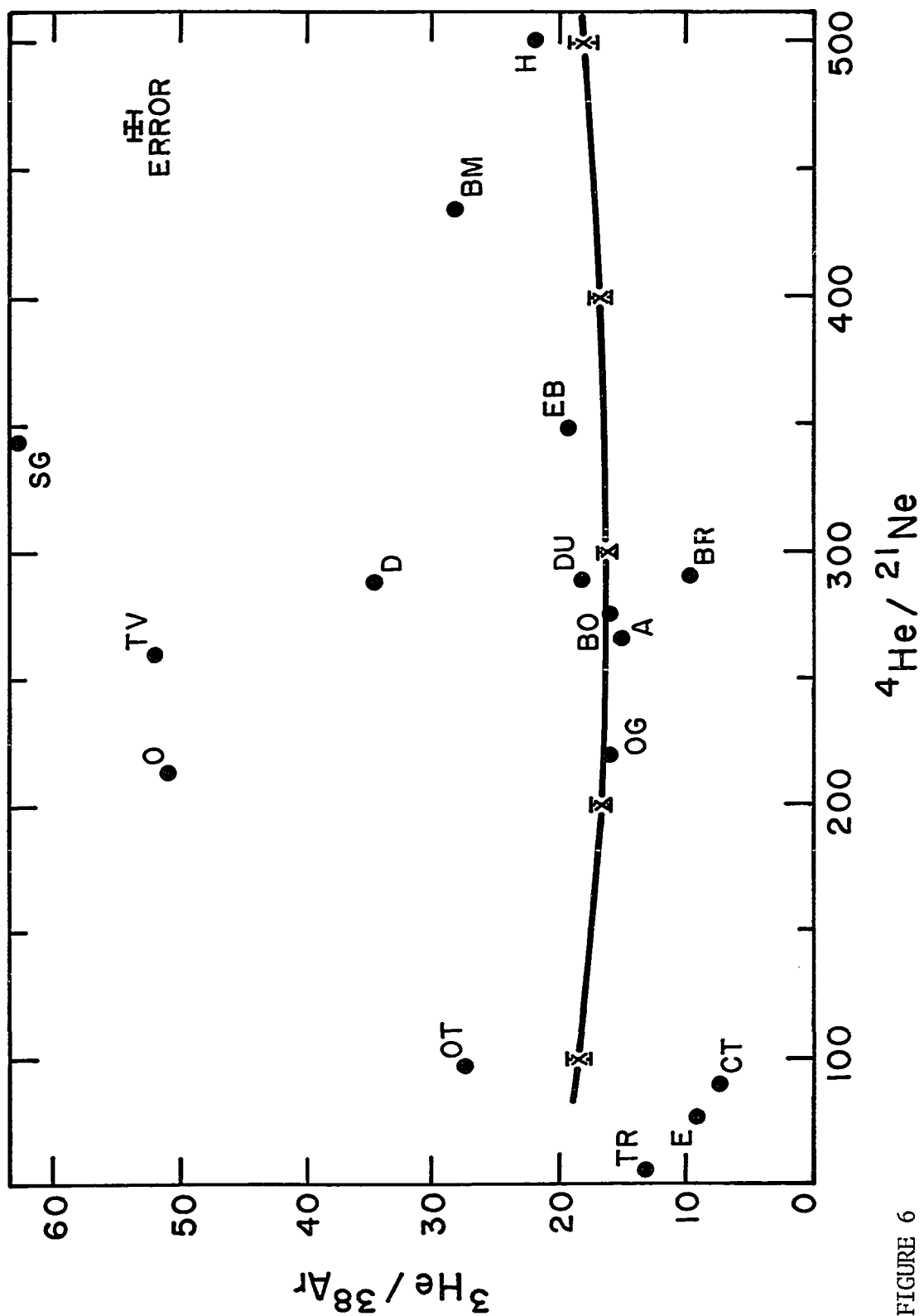
FIGURE 5

102
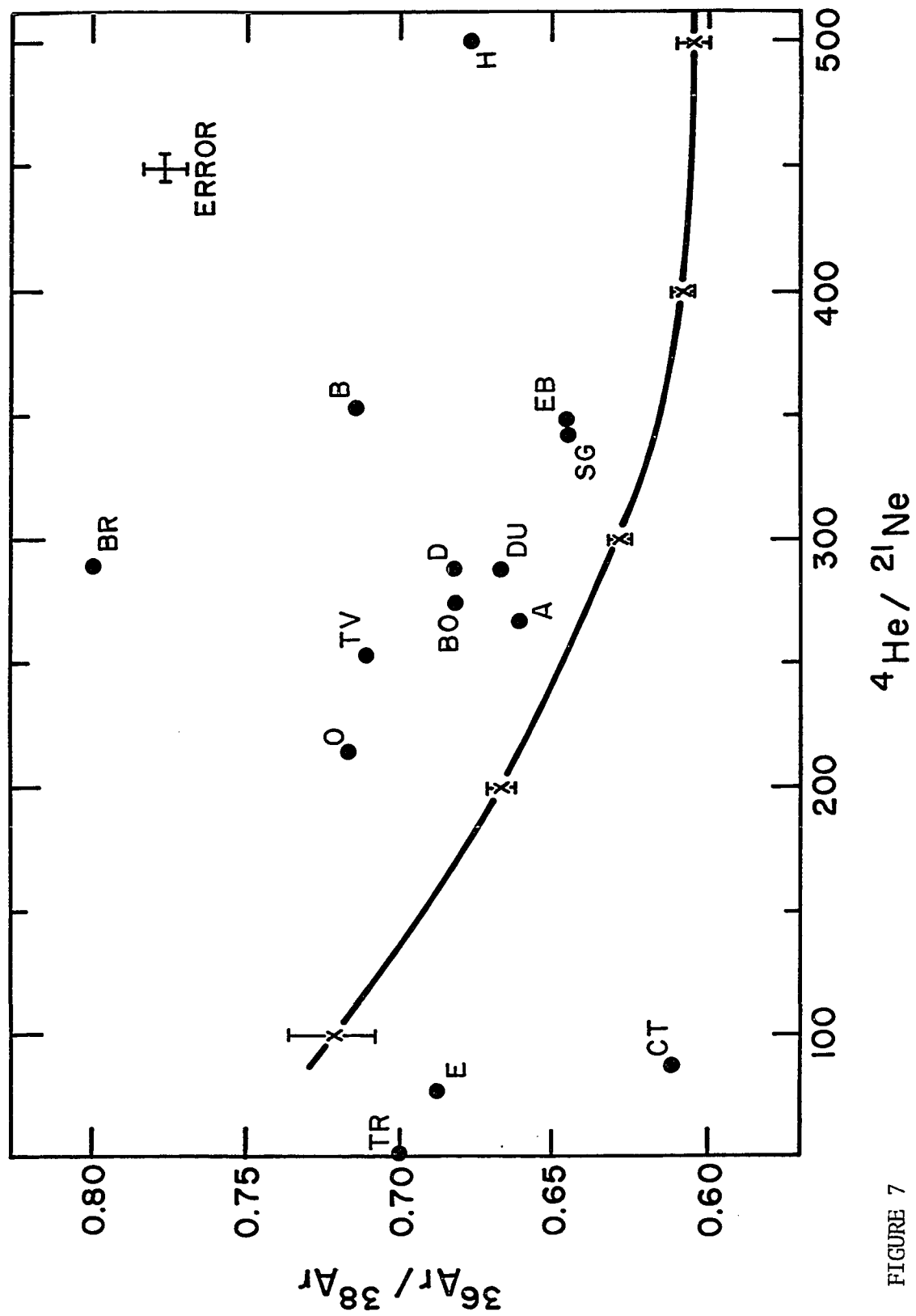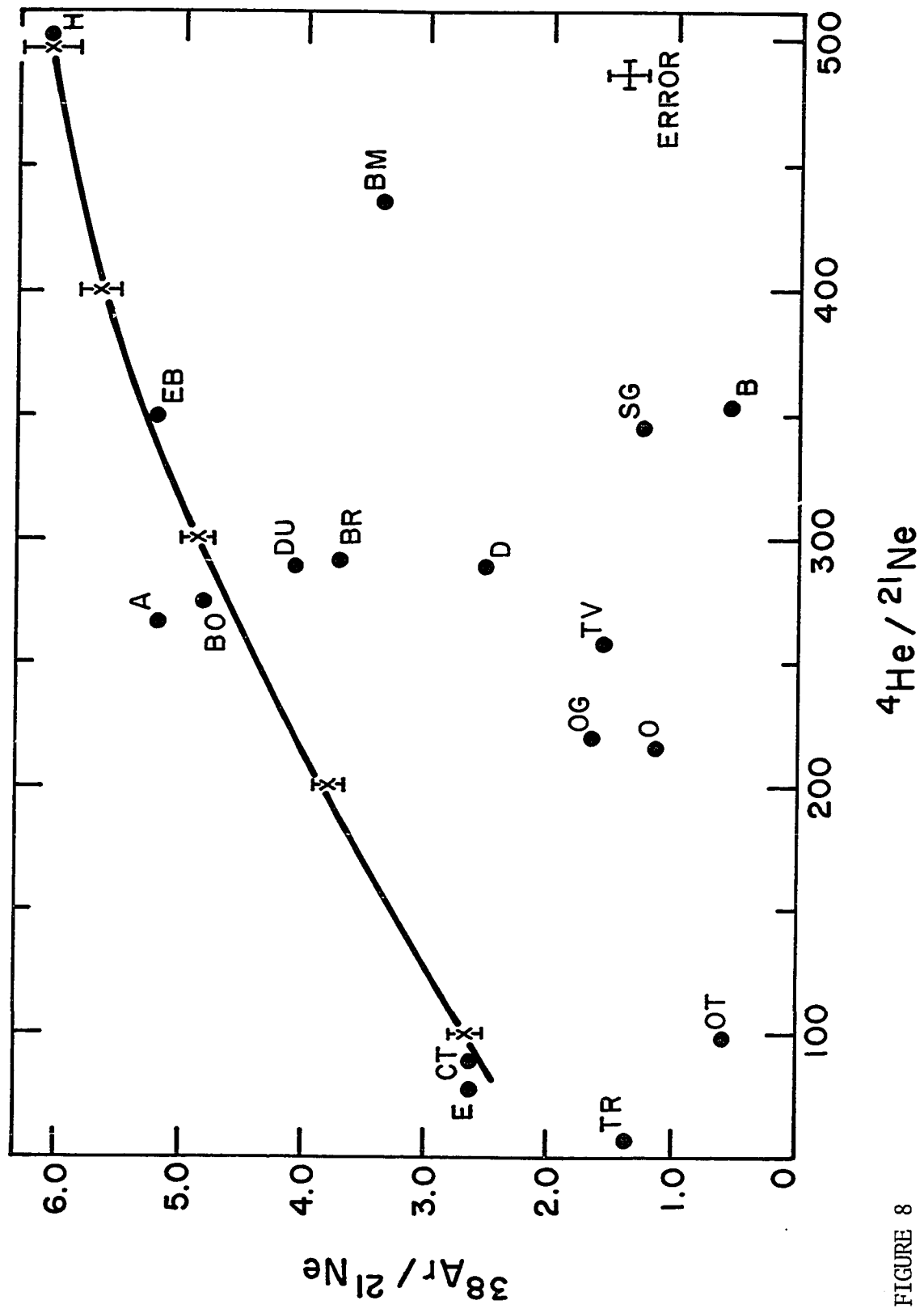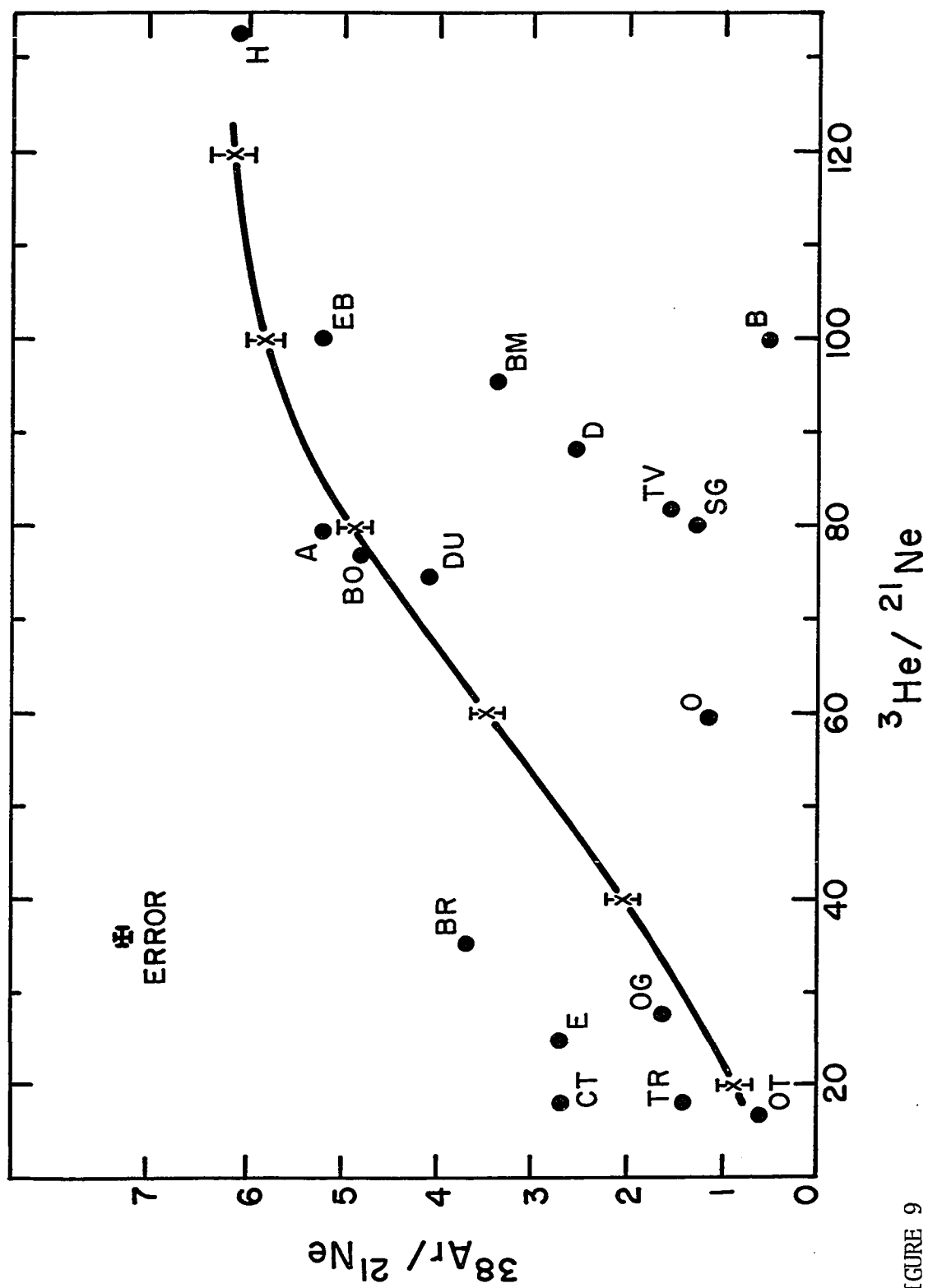
FIGURE 6

FIGURE 7

104

FIGURE 8

FIGURE 9

FIGURE 10
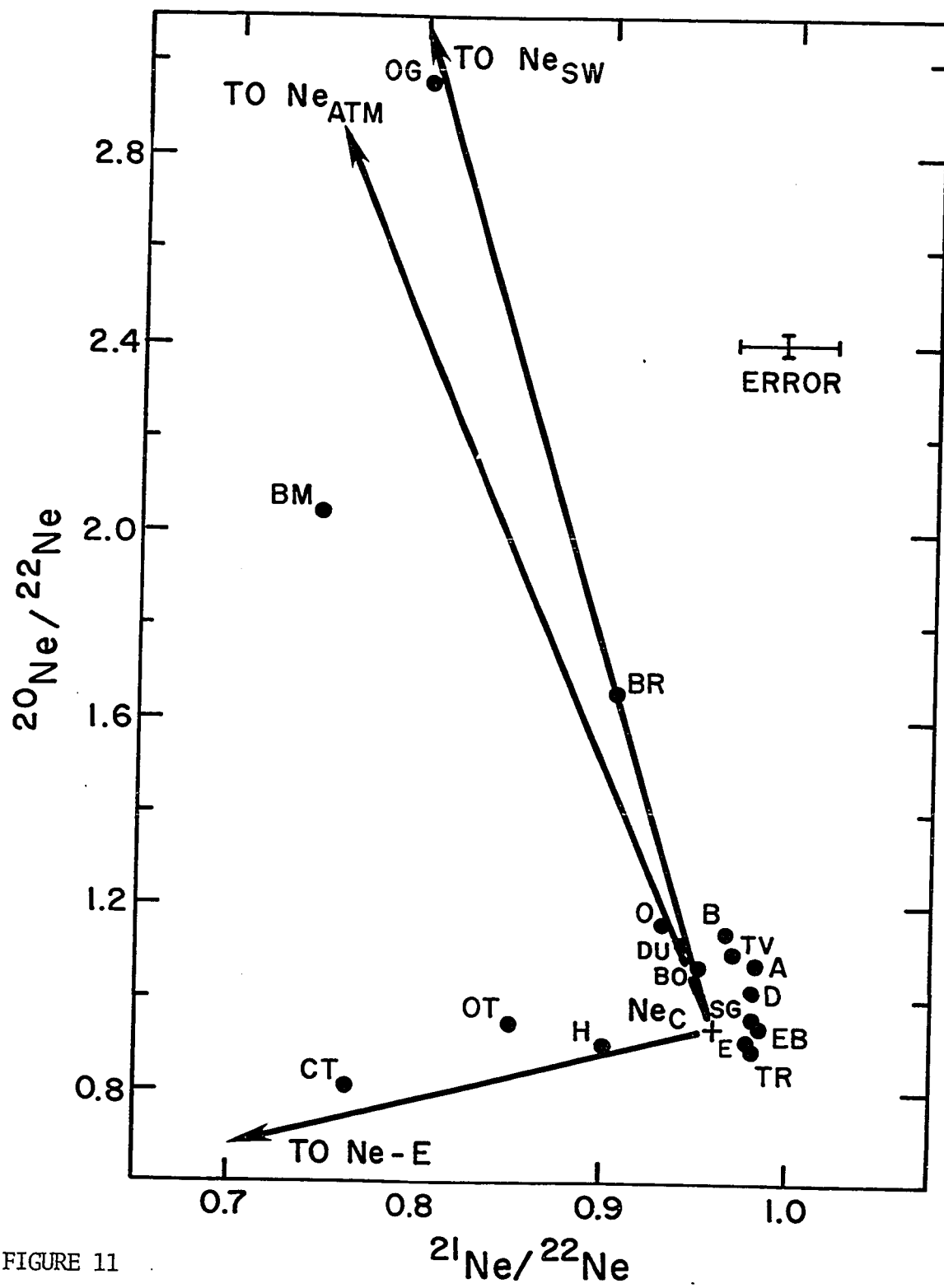
FIGURE 11

almost all of the meteorite samples, have higher $^{36}Ar/^{38}Ar$ ratios than that given by equation IV. (5). The meteorite El Burro fits most of the trends except for having a $^{3}He/^{4}He$ ratio which is slightly above the predicted curve.

These results underscore two primary general facts: first, that there is a wide variation throughout the literature in the composition and concentrations of the light inert gases reported among samples from the same iron meteorite; and secondly, that due to their generally low cosmic ray exposure ages, the meteorites studied in these experiments tend not to follow the spallation patterns as strongly as would a randomly selected distribution.

The first conclusion can be seen by considering other published data on these meteorites. Arispe, which as it was noted above falls consistently on or very near the correlation curves in Figure 5 through 10, was reported by Lipschutz et al. (1965) to contain the noble gases in very anomalous proportions. These investigators suggested that Arispe suffered a breakup some 100 million years ago and that it contains small amounts of either radiogenic or primordial ^{4}He. This conclusion is strengthened by the determinations of the cosmic ray exposure age, which fall into two groups: approximately 400 million years (Fisher and Schaeffer, 1960; Vilcsek and Wänke, 1962) and approximately 900 million years (Voshage, 1967). Thus it is obviously critical to know for a sample from this meteorite not only the depth from which the sample originated, but to which age group it belongs, because while Lipschutz

et al.'s analysis of Arispe finds the meteorite definitely anomalous with respect to Voshage and Feldman's (1978) predicted correlations, Fisher and Schaeffer (1960) and Hintenberger and Wänke (1964) agree with the present analysis which finds Arispe following the correlations.

Of the four meteorites which Voshage and Feldman (1978) find must have had "extraordinary irradiation circumstances" and thus did not fit their model, three, Bohumiltz, Cedartown, and Sierra Gorda, were also analyzed here. The anomalously high $^4He/^3He$ ratio which they find for Bohumiltz does not appear in either Hintenberger and Wänke's 1964 analysis or my own. On the side of consistency, the analyses of Cedartown (Hintenberger et al., 1967; Voshage and Feldman, 1978) and Sierra Gorda (Bauer, 1963; Voshage and Feldman, 1978) all agree with the present work in having somewhat high $^4He/^3He$ ratios.

Discordant results are not surprising when seen in the light of what has been generally observed in the cases where numerous analyses on different samples of the same iron meteorite were carried out — that is that there are significant variations in the concentrations and isotopic ratios of the light inert gases within the same iron meteorite, even for adjacent samples. Signer and Nier (1962) found what they termed "remarkable" variations among samples of the Washington County meteorite. The authors were unable to account for excesses of ^4He and ^{20}Ne which varied by more than a factor of five between samples. Heymann et al. (1966) studied 56 fragments of the Canyon Diablo iron meteorite by metallography and mass spectrometry. The concentration of ^3He varied

by a factor of 10^4, and in the 14 most gas-rich samples analyzed to determine the cosmic ray exposure age, the helium, neon, and argon isotopic ratios varied by more than 25%.

Herzog et al. (1976) measured the light inert gases in 21 Odessa iron samples and found that the helium, neon, and argon concentrations varied by factors of 62, 91, and 68, respectively, while $^4He/^3He$ varied by a factor of 2.55. Kolesnikov et al. (1972) found that the helium, neon, and argon concentrations in five fragments of the Sikhote-Alin iron meteorite all varied by factors of 22-29. These data yielded discordant cosmic ray exposure ages, which as in the case of Lipschutz et al.'s 1965 analysis of Arispe, was explained by collisional breakup of the parent meteoroid.

Even though these examples pertain to very massive iron meteorites, they caution against drawing general, let alone specific, conclusions from the analysis of single samples of iron meteorites without knowing their complete history: the cosmic ray exposure age of the parent meteoroid, whether or not the meteoroid suffered secondary breakups, the depth of the sample, the changes shock effects may have induced, etc. An attempt will be made to make sense of the data in the figures with this caution in mind.

In Figure 5 it can be seen that most of the samples are not too far removed from the curve of Voshage and Feldman (1978), and that the "band" in which they fall follows the trend of this curve. The figure also shows examples of what is the most commonly reported anomaly in the

light rare gas analyses of iron meteorite metal samples — a deficit of ^{3}He. Practically every investigation referenced thus far has found at least one such sample, and the cases of Cedartown and Sierra Gorda were mentioned earlier. The anomaly is most strikingly displayed in the Braunau meteorite, where the value of ^{3}He/^{4}He is so low (0.122, see Table 8) that it is not even shown in Figure 5. While almost all values of the ^{4}He/^{3}He ratio lie in the range 3.0-4.25, bracketing the spallation value of 3.80, the values published for Braunau are 13.18 (Bauer, 1963) and 9.71 (Hintenberger and Wänke, 1964). While my analysis gave a slightly lower figure of 8.20, it is still nearly twice the value of any other meteorite analyzed. Only the iron meteorite Washington County has such a large reported ^{3}He deficit (^{4}He/^{3}He = 14.3, Fisher and Schaeffer, 1959; 10.5, Signer and Nier, 1962; 22.7, Hintenberger et al., 1967).

The standard explanation for the ^{3}He deficit is that these meteorites were in more highly elliptical orbits which subjected them to greater than average temperatures near perihelion. This is thought to have caused the diffusive loss of spallation produced tritium ($t_{\frac{1}{2}}$ = 12.33 years) before it could decay to ^{3}He (Schultz, 1967; Hintenberger et al., 1967). Another explanation offered here is the following: ^{3}He has an uncommonly large (n,p) cross section, and an intense neutron irradiation at relatively high temperatures could therefore lead to ^{3}He loss via ^{3}H loss.

Hintenberger et al. (1967) noted a correlation between this ^{3}He deficit and the structural classification of the meteorite. Most

meteorites showing this behavior are hexahedrites, and this correlation is satisfied here for Braunau, Cedartown, and Sierra Gorda. Tombigbee River is also a hexahedrite which has previously shown high $^4He/^3He$ ratios ($^4He/^3He$ = 7.11, Fisher and Schaeffer, 1959; 7.04, Bauer, 1963). The data from Table 8 show no such deficit for this meteorite, with $^4He/^3He$ = 3.08.

Since ^3He and ^{21}Ne in iron meteorites are overwhelmingly from spallation, the higher the cosmic ray age of the sample, the further toward the upper left corner of Figure 5 (high $^3He/^4He$, low $^4He/^{21}Ne$) it should trend. This would lead to the prediction that the two most extreme samples, Tombigbee River and Edmonton, should have long cosmic ray exposure ages. This is borne out in the case of the Tombigbee River, but Edmonton is the only meteorite analyzed which has not had a prior determination of that age. As noted above, earlier measurements of the $^3He/^4He$ ratio by other investigators of Tombigbee River gave much lower values. Since the present ratio shows approximate agreement with the "normal" pattern, it is possible this sample originated from a greater depth in the parent meteoroid where the diffusive loss of tritium had not taken place. This conclusion is supported by the concentrations of the inert gases in Tombigbee River being the lowest overall of the meteorites analyzed.

Those samples with the oldest determined cosmic ray ages, Arispe. and Odessa, do fall on the correlation diagram where expected, as does the Babb's Mill meteorite, which has the lowest exposure age. So while

Babb's Mill has a low ^{3}He/^{4}He ratio of 0.220, it is normal in that it has a correspondingly high ^{4}He/^{21}Ne ratio.

A feature which shows up on all of the figures is the extreme location of the Hoba sample. The abscissa of Figures 5 through 10 all have ^{21}Ne in the denominator, and since Hoba's concentration of that nuclide is the lowest of those meteorites sampled, it always plots furthest to the right on the correlation diagrams. In Figure 5 Hoba shows a strong overabundance of ^{3}He; the same result could be obtained due to an underabundance of ^{21}Ne, but the later correlation diagrams contradict that interpretation.

Figures 6 and 8 are quite useful in detecting anomalous data because the variable along the ordinate is expected to change relatively little. Therefore, the large range of values seen along the ordinate in Figures 6 and 8 is striking. In Figure 6 the lower limit of the range of values lies near that of the "normal" correlation curve at ^{3}He/^{38}Ar about 17 for Arispe, Bohumiltz, Duchesne, and El Burro, and then trends upward to Sierra Gorda at a ratio of 63. Similarly, in Figure 8 the same four meteorite samples lie near the predicted ratio of ^{38}Ar/^{21}Ne of about 4.8, but the others trend down to Butler with a value of 0.53. Thus a large anomalous variation in the ^{38}Ar concentrations is evident, with a strong underabundance seen in Braunau, Butler, Dayton, Odessa, Sierra Gorda, and Tawallah Valley relative to that expected from the helium and neon concentrations. Butler had such a low abundance of ^{38}Ar that it does not appear on Figure 6, while Braunau, despite its large ^{3}He deficit, has

nearly a normal spallogenic ^{3}He/^{38}Ar ratio.

Three of the six meteorites showing a strong underabundance of ^{38}Ar have had argon measured in other samples of them previously. Schultz and Hintenberger (1967) report ^{38}Ar in Butler 17 times that presently seen; Schaeffer and Zähringer (1959) in Odessa 12 times; and Voshage and Feldman (1978) in Sierra Gorda of 3 times. The helium and neon concentrations from the present analyses are within a factor of two of all other investigator's results for Braunau, Butler, Dayton, Odessa, and Sierra Gorda. Tawallah Valley has had no previously published inert gas data.

With the agreement at helium and neon, but the disagreement in argon gas concentrations, a systematic experimental error could be suspected. However, the concentrations of helium, neon, and argon recorded all agree within a factor of two of other measurements on the Arispe, Babb's Mill, Bohumiltz, Cedartown, El Burro, Hoba, and Tombigbee River iron meteorites. This, and the variation of the discrepancies with other investigators (3 to 17-fold), seems to rule out a systematic error in the measurements.

There is additional support for this conclusion from the extensive studies of the Odessa meteorite. Helium concentrations varied by a factor of 6, neon by a factor of 5, and argon by a factor of 12 in measurements of these inert gases in Odessa by Schaeffer and Zähringer (1959), Signer and Nier (1962), Hintenberger and Wänke (1964), and Hintenberger et al. (1967). Herzog et al. (1976) have studied 21 Odessa samples. Several of their samples had helium, neon, and ^{38}Ar

concentrations similar to those found here. Therefore, my conclusion is that the ^{38}Ar differences seen in Figures 6 and 8 are real.

An underabundance of argon relative to the helium and neon concentrations would result if there has been incomplete gas extraction from the meteorites showing this anomaly. There are a number of arguments against that interpretation. Blank measurements were made following the meteorite sample runs, and in these the gas concentrations invariably dropped to less than 10% of the concentration recorded for the sample. Secondly, whenever the furnace was opened to clean out the fused residue, the crucible was always empty. Since all of the samples were entirely fused, the only other mechanism producing incomplete gas extraction would be if the fused metal retrapped gas as it was deposited on the furnace walls. However, if this retrapping had occured, there would be a consistent underabundance seen in all the samples analyzed.

One explanation for the variations in Figures 6 and 8 could be the presence of trace minerals. Until now the samples have been treated as if they were pure nickel-iron, which is an acceptable first order approximation. However, iron meteorites are known to contain inclusions, large and small, of silicates, sulfides, and phosphides. Although these minerals do contain iron atoms, the great majority of their atoms are oxygen, silicon, aluminum, magnesium, sulfur, and calcium. Now it is known that ^{3}He and ^{4}He yields from spallation do not depend very much on the target species for elements with $Z \gtrsim 6$ (carbon), hence the impurities should not affect the spallation helium much, if at all. However, it is

clear that ^{38}Ar cannot be formed from silicon, aluminum, magnesium or sulfur, whereas ^{21}Ne can be.

One might think that trace minerals cannot have much of an effect on isotopic yield ratios, but that is not necessarily true. Because the atomic weights of ^{21}Ne and ^{38}Ar are relatively far removed from those of the iron and nickel target nuclei, the yields of the former in the cosmic ray bombardment of iron and nickel are relatively small. In fact, the minimum of the mass-yield curve for spallation in iron is near ^{21}Ne. Also, the yield of ^{38}Ar is very sensitive to the calcium content of the sample. Calcium, although it does not reside exclusively in the phosphides, does occur primarily in the phosphide minerals of iron meteorites. Phosphide (called schreibersite in iron meteorites) occurs in the form of relatively small needles (approximately 100 x 10 μm) embedded in the metal phase, and its concentration is known to vary greatly from location to location (Buchwald, 1966).

However, there are difficulties in attributing all the observed deviations to varying proportions of trace minerals. If the apparent ^{38}Ar deficiency in these six meteorites is due solely to their having an underabundance of schreibersite, then Figure 8 implies that up to 90% of the "normal" spallation argon must come from that source. That such a large proportion of the spallation gas results from a trace mineral just isn't plausible.

The anomalies seen in Figures 6 and 8 could also be the result of the mixture of another inert gas component with the predicted

cosmogenic gas component. Figure 8 shows that mixing an atmospheric gas component with cosmogenic gas would not be suitable in that it would require a $^{38}Ar/^{21}Ne$ spallation yield ratio of less than $\frac{1}{2}$, which is highly unlikely in these meteorite samples.

The average inert gas isotopic ratios found in hypersthene chondrites (a common class of stony meteorites) were determined by Heymann (1967) as having $^{3}He/^{38}Ar \cong 40$ and $^{38}Ar/^{21}Ne \cong 0.14$. These gas compositions, when mixed with cosmogenic gas in Figures 6 and 8, respectively, can produce the observed range of values seen in those figures. However, it is difficult to understand why a stony meteorite gas component should be so prominent in iron meteorite metal samples. The data from Odessa, Sierra Gorda, and Tawallah Valley require that the analyzed gas be almost exclusively of that composition. Some of the meteorite parent bodies may have trapped inert gas with a composition similar to that in the chondritic meteorites, and despite the iron meteorite's subsequent evolution, they could retain a portion of that gas.

The most attractive hypothesis for the ^{38}Ar underabundance seen in Braunau, Butler, Dayton, Odessa, Sierra Gorda, and Tawallah Valley is a combination of varying trace mineral spallation contributions and the presence of a stony meteorite - like light inert gas component. It should be emphasized again that other investigators have reported similar underabundances in isolated cases.

Figure 7 contains an isotopic ratio, $^{36}Ar/^{38}Ar$, which can vary somewhat in spallation, but not as much as the range of values

(0.61 to 0.94) seen in these samples. Note that most of the abnormal samples fall above the "normal" spallation curve. The atmospheric $^{36}Ar/^{38}Ar$ ratio is 5.3. If the variation in this figure is due to an admixture of atmospheric argon, either of primordial or contamination origin, then one expects samples with low exposure ages to be the most anomalous, since their small spallogenic components will not as easily mask other components. That is the case here, with the two meteorites with the shortest ages, Babb's Mill ($^{36}Ar/^{38}Ar$ = 0.94, off the top of Figure 7) and Braunau, showing the largest $^{36}Ar/^{38}Ar$ ratios.

That the average cosmic ray exposure age of this set of meteorites is lower than the average for iron meteorites in general may be seen by a comparison of $^{36}Ar/^{38}Ar$ ratios. The average of $^{36}Ar/^{38}Ar$ in the present work is 0.70, whereas the average of 91 other determinations from the literature, which was taken as the cosmogenic argon yield ratio (Ar_c, Table 4), gives $^{36}Ar/^{38}Ar$ = 0.64. Thus another gas component is detectable in my samples. Most likely this component is atmospheric argon, which is normally overwhelmed by cosmogenic gas in iron meteorite metal samples.

Figures 9 and 10 strengthen the comments made earlier for Figures 6 and 8. Again, the presence of ^{38}Ar on the ordinate in both diagrams causes a large scatter of the data points. However, these figures do not present new relationships between the inert gas isotopes, since they result from secondary correlations. Figures 9 and 10 are shown because they have been used by some investigators of iron meteorites.

The three isotope representation $^{20}Ne/^{22}Ne$ versus $^{21}Ne/^{22}Ne$ is the only useful isotopic variation plot of the light inert gases. Helium has only two stable isotopes, and while argon has three, ^{40}Ar can vary because of ^{40}K decay. In the neon system there are no long-lived radionuclide precursors. This makes the neon isotopic system the most sensitive of the light inert gases for the detection of non-spallogenic contributions to the gas content.

Figure 11 shows that 12 of the 15 meteorites cluster around the cosmogenic neon (Ne_c) value, which means that they contain little if any neon from other possible neon gas components. Braunau and Babb's Mill show the definite presence of components with either a solar wind or an atmospheric neon composition, or both. Given the error, it is impossible to say firmly that Braunau and Babb's Mill contain neon of only atmospheric or solar wind composition, although the position of the Babb's Mill data point favors the former. As noted earlier, these meteorites have the shortest reported cosmic ray exposure ages of this set, so they are the most likely to be "abnormal" in Figure 11.

One may, of course, argue that both Babb's Mill and Braunau have been contaminated with terrestrial neon during their time on earth. However, the fact that these meteorites also indicate the presence of a trapped gas component in argon (Figure 7) makes that interpretation unlikely. By treating these meteorites as two component mixes of spallogenic gas and atmospheric trapped gas, the percentage of the primordial trapped component concentration relative to the total gas concentration

may be calculated. Of the total neon concentration, about 12% is due to trapped gas in Babb's Mill and 7.4% in Braunau. Of the total argon concentration, about 6.3% is due to trapped gas in Babb's Mill and 3.2% in Braunau. Thus it appears that spallation is approximately twice as efficient in producing argon from iron and nickel in these samples than neon.

The trend defined by the samples of Cedartown and Odessa troilite in Figure 11 is fascinating because it is in the direction of neon-E (Ne-E; see Black, 1972), a neon gas component which is apparently pure ^{22}Ne (Meier et al., 1980). There is now a consensus among cosmochemists that Ne-E is a record from direct stellar nucleosynthesis preserved in a class of stony meteorites called carbonaceous chondrites. The deviation of Cedartown in the direction of Ne-E in Figure 11 suggests that Ne-E, or a similar gas, may also occur in iron meteorites. Whether or not it is located in the metal phase or a trace impurity cannot be concluded from these results.

C. Krypton

1) Introduction

Krypton and xenon, the heavy inert gases, are present in meteoritic material only in very small concentrations. Even in stony meteorites the concentrations are on the order of 10^{-3} to 10^{-6} parts per million by mass and in iron meteorite metal samples the abundances often fall at least two orders of magnitude below that.

Relative to xenon, and certainly to helium, neon and argon, very few data are available on krypton in all meteorites. Meteoritic krypton isotope abundance measurements are more difficult experimentally than xenon measurements, not only because of hydrocarbon interference, which was discussed earlier in connection with ^{78}Kr, but because of atmospheric contamination. In the atmosphere the krypton to xenon ratio is about 12, as compared to stony meteorites where the value is about 1 and in the previous iron meteorite metal samples, where the ratio averaged about 6. A number of the subclasses of stony meteorites, ordinary, enstatite and carbonaceous chondrites, typically contain more xenon than krypton. Thus the background gas abundances relative to the sample abundances are distinctly unfavorable.

The overwhelming majority of krypton determinations which had been done prior to this study were on stony meteorite samples. The isotopic measurements on stony meteorites have resulted in the conclusion that many of these objects contain "trapped" krypton whose isotopic

composition is different from that of the terrestrial atmosphere (Eugster et al., 1967; Marti, 1967).

A second conclusion from these studies was that many of these meteorites have been exposed to relatively small, low energy (< 10 keV) neutron fluxes (Clarke and Thode, 1964; Marti et al., 1966; Eugster et al., 1969). These neutron fluxes caused anomalies to show up in krypton isotopes (notably 80 and 82) where neutron capture by bromine and selenium altered the isotopic ratios. Secondary neutrons from spallation reactions appeared to be able to provide the neutron fluxes required for this theory (Marti et al., 1966).

There has been some data published on krypton in iron meteorites, but most of it has been on their silicate, graphite, and troilite inclusions. The data from these studies will be discussed in section IV. E. in connection with the present analysis of mineral separates from the Odessa iron meteorite.

Thus it is not at all clear whether or not the conclusions reached for stony meteorites can be extended to include iron meteorite metal samples. Munk (1967a,b) found small amounts of krypton in the metal phase of three iron meteorites (Costilla Peak, Carbo, and Misteca; see Table 5), which he explained as the mix of a cosmic ray spallation component and a trapped component of atmospheric isotopic composition. The most abundant krypton producing spallation target elements in the meteorites analyzed were identified by him as zirconium, molybdenum, ruthenium, and palladium, and the resulting spallation spectra were distinct from

those of stony meteorites. Differences in the three meteorites were attributed to different degrees of cosmic ray shielding.

Hennecke and Manuel (1977) found the most distinguishing characteristic of the krypton in the two iron meteorite metal samples they investigated (Xiquipilco and Cape York; see Table 5) was that the light isotopes were preferentially enriched relative to the atmospheric standard. They concluded that by considering the iron meteorite's krypton composition as one extreme and that of carbon-rich residues of stony meteorites, in which the light isotopes are preferentially depleted, as another, mixtures of the two could explain the krypton in the earth's atmosphere, the solar wind, and the average of carbonaceous chondrites. Carbon-rich residues result from the acid treatment of carbonaceous chondrites, a subclass of stony meteorites thought to be in a primitive stage of evolution due to their lacking evidence of having been remelted. These meteorites will be further discussed with regard to the xenon data.

2) Correlation Diagrams

As was noted in the discussion of Figure 11, three isotope correlation diagrams have proved extremely useful in the resolution of compositions in the inert gases. The analysis is by necessity more complex for krypton and xenon, because now instead of three stable isotopes, as in neon, there are 6 and 9, respectively. Nevertheless, these diagrams have become the most common method used to distinguish between well understood isotopic variations and the puzzling isotopic anomalies

requiring further explanation.

Figures 12 through 16 are such correlation diagrams. As is the custom in the literature, ^{84}Kr is taken as the normalizing isotope in each plot. Since ^{84}Kr is the most abundant of the stable isotopes of krypton and can therefore be measured most accurately, it is a prime candidate for the normalizing isotope. In Figures 12 through 15 the ^{83}Kr/^{84}Kr ratio is plotted along the abscissa, and the ordinate ratios move progressively from ^{78}Kr/^{84}Kr to ^{86}Kr/^{84}Kr. ^{83}Kr is a useful choice for a persistant parameter because it is the only odd-A stable isotope of this even-Z element. It is more vulnerable to photoneutron emission and capture of non-thermal neutrons than the even-A isotopes. Hence it is a useful touchstone for a number of nuclear processes. Any mixture of two independent components will lie on the line connecting the components, and compositions arising from the mixture of three components will lie within the triangle whose vertices are the compositions of the three components.

The symbols used to label the meteorites from this work are the same as in the previous figures. Also shown are the data from Costilla Peak (CP), Carbo (C), and Misteca (M) (Munk, 1967a,b), as well as Xiquipilco (X) and Cape York (CY) (Hennecke and Manuel, 1977). The figures represent all the published data to date on krypton in iron meteorite metal samples.

Individual error bars are plotted for each meteorite in Figure 12 since there is no typical error for these data, but for the other

figures a single one standard deviation error estimate is given. The lines plotted on each graph are two component mixtures of atmospheric krypton and spallation krypton (see Table 5). The error in the mixing line is due only to the error in the calculated spallation spectrum, so the line may pivot about the atmospheric point slightly. The range of this variation is indicated by the cross-hatched regions in the figures.

3) Discussion

Always keeping in mind the large disparities found by investigators of the light inert gases in iron meteorites, some interesting trends are revealed by the correlation diagrams. First of all, the tentative conclusion of light isotope enrichment (^{78}Kr and ^{80}Kr) made by Hennecke and Manuel (1977) based on fragmentary data, is strongly supported. One of the important features of the present work is that it shows this anomaly in samples differing in cosmic ray exposure age as much as Butler and Babb's Mill do.

It is advantageous to first discuss those meteorites which are known to have long cosmic ray exposure ages. These may provide a good estimate of the spallation spectrum expected in iron meteorites, and deviations from that spectrum may then be the result of other krypton components present. Two of the meteorites analyzed by Munk (1967a,b) are useful in this regard: Carbo, which Signer and Nier (1962) report as having an exposure age of 600 ± 150 million years; and Costilla Peak which Munk (1967a) calculates from neon and argon abundances as having

FIGURE CAPTIONS

Figures 12 through 15 are three isotope correlation diagrams of krypton. The plotted line in Figures 12 through 14 is a mix of atmospheric krypton (triangle labeled ATM) with spallation produced krypton. The error in the spallation component (Munk, 1967b) is indicated by the cross hatched region. Typical one standard deviation errors in the measurements are indicated in Figures 13, 14, and 15.

FIGURE 12.   Plot of $^{78}Kr/^{84}Kr$ versus $^{83}Kr/^{84}Kr$.

Individual error bars are shown due to the wide variation in the one standard deviation errors.

FIGURE 13.   Plot of $^{80}Kr/^{84}Kr$ versus $^{83}Kr/^{84}Kr$.

FIGURE 14.   Plot of $^{82}Kr/^{84}Kr$ versus $^{83}Kr/^{84}Kr$.

FIGURE 15.   Plot of $^{86}Kr/^{84}Kr$ versus $^{83}Kr/^{84}Kr$.

The line is a least squares fit to the data shown.

FIGURE 15.   Plot of $^{84}Kr/^{132}Xe$ versus $^{36}Ar/^{84}Kr$.

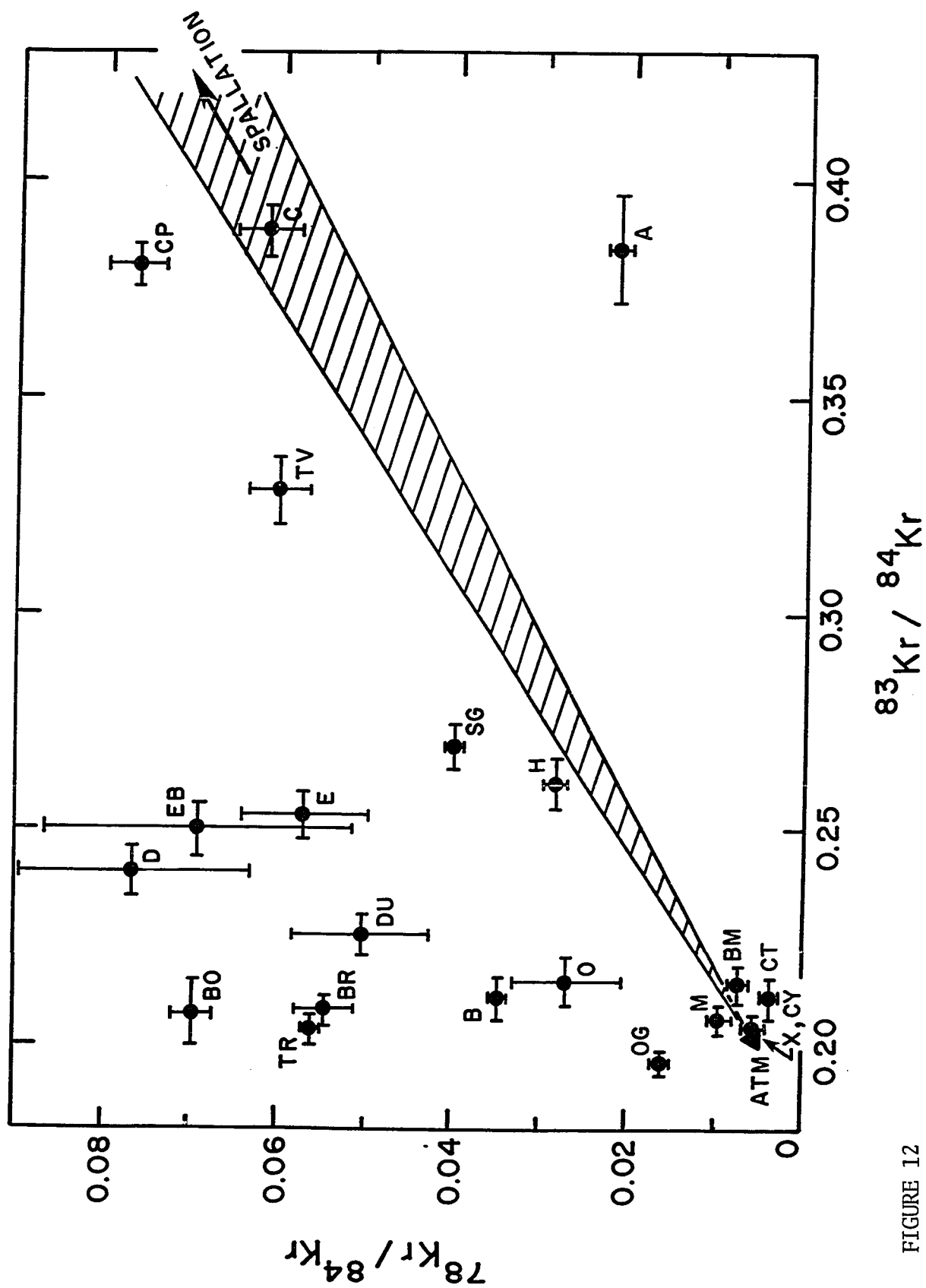The error in the measurements is smaller than the data points due to the scale used.
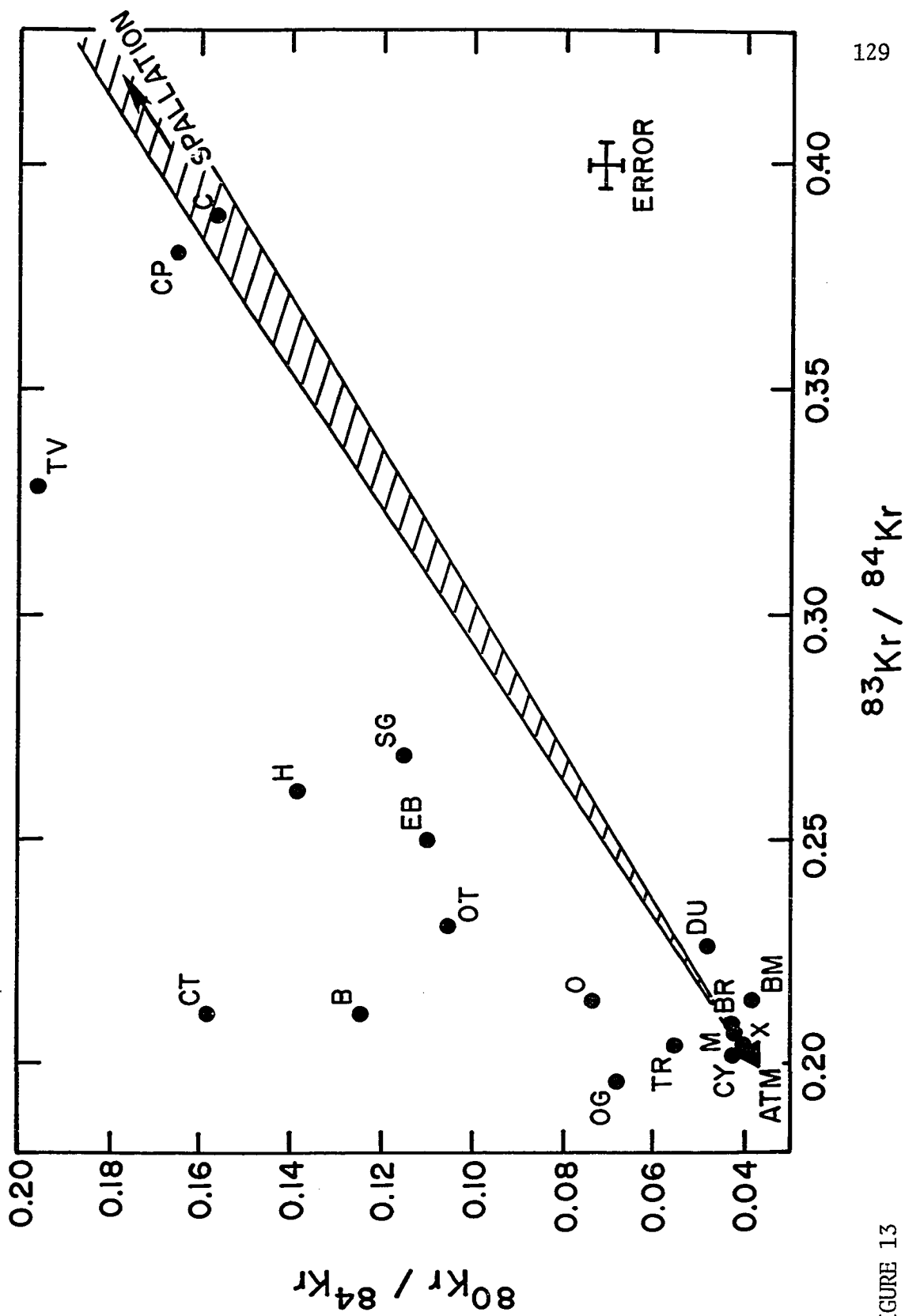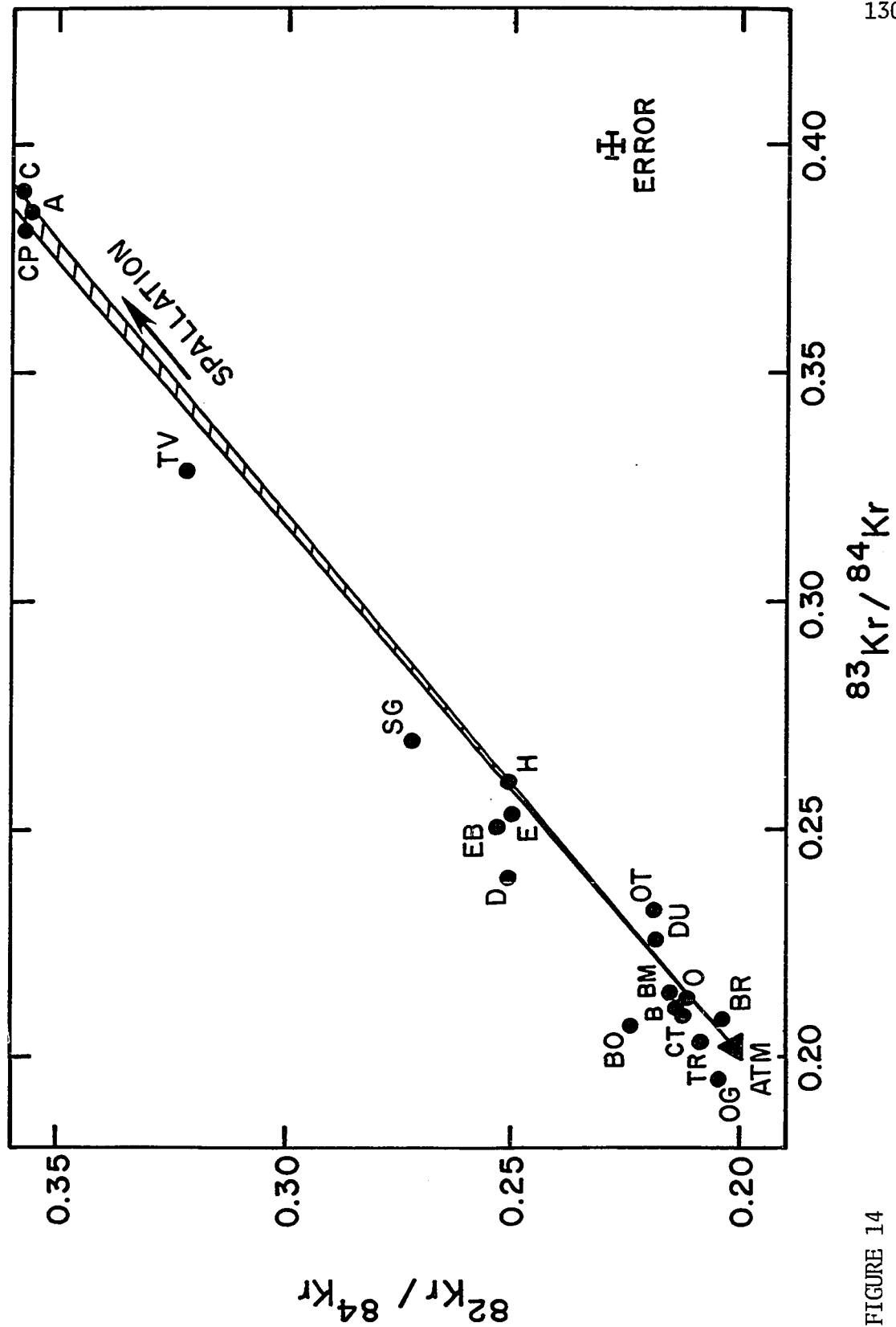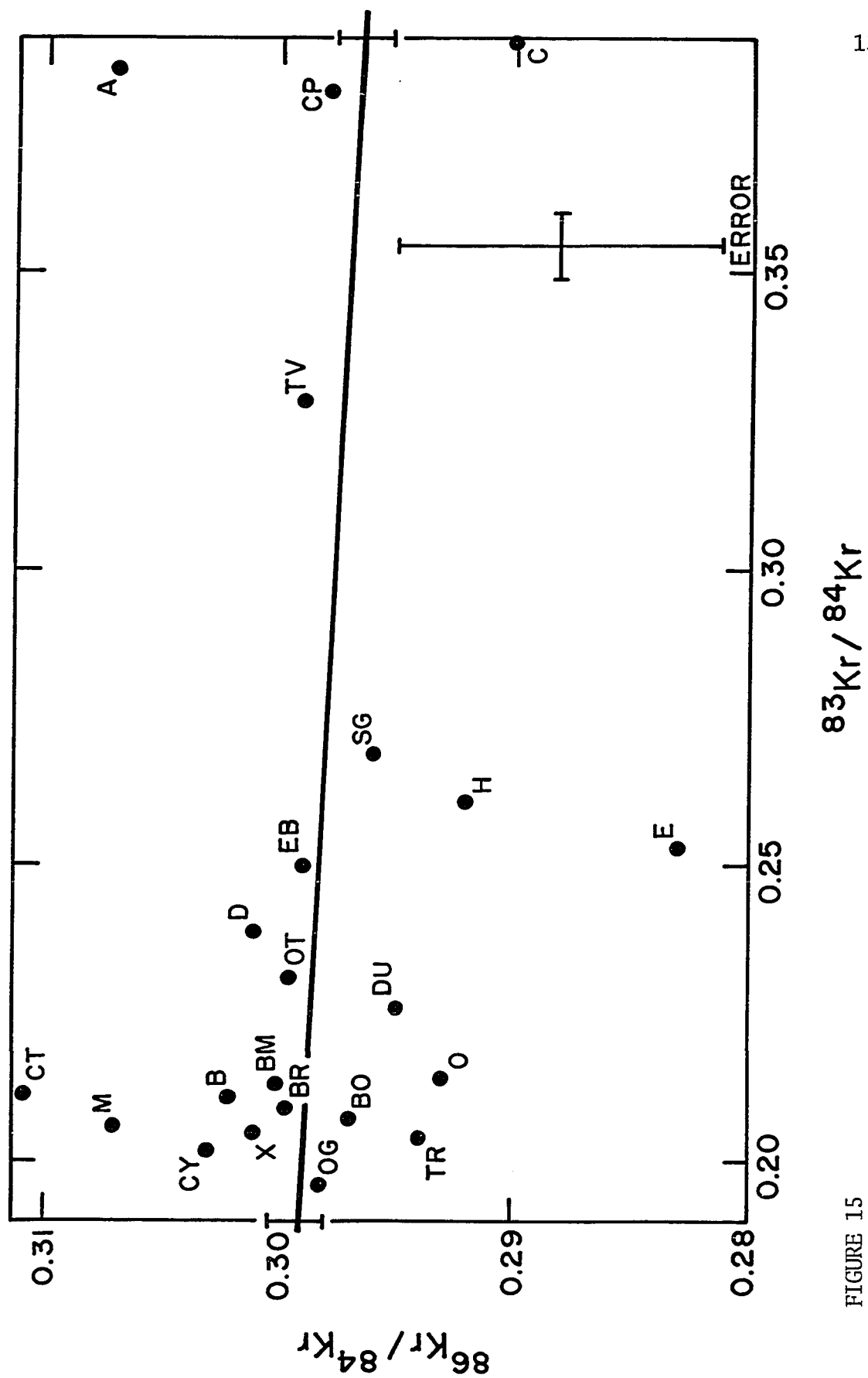
FIGURE 12

FIGURE 13

129

FIGURE 14

FIGURE 15
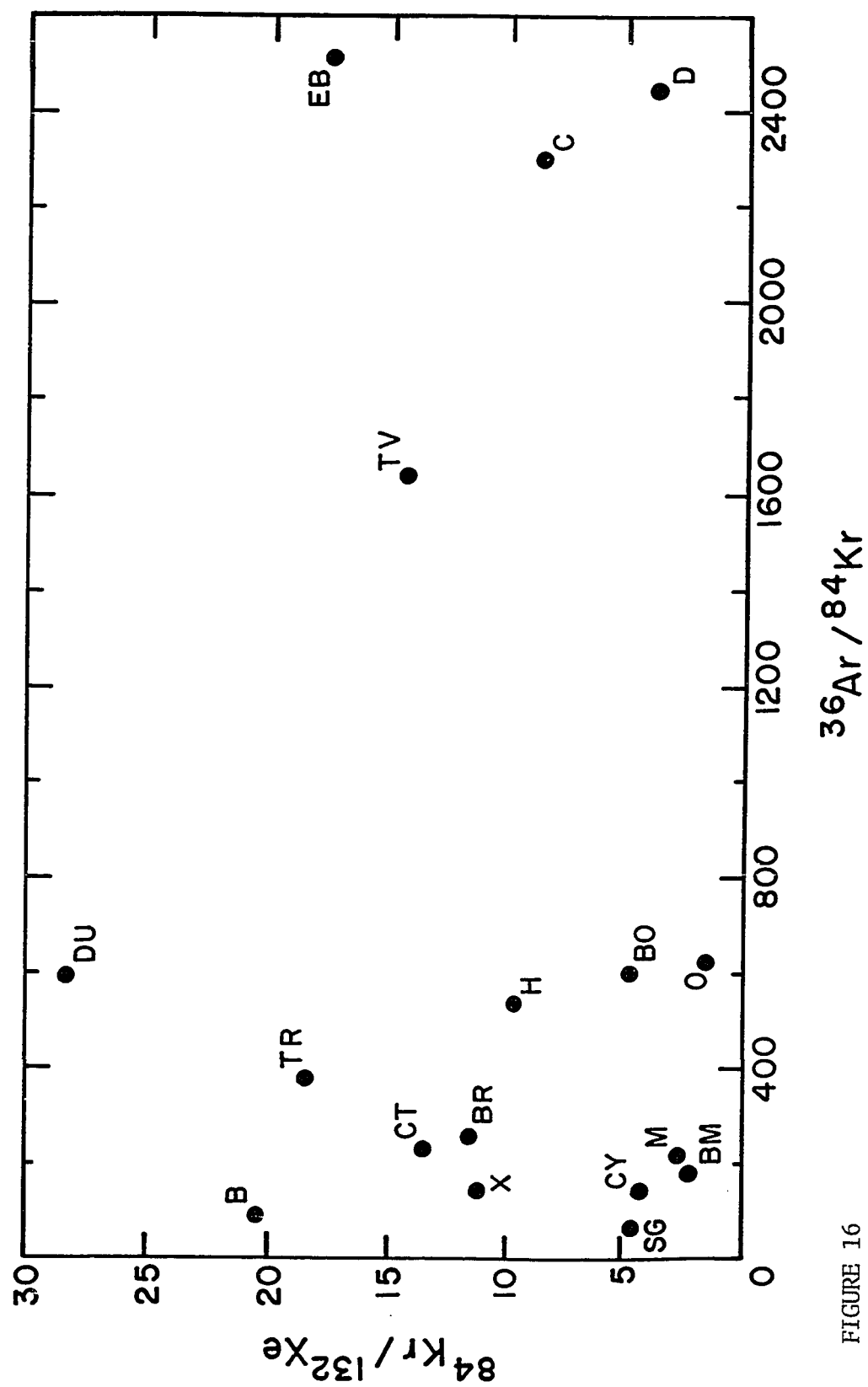
FIGURE 16

an exposure age of 530 ± 60 million years. These ages are greater than any of those for the samples presently analyzed except Arispe, whose average cosmic ray exposure age is 565 million years (see Table 3).

These three meteorites have the largest ^{83}Kr/^{84}Kr values and plot together well in Figures 14 and 15. In Figure 12 Arispe falls below the correlation curve, but I am reluctant to make much of a case for a single meteorite in this diagram. Arispe is, unfortunately, one of the three meteorites analyzed for which the ^{80}Kr/^{84}Kr ratio is questionable, and for that reason it is not plotted on Figure 13.

Munk (1967a,b) has calculated theoretical spallation yield ratios of krypton by using the empirical formula of Rudstam (1966) for the cosmic ray spectrum as deduced by Arnold et al. (1961) at a depth of 100 g/cm^2 in an iron meteorite. This theory predicts that the ^{86}Kr/^{83}Kr spallation ratio is less than 4 x 10^{-4}, consistant with radiochemical studies of spallation yields in this region of the periodic chart of the elements. The calculated spallogenic spectrum is listed in Table 5 normalized to ^{84}Kr. Here the spectrum is renormalized to ^{83}Kr, which is the most strongly produced cosmogenic krypton isotope:

$$^{78}\text{Kr}: \quad ^{80}\text{Kr}: \quad ^{82}\text{Kr}: \quad ^{83}\text{Kr}: \quad ^{86}\text{Kr} =$$

$$0.283: 0.613: 0.848: \equiv 1.00: 0.132: < 4 \times 10^{-4}.$$

This composition is distinct, but not greatly different, from that of Marti et al. (1966) deduced for stony meteorites:

$$^{78}\text{Kr}; \quad ^{80}\text{Kr}: \quad ^{82}\text{Kr}: \quad ^{83}\text{Kr}: \quad ^{84}\text{Kr}: \quad ^{86}\text{Kr} =$$

$$0.18: 0.49: 0.76: \equiv 1.00: 0.63: \equiv 0.$$

These differences are undoubtedly due to the different target nuclei from which krypton is formed in the two kinds of meteorites. It is important to keep in mind that differences in the calculated ratios in Table 5 and variations in Figures 12 through 15 may in part be due to varying proportions of the heavy trace element abundances. These abundances have been determined in very few iron meteorites.

Mixing lines of atmospheric krypton with the calculated spallation krypton composition are drawn in Figures 12, 13, and 14. These lines could be just as well described as mixes of solar wind krypton and spallation, since the solar wind and atmospheric krypton compositions are essentially identical (see Table 5). These definitely support the observation of Hennecke and Manuel (1977) that the krypton in iron meteorites is preferentially enriched in the light isotopes. The enrichment is unlikely to be due to spallation. This conclusion is clearly seen from both Figure 12 and Figure 13.

When dealing with ^{78}Kr one must always be cautious due to the large inherent error, but the variations seen among the meteorites are definitely significant. There is a tight clustering of five meteorites, Babb's Mill, Cedartown, Misteca, Cape York, and Xiquipilco near the atmospheric value. There is a second "grouping" of high ^{78}Kr/^{84}Kr but low ^{83}Kr/^{84}Kr ratios, which despite the large errors, are definitely enriched in ^{78}Kr. These meteorites are: Bohumiltz, Braunau, Dayton, Duchesne, Edmonton, El Burro, and Tombigbee River. The other meteorites do not deviate sufficiently from the mixing line to rule out a mix of an

atmospheric-solar wind krypton composition with spallogenic gas, although Arispe, as mentioned before, is distinctly underabundant in ^{78}Kr relative to Carbo and Costilla Peak.

Because the ^{80}Kr data are more reliable, the light isotope enrichment is more convincingly shown by Figure 13. There is again the same cluster of meteorites near the atmospheric composition, but now instead of Cedartown, Braunau plots at this location. The overabundance of ^{80}Kr is clearly seen in most other samples. The Edmonton meteorite has such a large ^{80}Kr/^{84}Kr ratio (0.229) that it plots off the top of the figure. The Hoba point is noteworthy in that this is the only correlation plot in which this meteorite does not fall on the mixing line of spallation with atmospheric-solar wind.

Figure 14 shows that if there are any true deviations from the mixing line, they are much smaller than in the previous figures. There might be excess ^{82}Kr in Bohumiltz, Dayton, El Burro, and Sierra Gorda. The data from the Cape York, Misteca, and Xiquipilco meteorites were not plotted here due to the congestion of points near the atmospheric-solar wind ratios. They too show very small possible enrichments of ^{82}Kr (see Table 5).

The Tawallah Valley meteorite has a large ^{83}Kr/^{84}Kr ratio and generally follows the spallation pattern in Figures 12 through 14. A combination of low sample gas concentrations and a relatively high blank measurement prior to its melting make the krypton data from this meteorite less precise, on the average, than for the others.

The line in Figure 15 is not a mixing line as before, since there is no spallogenic ^{86}Kr. Instead, the line is a least squares fit to the data. The ^{83}Kr/^{84}Kr ratio increases with increasing exposure age since the (^{83}Kr/^{84}Kr) spallation yield ratio is larger than 1.0. The ^{86}Kr/^{84}Kr ratio is equal to (^{86}Kr)$_{trapped}$ / $\left[(^{84}\text{Kr})_{trapped} + (^{84}\text{Kr})_{spallation} \right]$, and hence is bound to decrease. With little ^{84}Kr produced by spallation relative to ^{83}Kr, it is to be expected that the ^{86}Kr/^{84}Kr ratio will be nearly constant over a wide range of ^{83}Kr/^{84}Kr values.

The most striking property of krypton in iron meteorites is the apparent enrichment of the light isotopes ^{78}Kr and ^{80}Kr relative to atmospheric-solar wind krypton. Another possible interpretation is that the variations are due only to a deficiency of ^{83}Kr. If there were a deficiency in the amount of ^{83}Kr, then the data points in Figures 12, 13, and 14 would all be shifted to the left. In this case the samples could still have krypton which was the result of a mixture of atmospheric-solar wind and spallation components, but at some time in its history the meteorite, or the reservoir from which it derived its trapped gas, must have been subjected to a mechanism causing the selective depletion of ^{83}Kr.

To evaluate this idea quantitatively, first all the ^{86}Kr in the samples will be assumed as representing a trapped component of atmospheric composition. The Sierra Gorda meteorite will be used as an illustration because it appears to be deficient in ^{83}Kr in all the figures. The composition of Sierra Gorda after subtracting an atmospheric component

has the following spectrum:

^{78}Kr; ^{80}Kr: ^{82}Kr: ^{83}Kr; ^{84}Kr: ^{86}Kr =

0.047: 1.06: 1.04: ≡ 1.00: 0.39: ≡ 0.00

When this is compared to the spallation spectrum given earlier, it can be seen that a depletion of ^{83}Kr in the cosmogenic component by a factor of 1.9, on the average, will give the observed shift in the data of Sierra Gorda from the mixing lines in Figures 12, 13, and 14. If this same procedure is carried out for the other samples which do not follow the spallation pattern, only Braunau, Cedartown, and Duchesne cannot be similarly explained. The average depletion factor needed for ^{83}Kr in the cosmogenic component ranged from 1.9 for Sierra Gorda to almost 10 for Bohumiltz, but the depletion factor tended to fluctuate substantially from isotope to isotope within a given meteorite.

The fact that there does not emerge a common, constant depletion factor for all of the abnormal compositions is somewhat discouraging, but that does not necessarily disprove the assumption that ^{83}Kr is responsible for the variations in Figures 12 and 13. After all, the thermal neutron capture cross section of ^{83}Kr is the largest of any of the stable krypton isotopes, namely, 200 barns. For this reason it is logical to consider thermal neutron irradiation as the source of a ^{83}Kr depletion. Using Figure 13, the neutron flux required for such a depletion mechanism can be calculated. The use of Figure 13 is to be favored over Figure 12 simply because the data in Figure 13 are more accurate than those in Figure 12.

For the calculation the assumed original $^{83}Kr/^{84}Kr$ ratio for Sierra Gorda was read from Figure 13 as being about 0.32. If the shift in the $^{83}Kr/^{84}Kr$ value to the present $^{83}Kr/^{84}Kr$ ratio of 0.27 is due solely to neutron capture on ^{83}Kr, then the amount of ^{83}Kr converted to ^{84}Kr, $\Delta^{83}Kr$, in cm^3STP/g will equal:

$$\Delta^{83}Kr \ (cm^3STP/g) = (\text{neutron flux})(^{83}Kr_o)\sigma_{83}(t) \qquad \text{IV. (10)}$$

where the neutron flux is in neutrons/cm^2s, $^{83}Kr_o$ is the original concentration of ^{83}Kr in cm^3STP/g, σ_{83} is the thermal neutron capture cross section in cm^2 and t is the irradiation interval in seconds. The irradiation interval is assumed to be the cosmic ray exposure age of Sierra Gorda. The derived flux equals 1.4×10^5 neutrons/cm^2s, which is enormous relative to the 5 to 20 neutrons/cm^2s expected from secondary reactions in iron meteorites exposed to cosmic rays (Clarke and Thode, 1964). The average fluence necessary for this process to be the explanation of the anomalies in the Bohumiltz, Butler, Dayton, Edmonton, El Burro, Odessa, Sierra Gorda, and Tombigbee River samples is approximately 1×10^{21} neutrons/cm^2.

There are other problems besides the very large fluxes and fluences required by this mechanism, because there is no assurance that the neutrons available for capture have thermal energy. However, the resonant integral neutron capture cross section of ^{83}Kr is the same as its thermal neutron capture cross section. Furthermore, the resonant integral neutron capture cross section of ^{82}Kr is the same as that for ^{83}Kr,

200 barns, so that if one invokes higher energies than thermal, it will be ^{82}Kr which is depleted, rather than ^{83}Kr. As far as resonances are concerned, the largest resonances for both ^{82}Kr and ^{83}Kr are almost identical and occur at very similar energies: ^{82}Kr, σ(resonance) = 260 barns at E = 39.8 eV; and for ^{83}Kr, σ(resonance) = 290 barns at E = 27.9 eV (Mann et al., 1959). Thus if the thermal neutron capture cross sections are not used, only a very restrictive set of neutron energies (< 30 eV) must be taken to more strongly favor the depletion of ^{83}Kr.

Assuming for the moment that such large thermal neutron fluxes and fluences could have occured somehow, what other effects might be seen in krypton? Provided the abundance of bromine is high enough, excesses at ^{80}Kr and ^{82}Kr could be produced by neutron capture in ^{79}Br and ^{81}Br, respectively. Similarly, neutron capture in ^{82}Se could produce ^{83}Kr. Clarke and Thode (1964) have used this mechanism to explain excesses of these krypton isotopes in troilite (FeS) from the Canyon Diablo iron meteorite. However, the probable host mineral of bromine and selenium in iron meteorites would be troilite, so the concentrations they assumed in their calculations are much higher than that expected for iron meteorite metal samples.

Although the reported data are very sparse for these two elements in iron meteorites for the metal phase, Reed (1971) finds the average abundance of bromine as less than 0.1 parts per million, and Pelly and Lipschutz (1971) estimate selenium as having a concentration on the order of 0.05 parts per million. Clarke and Thode (1964) were especially hopeful that the selenium abundance might be high in troilite (maximum value

reported of 300 ppm in troilite, Kiesl and Hecht, 1969), because the neutron capture cross section of ^{82}Se is very low, approximately 0.04 barns.

Assuming typical abundances of bromine and selenium in the metal phase as 0.06 and 0.01 ppm, respectively, the effect of a large neutron flux may be estimated. ^{79}Br and ^{81}Br have roughly equal abundances (50.7% and 49.3%, respectively) and ^{82}Se represents 9.2% of the total selenium concentration. The thermal neutron capture cross section of ^{79}Br, ^{81}Br, and ^{82}Se are 10.7 barns, 2.66 barns, and 0.045 barns, respectively. Assuming the irradiation time and the derived neutron flux used previously to calculate the ^{83}Kr depletion in Sierra Gorda, this assumption would produce the following amounts of ^{80}Kr, ^{82}Kr, and ^{83}Kr in that meteorite:

$$^{80}Kr = 5.6 \times 10^{-8} \; cm^3 STP/g$$
$$^{82}Kr = 1.3 \times 10^{-8} \; cm^3 STP/g$$
$$^{83}Kr = 6.9 \times 10^{-12} \; cm^3 STP/g.$$

This is more than four orders of magnitude more ^{80}Kr and ^{82}Kr than that measured in the Sierra Gorda sample, and the ^{83}Kr produced would be a third of the total ^{83}Kr measured. There are undoubtedly other ramifications of such a strong neutron irradiation, but this is sufficient to discard that mechanism for depleting ^{83}Kr in situ (i.e. in the meteorite).

Since it has been shown that the transformation of ^{83}Kr to ^{84}Kr by the radiative capture of neutrons in situ cannot be the explanation

for the variations in Figures 12 and 13, there are only two viable possibilities which remain. One is that some primordial krypton reservoir was irradiated by such a strong neutron fluence prior to the incorporation of the gas into the meteorite parent bodies; the other is that the variations are not due to ^{83}Kr, but are due to excesses of ^{78}Kr and ^{80}Kr. The irradiation of krypton with neutrons prior to its trapping in meteorite parent bodies still requires the very large neutron fluences deduced in this section, i.e., on the order of 10^{21} neutrons/cm^2. Such neutron doses are generally associated with stellar nucleosynthesis, specifically supernovae. The irradiation of krypton in a supernova remnant cannot be excluded as a possible explanation, particularly because the bromine to krypton abundance ratio in such an environment, roughly estimated to be 0.3 (Cameron, 1973), is approximately seven orders of magnitude smaller than the abundance ratio in the metal phase of iron meteorites.

The other alternative is that ^{78}Kr and ^{80}Kr are the cause of the variations in Figures 12 and 13. As seen by the earlier calculation, one production mechanism of ^{80}Kr, ^{82}Kr, and ^{83}Kr is neutron capture in bromine and selenium. If that calculation is repeated, except now using a neutron flux of 5 neutrons/cm^{2}s, as would be expected from cosmic rays (Clarke and Thode, 1964), the amounts of ^{80}Kr, ^{83}Kr, and ^{83}Kr produced in Sierra Gorda would be:

$$^{80}Kr = 2.0 \times 10^{-12} \ cm^3STP/g$$
$$^{82}Kr = 5.0 \times 10^{-13} \ cm^3STP/g$$
$$^{83}Kr = 2.5 \times 10^{-16} \ cm^3STP/g.$$

This represents about 23% of the total ^{80}Kr measured in Sierra Gorda, 2.4% of the ^{82}Kr, and about 10^{-5} of the ^{83}Kr measured. When the measured ^{80}Kr and ^{82}Kr concentrations are adjusted by subtracting this component, the resulting isotopic ratios are ^{80}Kr/^{84}Kr = 0.089 and ^{82}Kr/^{84}Kr = 0.266. Both of these agree well with the two component mixing model on Figures 13 and 14 within the errors in the assumed bromine abundance, the assumed neutron flux, the exposure age uncertainties, and the error in the mixing line itself.

Because of the many inherent errors, it is not justifiable to draw more than qualitative conclusions for this production mechanism. However, these are interesting. The essentially equal abundances of ^{79}Br and ^{81}Br imply that the enrichment of ^{80}Kr relative to ^{82}Kr by this mechanism will be equal to the ratio of their thermal neutron capture cross sections, which is approximately four. This factor gives a good fit to the data points of Butler, Cedartown, El Burro, Hoba, Tawallah Valley, and Tombigbee River in Figures 13 and 14, as well as Sierra Gorda. The extremely high ^{80}Kr concentrations of Arispe, Bohumiltz, Dayton, and Edmonton may reflect high concentrations of bromine, either in the metal, or in small troilite inclusions imbedded in the samples. The low concentration of ^{82}Se in combination with its very low neutron capture cross section rules it out as a production mechanism of ^{83}Kr.

However, this process does not address the observed ^{78}Kr enrichments. There is the possibility that the spallation spectrum derived may not accurately predict the production of this isotope since the heavy

trace element abundances are not well known. Shifting the atmospheric-solar wind and spallation krypton mixing line toward higher $^{78}Kr/^{84}Kr$ ratios would fit all the data better except that of Arispe, which is already anomalously low, although only an unrealisticly large $^{78}Kr/^{84}Kr$ spallation ratio would give good agreemant.

A totally different production mechanism for the ^{78}Kr and ^{80}Kr enrichments involves direct stellar nucleosynthesis considerations. According to current thinking, bypassed p-isotopes such as ^{78}Kr are formed by photodisintegration of an inventory of nuclei from the atomic mass range 70-200 in massive stars (Heymann and Dziczkaniec, 1980). Heymann and Dziczkaniec (1980) have pointed out that stony meteorites, especially carbonaceous chondrites, are deficient in these isotopes if these meteorites are contaminated with krypton from the oxygen burning shell of a single supernova which exploded near the nascent solar system and perhaps triggered its formation (see Cameron and Truran, 1977). Heymann and Dziczkaniec (1980) have also suggested that matter from even deeper locations than the oxygen shell, specifically from the silicon burning shell of the star, could have large overproduction factors of ^{78}Kr and ^{80}Kr. Thus this single mechanism could produce both the ^{78}Kr and ^{80}Kr excesses observed.

It is unclear how such matter from a supernova would become part of an iron meteorite. The xenon data will not provide clues as to whether the ^{78}Kr and ^{80}Kr enrichments are the result of this mechanism because excesses in light krypton isotopes do not necessarily demand coherently

correlated excesses of the bypassed p-isotopes of xenon, which are ^{124}Xe and ^{126}Xe.

Finally, Figure 16 shows that there is no correlation between the krypton to xenon concentrations and the argon to krypton concentrations. The present experimental results confirm what was seen previously in this regard, as far as iron meteorite metal samples are concerned. Those samples with ^{36}Ar/^{84}Kr less than 600 range in ^{84}Kr/^{132}Xe from about 2 to 20. The samples with ^{36}Ar/^{84}Kr greater than 2200 range in ^{84}Kr/^{132}Xe from about 3 to 18. Arispe, Costilla Peak, and Edmonton plot off the right side of the diagram (see Table 3), and the error in the data points is negligible due to the scale used in the figure.

D. Xenon

1) Introduction

The analysis of xenon is by far the most complex of any of the inert gases. In general, xenon isotopes are formed by spallation, radioactive decay, and fission, or they can be from trapped gas. Hopefully a mix of these sources will provide an explanation for the differences observed when comparing the xenon data from meteorites with solar xenon and terrestrial xenon (Figure 17; after Podosek, 1978). The reference composition in Figure 17 is that of the solar wind (Eberhardt et al., 1970), with the nine stable xenon isotopes plotted on the abscissa. The ordinate delta values, δ_M^{130}, are defined as:

$$\delta_M^{130} \equiv 1000 \left[\frac{(M/130)_{sample}}{(M/130)_{solar\ wind}} - 1 \right]$$

IV. (11)

and are thus permil deviations from the solar wind composition.

The importance of the carbonaceous chondrites has been noted throughout the discussion of the inert gases, and the average xenon composition of carbonaceous chondrites (AVCC) is ubiquitous in all classes of stony meteorites. The AVCC xenon composition is taken as a standard for chondritic meteorites because of this pervasiveness. Nevertheless, it is now known that AVCC xenon is itself a mixture of a number of isotopically distinct xenon components, and hence the use of the AVCC composition as a reference standard must be handled carefully.

While the AVCC and solar compositions are virtually the same for the light fission shielded isotopes ^{124}Xe, ^{126}Xe, ^{128}Xe, and ^{130}Xe (Eberhardt et al., 1970, 1972; Podosek et al., 1971), there is a striking disparity at all masses between terrestrial and solar wind xenon. There is no general consensus as to the reason for this apparent steep mass fractionation. The differences at ^{131}Xe, ^{132}Xe, ^{134}Xe, and ^{136}Xe between solar and terrestrial xenon seem to be a continuation of the trend seen for the light isotopes, but deviations from the expected linear trend have been discovered which are attributed to nucleogenic components in either one or both of these gases. A fission source is suspected for these anomalies at the heavy isotopes (A > 130), but Podosek et al. (1971) have clearly demonstrated that this xenon cannot result from the fission of any known naturally occuring or man-made nuclei.

There is also an enrichment in the heavy isotopes of the AVCC composition, which is likewise indicative of a spontaneous fission component (Krummenacher et al., 1962). This component has been labeled CCF xenon for carbonaceous chondrite fission. However, as yet this component has not been identified as being the result of any known fissioning nuclei. This has prompted Anders and Heymann (1969) to suggest that the fissile parent is a superheavy element.

When analyzing carbonaceous chondrites by stepwise heating, Manuel et al. (1972) noted a strange isotopic effect: those fractions showing excesses in the heavy isotopes always had coherently correlated excesses in the light isotopes ^{124}Xe and ^{126}Xe. They proposed a two

component model in which this strange component, X, mixes with a complementary composition, Y, to explain these results. The X component is taken as evidence for primordial isotopic inhomogeneity of the solar system since a process for producing the component in situ has not been found.

Lewis et al. (1975) discovered this same unusual behavior with even greater variations than those found by Manuel et al. (1972) by analyzing the residue of the Allende carbonaceous chondrite after the meteorite had been treated by selective chemical dissolution techniques. They found that the inert gases were concentrated in a very small fraction (approximately 0.5% by mass) of the meteorite. In contrast to the above interpretation, however, this group of investigators has rejected the "X + Y" hypothesis, and has favored the heavy xenon isotope enrichment as being due to the fission of superheavy elements while the light isotope excesses would be due to very strong mass fractionation.

Pepin and Phinney (1980) have made a comprehensive study of the xenon problem in the entire solar system by utilizing not only the conventional two-dimensional, but also seven-dimensional correlation mathematics to define the xenon encountered in various solar system reservoirs. They concluded that the isotopic compositions of trapped xenon seen in meteorites, the earth's atmosphere, and the solar wind could be represented as a mixture of one or more of five components: cosmic ray produced xenon (CR-Xe), xenon from ^{244}Pu fission (Pu-Xe), and what one might call "primitive" components L-Xe, H-Xe, and U-Xe. There are also

sometimes contributions from the decay of ^{129}I to ^{129}Xe, ^{128}Xe due to neutron capture by ^{127}I, and fissiogenic $^{131-136}$Xe from the spontaneous fission of ^{238}U. Superposed on all these is the possibility of mass fractionation of any given component, which may alter gas compositions by non-nuclear processes, as discussed in section IV. A.

These components are listed in Table 9, along with the xenon isotopic compositions of the terrestrial atmosphere, the solar wind, and AVCC. The values given for spallation xenon are theoretically determined ratios by Munk (1967b) based on the empirical formula of Rudstam (1966) for the cosmic ray spectrum as deduced by Arnold et al. (1961) at 100 g/cm^2 depth in an iron meteorite. An additional component has been derived through the interpretation of stepwise heating data from a severly etched mineral fraction of the Murchison carbonaceous chondrite (Srinivasan and Anders, 1978). The patterns seen were suggestive of nuclear processes believed to take place in red giant stars, especially the s-process (neutron capture on a slow time scale), and so was labeled s-Xe. These are useful, but not necessarily all, possible ingredients for the analysis of xenon in my work.

A few comments about the ingredients of Table 9 are necessary. Ultimately all nuclei in the solar system are due to nucleosynthesis somewhere. For every type of nucleosynthesis, it is useful to distinguish between direct and delayed nucleosynthesis. The distinction cannot be perfectly sharp. It is based on the question of whether a specific radioactive (or fissile) nuclear species does or does not get

TABLE 9

XENON ISOTOPIC COMPOSITIONS

	^{124}Xe	^{126}Xe	^{128}Xe	^{129}Xe	^{130}Xe	^{131}Xe	^{132}Xe	^{134}Xe	^{136}Xe
1) ATMOSPHERE	2.337	2.180	47.146	649.58	≡ 100	521.27	660.68	256.28	217.63
2) AVCC	2.851	2.512	50.73	628.7	≡ 100	504.3	615.0	235.9	198.8
3) SOLAR WIND	2.99	2.67	50.45	634.5	≡ 100	495.5	607.0	225.8	184.2
4) U-Xe	2.947	2.541	50.873	628.7	≡ 100	499.58	604.79	212.88	166.34
5) H-Xe	0	0	0	—	≡ 0	0.073	0.249	0.7123	≡ 1
6) L-Xe	1.60	≡ 1	3.26	—	≡ 0	23.0	0	0	0
7) s-Xe	0	0	0.43	0.03	≡ 1	0.51	2.04	0	0
8) ^{244}Pu-Xe	0	0	0	≤2.6	0	25.1	87.6	92.1	≡ 100
9) ^{238}U-Xe	0	0	0	0	0	7.6	59.5	83.2	≡ 100
10) SPALLATION	0.780	≡ 1	1.203	1.184	0.041	1.425	0.005	10^{-5}	10^{-6}

REFERENCES:

1) Basford et al. (1973); 2), 4), 5), 6) Pepin and Phinney (1980); 3) Eberhardt et al. (1970); 7) Srinivasan and Anders (1978); 8) Alexander et al. (1971); 9) Wetherill (1953); 10) Munk (1967b).

involved in chemical and/or geological processes after nucleosynthesis, but before it decays quantitatively. If it does decay quantitatively, the synthesis of the daughter products is called direct; if it does not, then the synthesis of the daughters is called delayed. The formation of xenon from the fission of ^{244}Pu or a superheavy progenitor in the meteorite is an example of delayed nucleosynthesis.

A second distinction is between stellar and non-stellar nucleosynthesis. The only examples of the latter discussed in this work so far are the spallogenic components due to cosmic ray bombardment of the meteorite parent bodies while in orbit about the sun.

Although the solar wind composition, which has been studied well in lunar samples, only represents the long-term average composition of xenon in the solar wind reservoir of the sun, it is widely assumed that it represents xenon in the entire sun. For many years it has been assumed that the xenon composition in the sun also represents the composition of xenon in the solar nebula from which the solar system formed. The crux of Pepin and Phinney's (1980) work is that that is not so. These investigators claim that the xenon in the solar nebula was U-Xe. This acronym is derived from the German term "Ur-Xenon", i.e. "primeval xenon".

The normalizations of atmosphere, AVCC, solar wind, and U-Xe to ^{130}Xe $\equiv$ 100 are done so that isotopic ratios may be determined easily. H-Xe and L-Xe are first normalized by assumption to ^{130}Xe $\equiv$ 0, then renormalized to ^{136}Xe $\equiv$ 1.00 and ^{126}Xe $\equiv$ 1.00, respectively. The very

large ^{131}Xe/^{126}Xe yield ratio of 23.0 for L-Xe is probably erroneous (Pepin, private communication).

In the few previous studies of the xenon composition of iron meteorite metal samples, the behavior seen has not been greatly anomalous in the following sense. Munk's (1967a,b) analysis of the Carbo and Costilla Peak iron meteorites indicated that after subtracting a small trapped atmospheric component, based on the assumption that all the measured ^{136}Xe was due to such a component, the remainder of the gas agreed well with the predicted spallation yield from heavy trace elements. The small variations seen were attributed to different amounts of cosmic ray shielding. Hence these meteorites seemed to contain only atmospheric and spallogenic xenon.

Hennecke and Manuel (1977) combined their data for Cape York and Xiquipilco with that of Munk's (1967b) analysis of Misteca to construct correlation diagrams showing a marked similarity in the isotopic composition of xenon trapped in the earth and moon with that seen in these three iron meteorites for masses $^{128-136}$Xe. However, they found the ^{124}Xe/^{126}Xe ratio to be very consistent at 1.04 for these meteorites, while Munk's (1967b) calculated production ratio for spallogenic xenon is ^{124}Xe/^{126}Xe = 0.78. Because of this discrepancy, Hennecke and Manuel (1977) argue that there is an exotic trapped component in iron meteorites which shows up at the light isotopes ^{124}Xe and ^{126}Xe.

2) Correlation Diagrams

The data from Table 6 are plotted on Figures 18 through 23. The more traditional three isotope correlation diagrams are used rather than the seven isotope hyperplane mathematical analysis of Pepin and Phinney (1980). Pepin and Phinney's analysis is well suited for detecting compositions not on the hyperplane only when the experimental errors are much smaller than in this work.

The normalizing isotope along each axis in Figures 18 through 23 is ^{132}Xe. This is done because ^{132}Xe is the most abundant of the stable isotopes of xenon and can therefore be measured most accurately. Each figure has the ^{136}Xe/^{132}Xe ratio on the ordinate plotted versus one of the other stable xenon isotopes normalized to ^{132}Xe along the abscissa. The ^{136}Xe/^{132}Xe ratio is a useful choice as a persistent parameter because ^{136}Xe is not produced by spallation and ^{132}Xe is only very slightly produced by spallation (see Table 9). Thus, one xenon production mechanism may be eliminated immediately as the source for all large variations along the ordinate. The ^{129}Xe data are not plotted in the correlation diagrams because of the ambiguity arising from contributions to that isotope from ^{129}I decay.

The symbols identifying the meteorites are the same as used previously, and a typical one standard deviation error estimate is given in the corner of each diagram. The U-Xe, solar wind (SW), and atmospheric (ATM) xenon compositions are plotted on each figure and are distinguished by a square, circle, and triangle, respectively. Mixing lines are

drawn of U-Xe with the ^{244}Pu fission xenon (Pu-Xe) and H-Xe components. Also shown are trend lines for cosmogenic xenon (CR-Xe) and s-Xe; these indicate only the <u>direction</u> in which the addition of the component would shift a given point. This is to be distinguished from the true mixing lines. For example, if a sample were to be a mixture of U-Xe and atmospheric xenon <u>only</u>, it would have to lie on the plotted line between the U-Xe and atmospheric points.

Mixing lines of U-Xe with ^{238}U fission xenon are not shown on the figures due to their similarity with the U-Xe--Pu-Xe mixing lines. In all cases such a mixing line would either fall on the U-Xe--Pu-Xe mixing line (Figures 18 and 19) or between that mixing line and the one for U-Xe and H-Xe (Figures 20, 21, 22, and 23). In the second instance, the mixing line with ^{238}U would be much closer to the Pu-Xe mixing line than to the H-Xe line. Moreover, as was discussed in section IV. A., the uranium concentrations found in the metal phase of iron meteorites are only on the order of one part per billion by mass anyway.

3) Discussion

The variations in the xenon compositions are complex, as the figures clearly indicate. Figures 18 and 19 can be considered together since the trends they reveal are very similar. The isotopes on the abscissas, ^{124}Xe and ^{126}Xe, are the lightest of the stable isotopes and are thought to be formed only by either the p-process of stellar nucleosynthesis or by spallation. The spallation component is strongly evident in

FIGURE CAPTIONS

FIGURE 17.   Per mil deviations of the average xenon measured in
carbonaceous chondrites (AVCC) and atmospheric xenon
from the solar wind xenon composition.

Figures 18 through 23 are three isotope correlation diagrams of xenon
with the U-Xe (square), solar wind (SW, open circle),
and atmospheric (ATM, triangle) xenon compositions plotted.
Mixing lines of U-Xe with ^{244}Pu fission xenon (Pu-Xe) and
H-Xe are indicated, as are trend lines for cosmic ray
produced xenon (CR-Xe) and s-Xe. Typical one standard
deviation errors in the measurements are plotted in the
corner of each figure.

FIGURE 18.   Plot of $^{136}Xe/^{132}Xe$ versus $^{124}Xe/^{132}Xe$.

FIGURE 19.   Plot of $^{136}Xe/^{132}Xe$ versus $^{126}Xe/^{132}Xe$.

FIGURE 20.   Plot of $^{136}Xe/^{132}Xe$ versus $^{134}Xe/^{132}Xe$.

FIGURE 21.   Plot of $^{136}Xe/^{132}Xe$ versus $^{130}Xe/^{132}Xe$.

FIGURE 22.   Plot of $^{136}Xe/^{132}Xe$ versus $^{128}Xe/^{132}Xe$.

FIGURE 23.   Plot of $^{136}Xe/^{132}Xe$ versus $^{131}Xe/^{132}Xe$.

FIGURE 24.   A compilation of the xenon data and the one standard devia-
tion errors for the Braunau iron meteorite metal sample.

Figure Captions (continued)

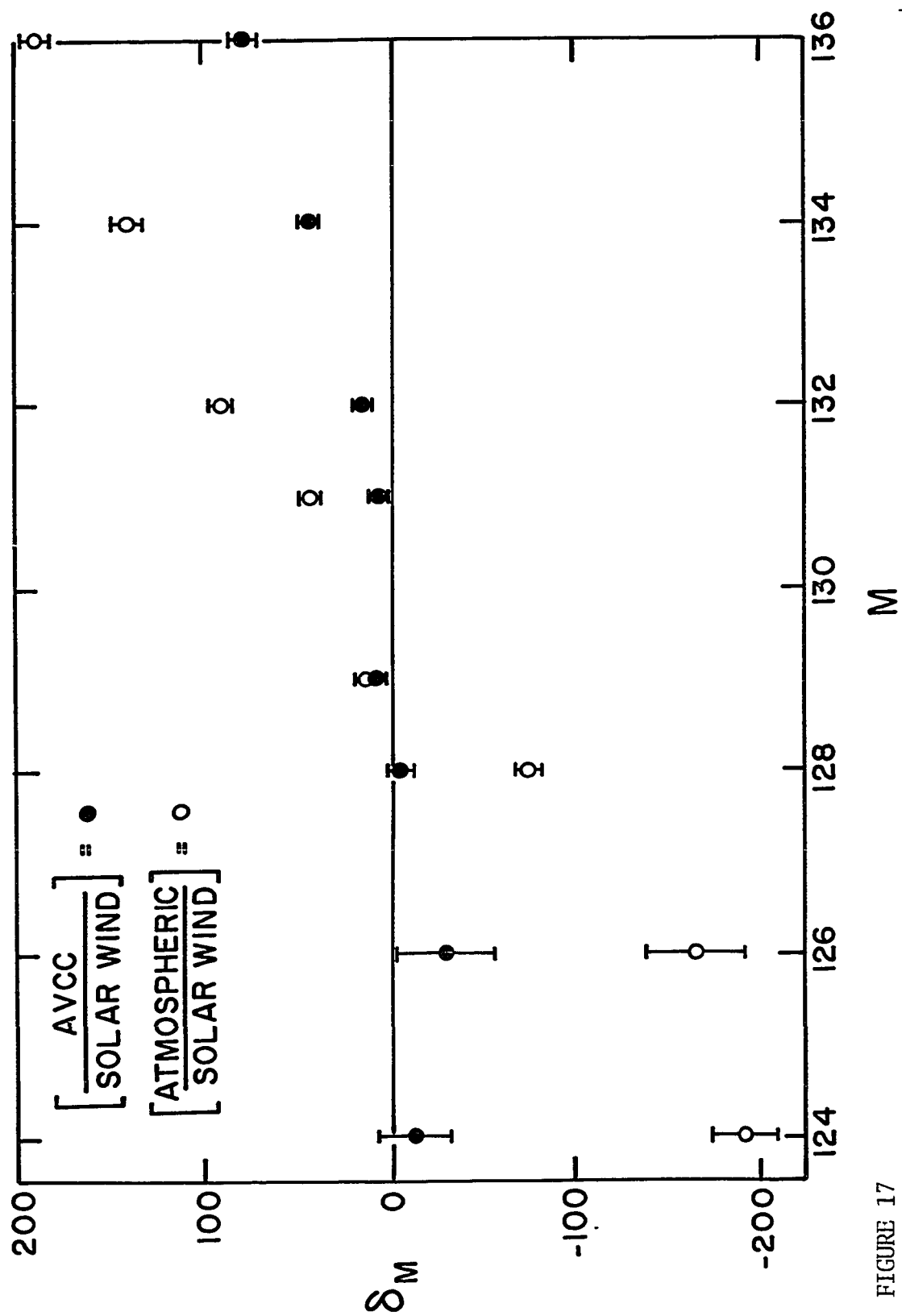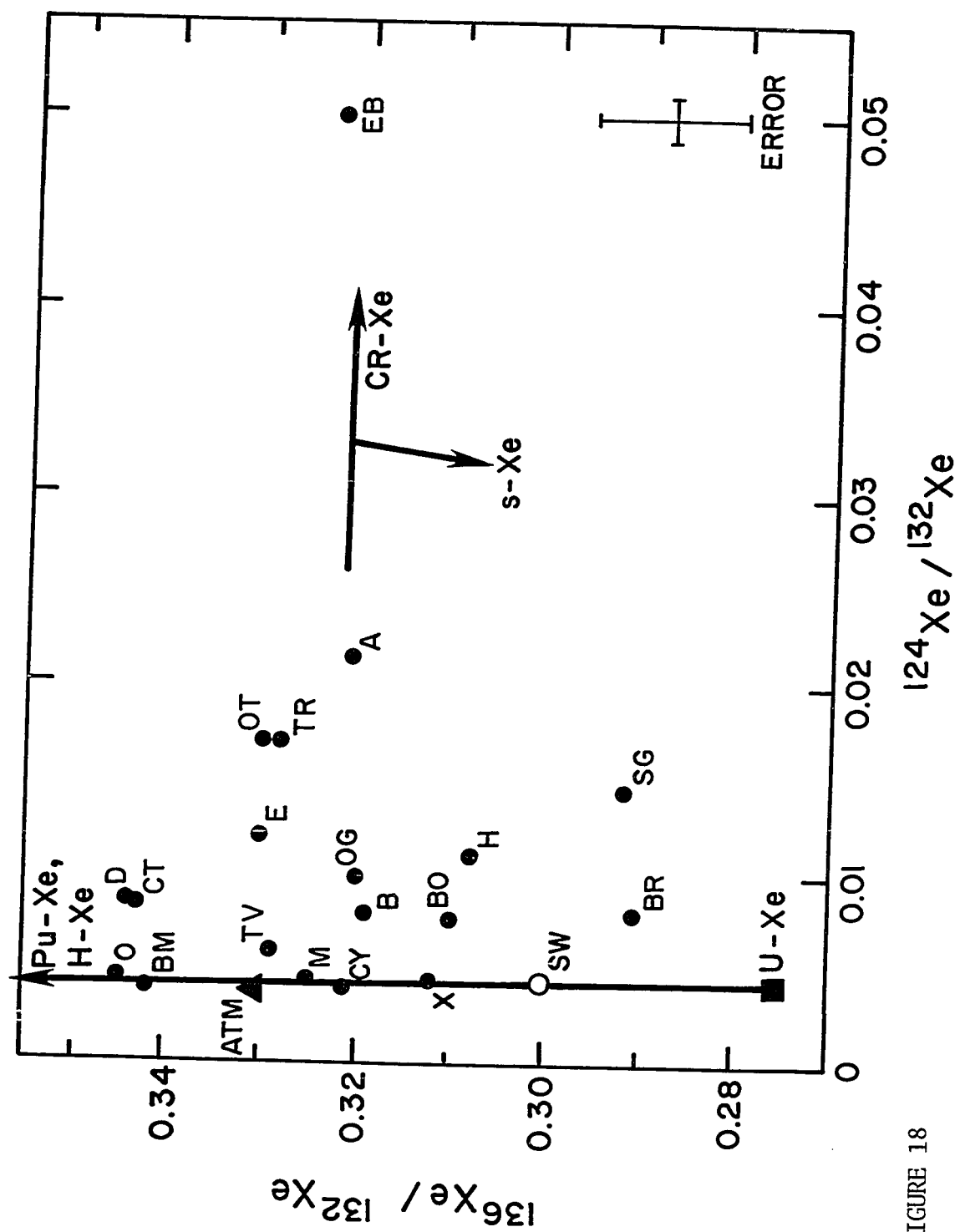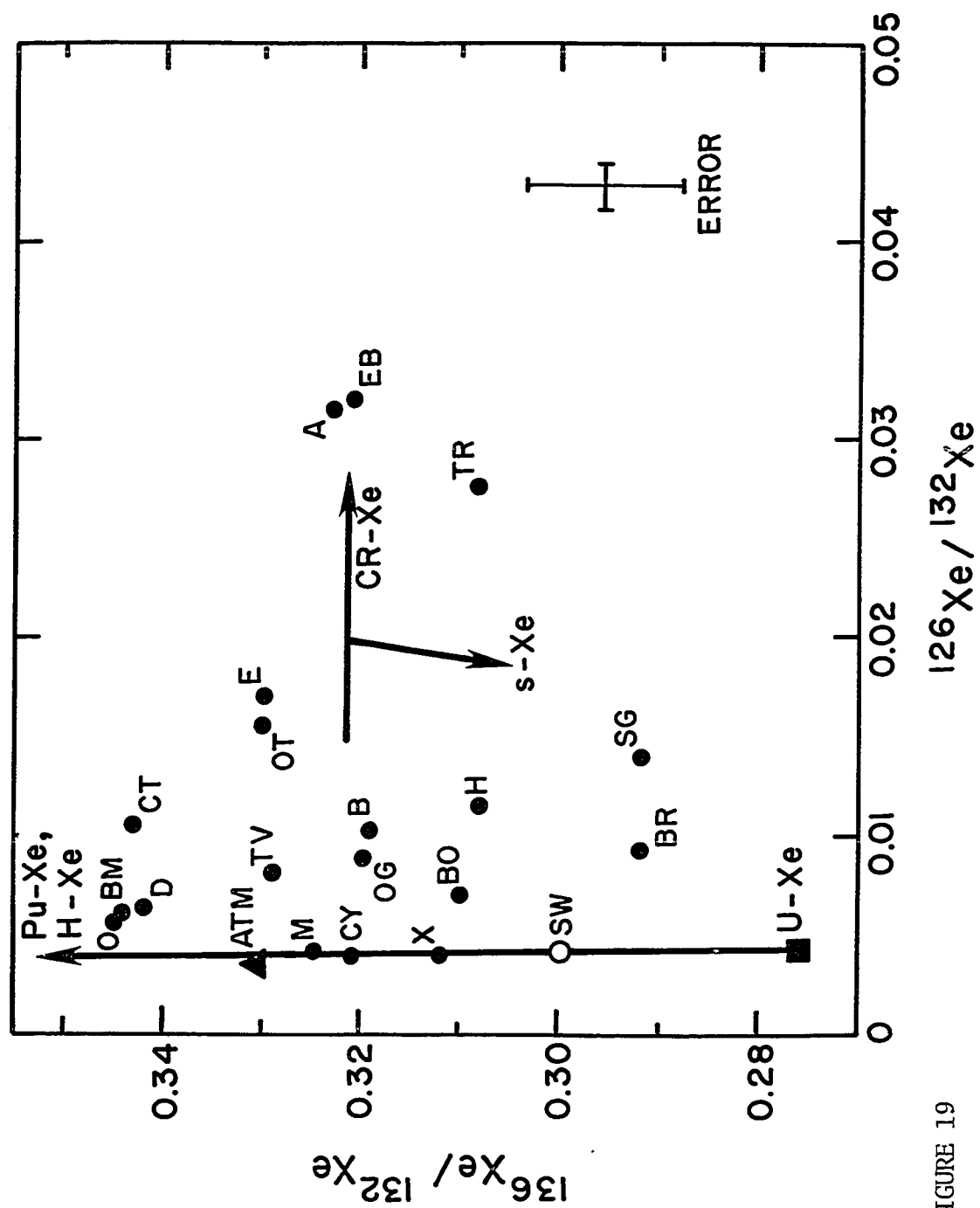Components, mixing lines, and trend lines are as in
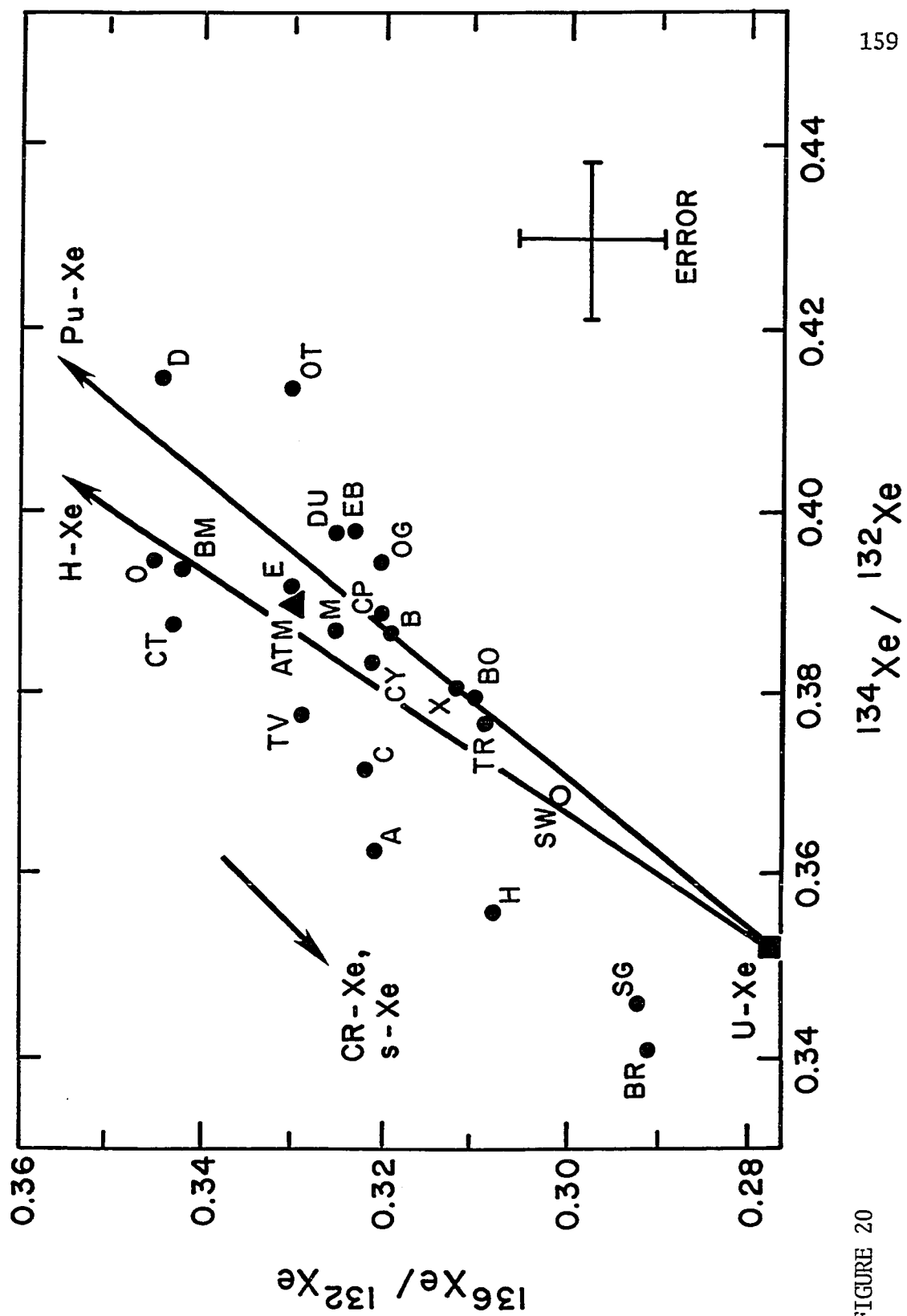
Figure 18 through 23.
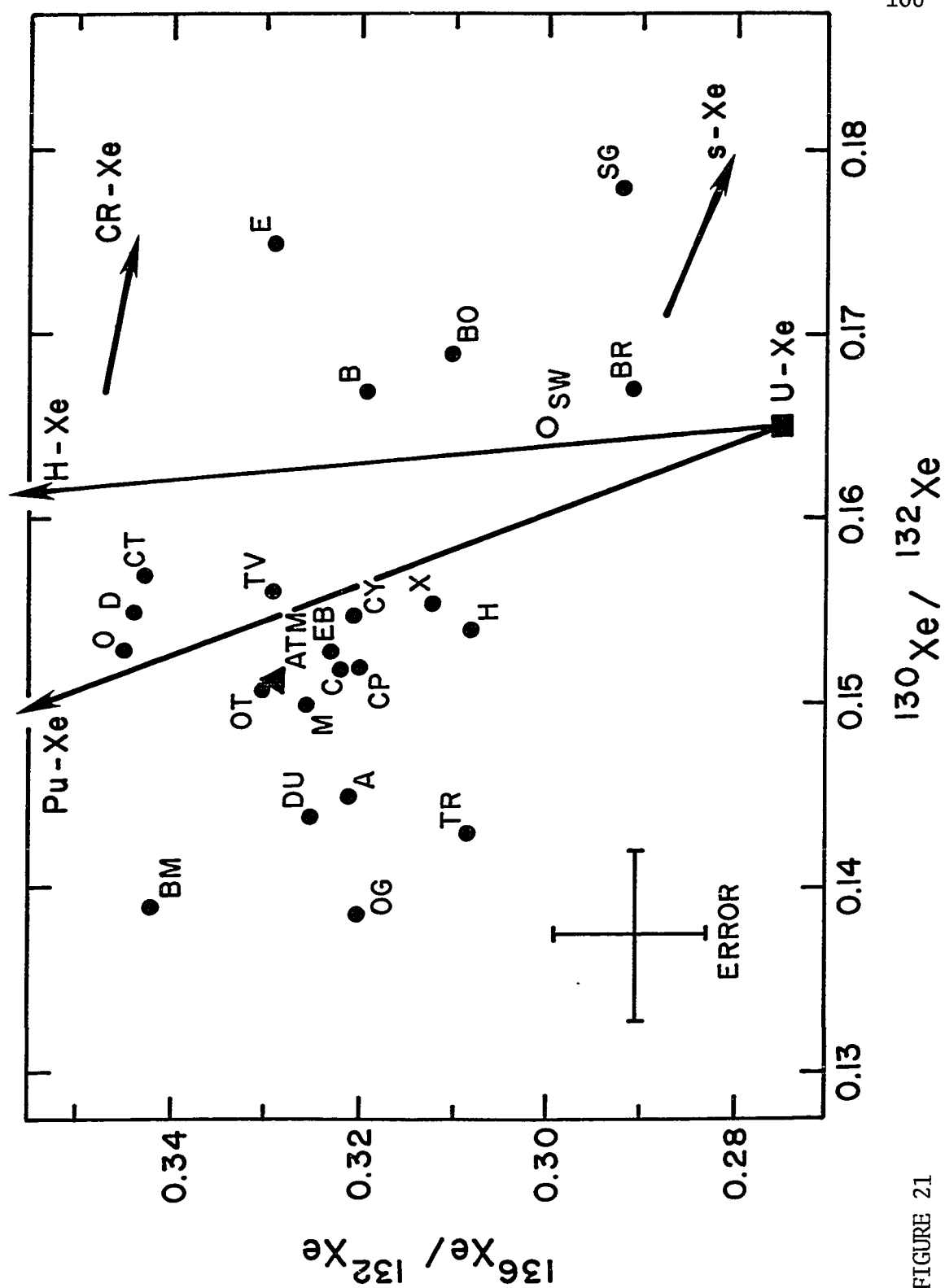
FIGURE 17

FIGURE 18
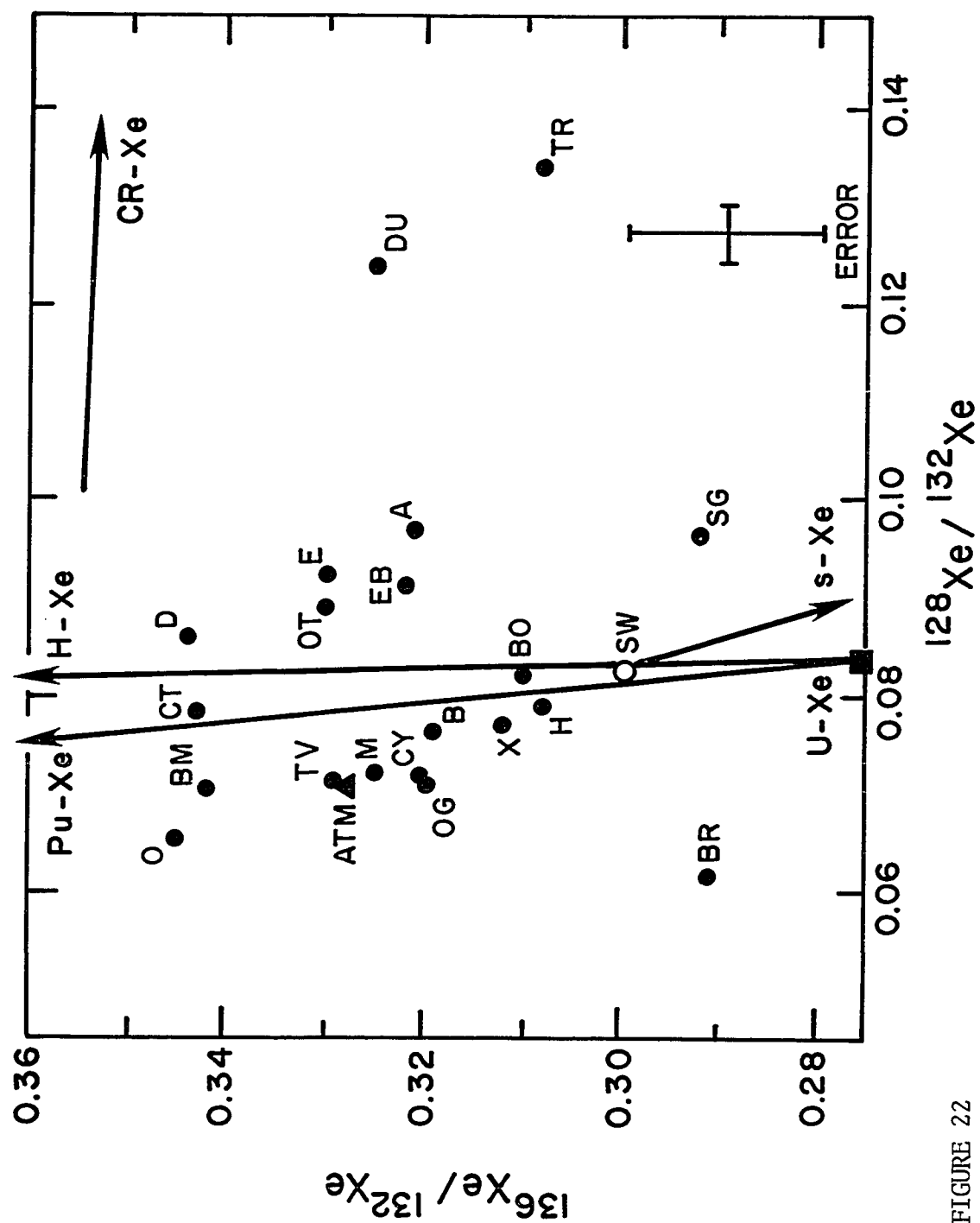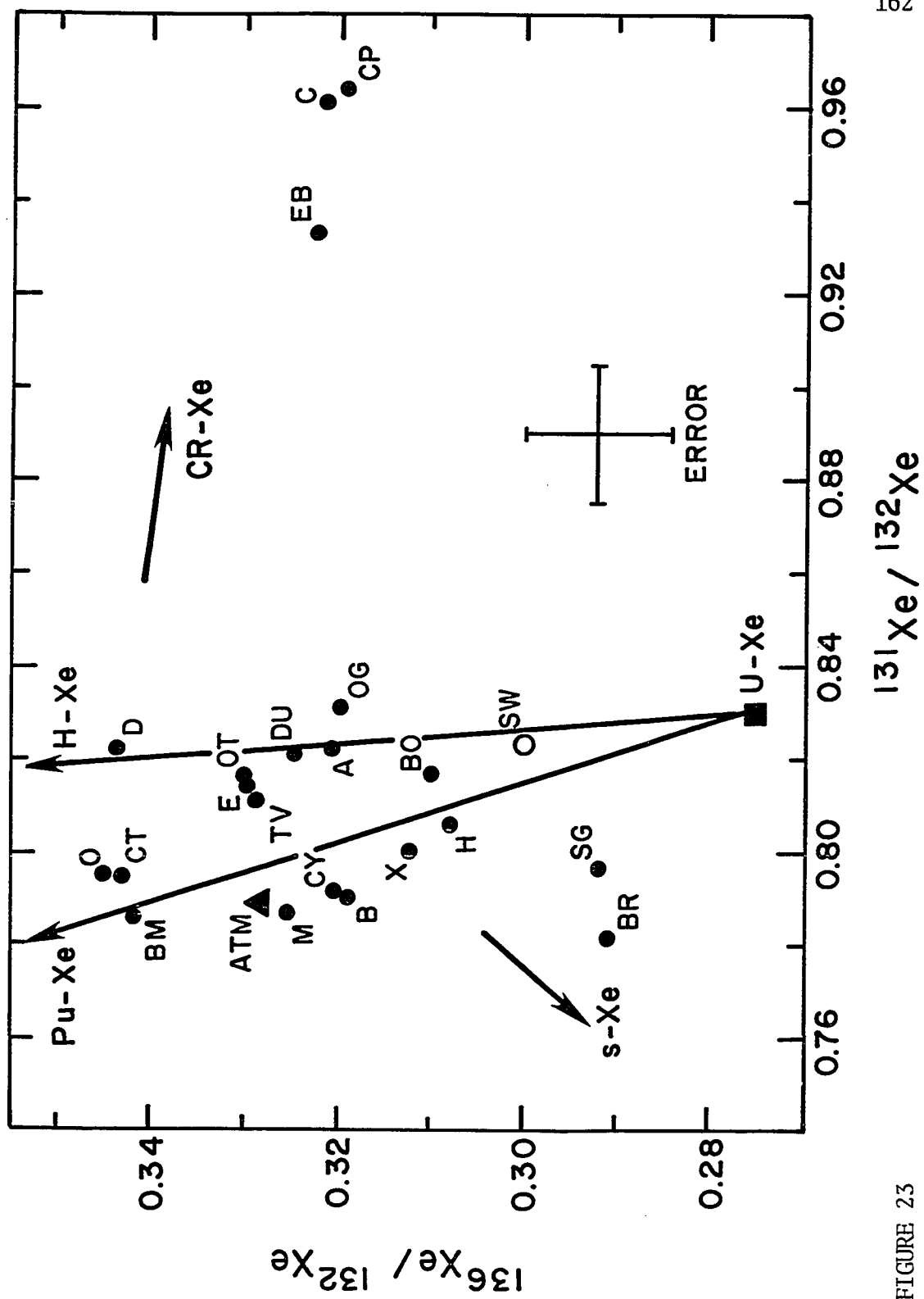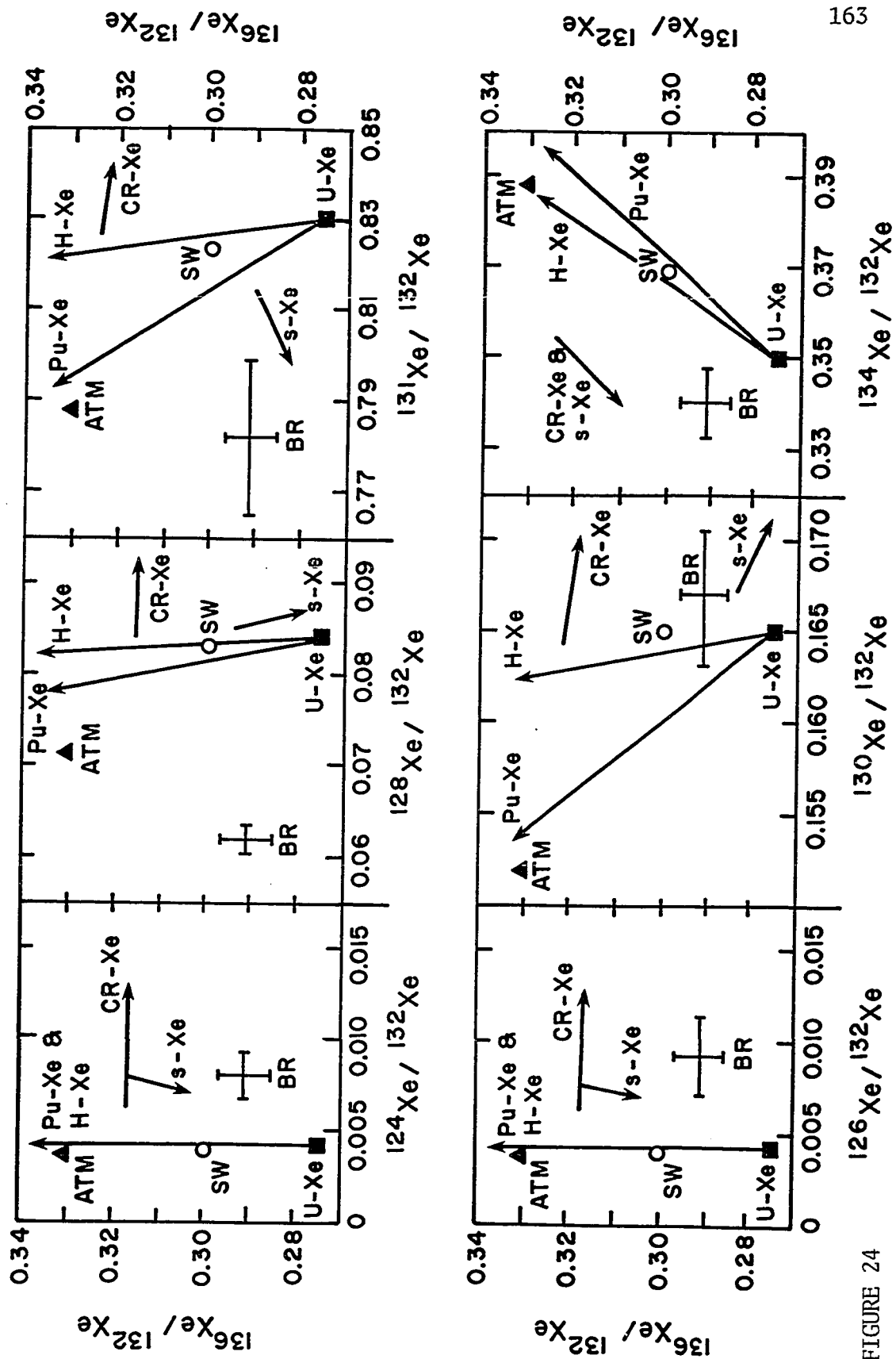
FIGURE 19

FIGURE 20

FIGURE 21

FIGURE 22

FIGURE 23

FIGURE 24

the figures, and the most extreme data plot well off these diagrams to the right. This is due to the long cosmic ray exposure ages of some of the samples, such as Costilla Peak, which Munk (1967a) reports as having a $^{126}Xe/^{132}Xe$ ratio of 0.153. Of the samples presently analyzed only Duchesne falls off Figures 18 and 19, but the errors associated with the measurement of these particular ratios in that sample were very large (see Table 3). However, most importantly, it can already be seen that it is impossible for the observed data points to be explained as the mix of a single xenon composition such as solar wind or atmospheric with spallation produced gas, because the spread of the $^{136}Xe/^{132}Xe$ ratios is much too large for that to be true.

This is truly one of the most fundamental results which has emerged from my study. All earlier investigators have assumed that xenon in iron meteorites is a mix of atmospheric and spallation xenon plus, perhaps, a little bit of an exotic "light" component at ^{124}Xe and ^{126}Xe. From what follows, it should become clear that those earlier assumptions are totally unjustified.

Since the data in Figures 18 an 19 do not define a linear correlation, at least three xenon components are required to account for the variations. The mixture of solar wind, atmospheric, and cosmogenic xenon components can produce the majority of the compositions seen in these figures. However, the most interesting meteorites are those with xenon compositions which are not consistent with such an interpretation. The Braunau and Sierra Gorda samples have $^{136}Xe/^{132}Xe$ ratios less than that

Data lying to the left of the U--H and U--Pu xenon mixing lines in Figure 20 could indicate the presence of spallogenic gas. Since spallation will produce essentially only ^{132}Xe in this figure, in general those meteorites with long cosmic ray exposure ages should trend toward the origin. The exact location of a sample will depend not only on its spallation target composition but its original primordial xenon composition. What is striking is that the two meteorites furthest from the mixing lines are Braunau and Sierra Gorda. Their short cosmic ray exposure ages rule out such a large shift in position as being due to cosmogenic gas, although the direction of the shift is consistent with that case. An admixture of s-Xe will also shift compositions in that direction on Figure 20, as s-Xe contains no ^{134}Xe or ^{136}Xe.

The isotope best suited to show confirmation of a possible s-Xe component is ^{130}Xe (Figure 21). ^{130}Xe is formed by the s-process of nucleosynthesis and by spallation, although the spallation yield is relatively small (see Table 9). Spallation could show up, but cannot displace the data points too much away from the mixing lines between non-spallogenic components. Figure 21 indicates that Sierra Gorda and Braunau continue to trend in a direction consistent with their having a s-Xe component.

Another xenon isotope produced by the s-process of nucleosynthesis is ^{128}Xe. The analysis of correlations between ^{128}Xe and the other isotopes is somewhat more difficult than for ^{130}Xe due to ^{128}Xe having a strong spallogenic production yield. This fact is reflected in

Figure 22 where a number of meteorites plot off the ^{136}Xe/^{132}Xe versus ^{128}Xe/^{132}Xe diagram to the right. The crucial observation in this figure is the separation of the Braunau and Sierra Gorda data points. In all previous figures these two meteorites always plotted together and in positions consistent with their having a s-Xe component. This follows in Figure 22 for Sierra Gorda, but distinctly not for Braunau. Therefore, the anomalous xenon composition seen in Braunau cannot be due to a s-Xe component alone.

Figure 23 completes the cycle of stable xenon isotopes by plotting ^{131}Xe/^{132}Xe along the abscissa. ^{131}Xe is an isotope whose possible origins are the most complex of those in xenon. Table 9 shows that this is the only isotope of xenon which has a non-zero value in each of the components listed. It is formed by the r-process in stellar nucleosynthesis, and Dziczkaniec (1980) has shown that it can also be made, in principle, by the p-process. The data in Figure 23 plot in locations similar to those in Figure 21 with respect to the various components and trend lines, except that in this figure the larger spallogenic component is evident in a few samples.

Some general comments can be made concerning Figures 18 through 23. First of all, a number of samples contain a mix of solar wind and atmospheric xenon components. This is most clearly seen in Figures 20 and 21, where the spallation contribution to the isotopes involved are relatively insignificant. The xenon compositions of the meteorites Arispe, Bohumiltz, Butler, Duchesne, Edmonton, El Burro, Hoba, Tawallah

Valley, and Tombigbee River may all be produced as a mixture of solar wind, atmospheric, and cosmogenic xenon components. Arispe, Duchesne, and Tombigbee River always show evidence of a significant spallation component. This result is not surprising for Arispe or Tombigbee River, both of which have long cosmic ray exposure ages and have indicated a similar component in the other inert gases. Duchesne has a large concentration of xenon, which favors a spallation origin for that gas. It is true that the exposure age reported for Duchesne is only 200 million years, but this meteorite could have suffered multiple breakups with this sample coming from an "old" portion of the meteorite parent body which has not been studied previously.

The occurence of atmospheric xenon, or what appears to be an atmospheric component, in meteorites has long been a topic of debate in this field. Obviously, one suspects that meteorites pick up atmospheric xenon during their time on earth, especially iron meteorites which are prone to rusting. However, it is by no means clear how much of the atmospheric gas is indigenous to the meteorites of my study and how much is due to contamination. Every effort was made to eliminate terrestrial contamination (see section II. D.), but it is doubtful these efforts could have been totally successful. This means that the truly indigenous gas compositions are actually always at locations which are further from the atmospheric point than they show on the figures.

The ^{129}Xe data are not discussed with the other xenon isotopes because of the known possibility of a ^{129}I decay contribution. Many of

the meteorites analyzed show evidence of such a component (see Table 6).

The El Burro sample has the largest $^{129}Xe/^{132}Xe$ value of the 15 samples

investigated, and it is similar in magnitude to the enrichment seen in

the metal phase of Carbo by Munk (1967b). The Tawallah Valley and

Tombigbee River samples are unusual in having anomalously low $^{129}Xe/^{132}Xe$

ratios. Since the Tombigbee River sample has shown strong indications

of a large spallation component, this deviation is especially unusual in

that ^{129}Xe is much more abundantly produced by spallation than is ^{132}Xe.

The addition of a large heavy isotope rich xenon component seems neces-

sary for these two meteorites to have such an apparent ^{129}Xe underabun-

dance.

To summarize the new and most significant results which emerge

from an analysis of the three isotope correlation diagrams of xenon:

1) Trapped xenon gas in iron meteorites is not solely of atmospheric

composition. There is strong evidence from the data of possible trapped

xenon components similar to U-Xe, s-Xe, the solar wind, ^{244}Pu and/or

H-Xe, as well as atmospheric.

2) There are earlier results which suggest that iron meteorite metal

samples contaminated with troilite (FeS) and/or silicate inclusions con-

tain fission xenon. The presence of heavy isotope rich xenon is confirm-

ed here in every figure for Babb's Mill, Cedartown, Dayton, and Odessa,

but it is not clear whether the xenon from these meteorites originated

from imbedded inclusions.

3) There is the strong indication that iron meteorites may contain

a s-Xe component . Sierra Gorda's xenon composition, while being very anomalous, is extremely consistant in that it always trends in the direction of a s-Xe like component mixed with solar wind xenon and a small cosmogenic component. This is a remarkable result--to see a component in a bulk iron meteorite sample which had previously only been detected in the carbon-rich residue of a carbonaceous chondrite (Srinivasan and Anders, 1978).

4) The Braunau meteorite is abnormal in that it contains a xenon component not previously seen in any meteorite sample, stony or iron. The composition is most anomalous at ^{128}Xe, and shows that the data from this meteorite cannot arise solely from the addition of a s-Xe component. The ^{128}Xe/^{132}Xe ratio in Braunau equals 0.0618, whereas the s-process prediction is 0.133 (Lamb et al., 1977), and the s-Xe ratio deduced by Srinivasan and Anders (1978) is 0.211.

In an effort to better understand the Braunau anomalies, the various xenon components and trend lines from Figures 18 through 23 are replotted with only Braunau's data and error bars in Figure 24. From this figure one sees that an enrichment of ^{130}Xe and ^{132}Xe and a depletion of ^{128}Xe, ^{129}Xe, and ^{131}Xe will qualitatively produce the unusual results seen. This suggests that neutron capture might be the source of these anomalies, since the odd N isotopes of this even Z element have greater neutron capture cross sections, in general.

To investigate this possibility at least semi-quantitatively, the following simplified calculations were carried out. Assuming that

the initial $^{131}Xe/^{132}Xe$ ratio in Braunau had the solar wind value of 0.823, and that the change in the ratio to its present value of 0.782 is due solely to neutron capture on ^{131}Xe, the required neutron flux may be estimated:

$$\Delta^{131}Xe(cm^3STP/g) = (neutron\ flux)(^{131}Xe_0)\sigma_{131}(t) \qquad IV.\ (12)$$

The change in the ^{131}Xe concentration is represented by $\Delta^{131}Xe$; the neutron flux is in neutrons/cm^2; $^{131}Xe_0$ is the initial, pre-irradiation concentration of ^{131}Xe in Braunau in cm^3STP/g; σ_{131} is the neutron capture cross section of ^{131}Xe in cm^2; and t is the neutron irradiation interval, assumed to be equal to the average cosmic ray exposure age of Braunau ($1.9 \times 10^{14}s$).

The resulting flux necessary for this conversion of ^{131}Xe to ^{132}Xe is 1.6×10^6 neutrons/cm^2s for the thermal neutron capture cross section of 90 barns, and 1.7×10^5 neutrons/cm^2s for the resonant integral neutron capture cross section of 870 barns. Both of these fluxes are well above that expected to result from spallation reactions (approximately 5 to 20 neutrons/cm^2s; Clarke and Thode, 1964), but as noted earlier, 10^{20-21} neutrons/cm^2 is consistent with theoretical predictions in supernovae. Since the ^{132}Xe resonant integral for neutron capture is only 4.5 barns, neutron capture on ^{132}Xe can be safely ignored.

The same calculation must also be carried out for the enrichment of ^{130}Xe by neutron capture on ^{129}Xe, and for the depletion of ^{128}Xe, to determine if the derived neutron irradiation flux required to

produce the observed anomalies remains constant. For ^{129}Xe there is the problem in knowing what the initial ^{129}Xe/^{132}Xe ratio might have been because of the possibility of ^{129}I decay contributions to the present ^{129}Xe concentration. For this estimate, the initial ^{129}Xe concentration was assumed to be equal to the initial ^{132}Xe concentration derived in the above calculation. The flux necessary to convert that initial ^{129}Xe concentration to that seen presently in Braunau was 1.5 x 10^6 neutrons/ cm^{2}s for the thermal neutron capture cross section of 20 barns, and 1.2 x 10^5 neutrons/cm^{2}s for the resonant integral neutron capture cross section of 250 barns. This is only a lower estimate of the flux required, because unlike the previous case, the nuclei being produced, ^{130}Xe, does not have negligible neutron capture cross sections relative to the nuclei on which the neutron capture is taking place. The thermal neutron capture cross section of ^{130}Xe is 5.4 barns and the resonant integral cross section is 115 barns.

Within the obvious limitations of this admittedly first-order estimate, the neutron fluxes required in the above calculations are consistent, although high. In both cases the depletion produced in the nuclei capturing neutrons was approximately 3%.

The most dramatic anomaly in Braunau, however, is at the isotope ^{128}Xe. Even though the resonant integral for neutron capture on ^{128}Xe is 330 barns versus the thermal capture cross section of 4.4 barns, the average high energy neutron flux of about 1.5 x 10^5 neutrons/cm^{2}s calculated above is insufficient to produce the change in the ^{128}Xe/^{132}Xe ratio

from that of the solar wind (0.0831) to the measured value of 0.0618. A minimum flux of 3.9 x 10^6 neutrons/cm^{2}s is necessary to produce the 24% depletion of the initial ^{128}Xe concentration this mechanism suggests.

The drastic depletion of ^{128}Xe required to alter the solar wind ^{128}Xe/^{132}Xe ratio and the inconsistency between the derived neutron fluxes needed to produce the different xenon isotopic enrichments makes it very doubtful that neutron capture on a xenon composition similar to that of the solar wind is responsible for the presently measured xenon composition in Braunau. However, because of the qualitative agreement between the observed anomalies and the depletions one would predict from the neutron capture cross sections, this line of reasoning seems worth pursuing further.

One possibility is that the assumed solar wind composition as the initial trapped Braunau composition is incorrect. The atmospheric ^{128}Xe/^{132}Xe ratio equals 0.0714, so the ^{128}Xe depletion required by assuming an initial xenon composition of atmospheric xenon is less than that calculated above. Nevertheless, the depletion necessary is more than 12%. Furthermore, the fluxes deduced for the enrichment of ^{130}Xe and ^{132}Xe differ by more than an order of magnitude. Thus neutron irradiation of an atmospheric xenon composition also shows poor agreement with the observed Braunau xenon isotopic ratios.

One initial xenon composition which could possibly produce the Braunau data is the s-xenon seed composition assumed by Dziczkaniec (1980) in her investigation of nuclear processes in massive stars:

$$^{128}Xe: \ ^{129}Xe: \ ^{130}Xe: \ ^{131}Xe: \ ^{132}Xe \ =$$

$$0.1330: \ 0.0533: \ 0.3920: \ 0.1500: \ \equiv 1.000$$

Since ^{128}Xe is the only nucleus which is only destroyed and not formed during the neutron irradiation, its concentration relative to ^{132}Xe can only decrease. Also, the initial ^{129}Xe and ^{131}Xe abundances relative to ^{132}Xe are so much lower than in solar wind or atmospheric compositions that their contribution to the ^{130}Xe and ^{132}Xe concentrations, respectively, will be small shortly after the start of the irradiation. This permits the loss of ^{128}Xe to continue for a longer interval before producing significant enrichments at ^{130}Xe and ^{132}Xe.

Unfortunately, this qualitative discussion is all that can be offered at this time. Dziczkaniec (1980) did not investigate low enough neutron fluxes to be able to test this hypothesis at present. It is hoped that future analysis in this area will yield a simultaneous solution for all the xenon isotopes which matches that seen in Braunau.

In any _in_ _situ_ neutron irradiation of Braunau there is a problem with the light isotopes ^{124}Xe and ^{126}Xe. The ^{124}Xe resonant integral for neutron capture is extremely large (3000 barns), so if neutron irradiation were the mechanism for altering the $^{128}Xe/^{132}Xe$, $^{130}Xe/^{132}Xe$ and $^{131}Xe/^{132}Xe$ ratios _in_ _the_ _meteorite_, the $^{124}Xe/^{126}Xe$ ratio should be anomalously low. Since it is not, if a strong neutron irradiation is the reason for the anomalies seen in Braunau, the irradiation must have taken place sometime prior to the time the xenon was trapped in the meteorite. The puzzling corollary is that the loss of ^{124}Xe must have been made up

by the addition of a ^{124}Xe rich gas prior to trapping the mixture in the meteorite parent body.

E. Mineral Separates from Odessa

1) Introduction

There have been more precursor studies of the heavy inert gases from inclusions in iron meteorites than from the metal phase itself. This is because the concentrations of krypton and xenon are considerably greater in such samples, hence the greater likelihood of finding anomalous, and therefore interesting, compositions. Also, the experimental obstacles in the study of inclusions are not so difficult to overcome. Still, the number of these reports on krypton and xenon is not large, but investigations of inclusions restricted to the light inert gases, helium, neon, and argon, are quite numerous. Except for analyses of troilite and/or graphite from the Odessa meteorite, these latter reports will be disregarded here.

By far the most common published result for such investigations of krypton and xenon is that of a distinct ^{129}Xe excess. This excess has been seen in troilite inclusions from iron meteorites (Reynolds et al., 1962; Alexander et al., 1968), in graphite (Alexander and Manuel, 1967; Alexander and Manuel, 1968), and in silicate (Alexander and Manuel, 1968; Hintenberger et al., 1969; Bogard et al., 1971). This excess was in general attributed to the decay of ^{129}I, but some investigators felt that a portion of the excess ^{129}Xe could be trapped (Bogard et al., 1971).

These same references report varying concentrations of trapped krypton and xenon, but only in the silicate inclusions was this trapped

composition distinct from that of atmospheric gas. The xenon measurements from silicate inclusions of Xiquipilco (Alexander and Manuel, 1968) and Pine River (Bogard et al., 1971) required the presence of average carbonaceous chondrite (AVCC) xenon to account for the data.

Another often seen effect are excesses at ^{80}Kr, ^{82}Kr, ^{83}Kr, ^{128}Xe, and ^{131}Xe, presumably due to neutron capture reactions on bromine, selenium, iodine, and tellurium. This has been observed in troilite (Clarke and Thode, 1964; Alexander et al., 1968), graphite (Alexander and Manuel, 1967 and 1968), and silicate inclusions (Bogard et al., 1971) of iron meteorites.

The interpretation of the data for the light inert gases from iron meteorite inclusions is complicated by the presence of cosmogenic gas. Relatively small amounts of spallation krypton and xenon are found in the non-metallic phases of these meteorites, so that applying corrections for this component does not introduce a great deal of error in the deduced trapped components.

In only one previous instance have all five inert gases been measured by one investigator in the metal, graphite, and troilite phases of an iron meteorite. The Deelfontein meteorite studied by Fireman and DeFelice (1968) is a coarse octahedrite which they determined had a cosmic ray exposure age of 400 ± 40 million years. The Odessa meteorite analyzed for these same three phases in my work is also a coarse octahedrite, and its average cosmic ray exposure age is about 500 million years (see Table 3). Thus these two meteorites should provide an

interesting comparison.

Begemann (1965) has measure the helium and neon isotopes from two different troilite samples taken from Odessa inclusions. The resulting average isotopic ratios reproduced below may be compared to those in Tables 3 and 7:

^{3}He	$\dfrac{^4\text{He}}{^3\text{He}}$	^{20}Ne	$\dfrac{^4\text{He}}{^{20}\text{Ne}}$	$\dfrac{^{20}\text{Ne}}{^{22}\text{Ne}}$	$\dfrac{^{21}\text{Ne}}{^{22}\text{Ne}}$
4.6×10^{-7}	6.67	2.99×10^{-8}	102	0.896	0.870

The ^{3}He and ^{20}Ne concentrations are in cm^3STP/g.

2) Metal and Troilite

Of the mineral separates analyzed, only the sample labeled as troilite in Table 3 will be discussed here. The discarding of the non-magnetic "troilite" aliquot was justified earlier due to the very nature of its name--presumably troilite (FeS) should be magnetic. This sample was that left after a purifying magnetic separation and was run on the chance that it might produce useful results.

An examination of the helium, neon, and argon data from the three phases of Deelfontein and Odessa show remarkably similar trends. As was discussed in section IV. B., the results for these gases from the metal phase of Odessa may be interpreted almost entirely as spallation products, and this is also true for Deelfontein.

The troilite phase analyzed in my work and those analyzed by Fireman and DeFelice (1968) and Begemann (1965), also show definite

evidence of a strong spallogenic component. Relative to the metal phase, the ^{4}He/^{3}He and ^{36}Ar/^{38}Ar ratios increase and the ^{21}Ne/^{22}Ne ratio decreases in the troilite of both Odessa and Deelfontein. This would be consistent with the admixture of a small amount of atmospheric gas, except that in both meteorites the ^{20}Ne/^{22}Ne ratio in the troilite de-creases relative to the metal phase, which is the opposite of what such an interpretation would predict.

This is a striking result which suggests the presence of a neon component similar to that of Ne-E (pure ^{22}Ne) in iron meteorite inclusions. The possibility of Ne-E making a significant contribution to the neon in iron meteorites was discussed with respect to the metal phase sample of Cedartown and Figure 11 in section IV. B. Why this component would be preferentially located in the troilite phase is not clear.

The low concentration of argon in the metal phase of Odessa shows up again in the fact that ^{20}Ne/^{36}Ar in the metal is greater than ^{20}Ne/^{36}Ar in the troilite. The normal, but reverse behavior is seen in Deelfontein. In troilite, both iron and sulfur contribute to the production of cosmogenic neon, and since sulfur is closer in mass to neon than is iron, the production of neon in troilite should be favored over that in the metal phase.

Assuming the troilite to be pure FeS, then the difference in the ^{21}Ne/^{38}Ar ratios in the metal (assumed all iron) and the troilite phases can be used to calculate the relative cross sections of sulfur and iron for the production of ^{21}Ne, $\sigma_S^{21}/\sigma_{Fe}^{21}$. The ^{21}Ne and ^{38}Ar isotopes are

chosen for this calculation because in neon and argon cosmogenic components show up most prominently in these two isotopes. Since ^{38}Ar cannot be made by spallation from sulfur:

$$\left.\frac{^{21}Ne}{^{38}Ar}\right)_{troilite} = \frac{(\sigma_S{}^{21} + \sigma_{Fe}{}^{21})}{\sigma_{Fe}{}^{38}}$$

or

$$\frac{\sigma_S{}^{21}}{\sigma_{Fe}{}^{21}} = \frac{\sigma_{Fe}{}^{38}}{\sigma_{Fe}{}^{21}} \left.\left(\frac{^{21}Ne}{^{38}Ar}\right)\right)_{troilite} - 1 \qquad\qquad IV. \ (13)$$

The ratio is 0.93 when this is done for Odessa, while using the data from Deelfontein give 4.02. Since cosmic rays on sulfur in troilite should be approximately 17 times more effective in producing ^{21}Ne than cosmic rays on iron (Mazor et al., 1970), the underabundance of argon in the Odessa metal sample continues to be puzzling.

The absolute amounts of krypton and xenon were only known within about 50% accuracy for the Deelfontein samples due to blank values and the procedures used by Fireman and DeFelice (1968). Thus their heavy inert gas isotopic ratios have much larger standard deviations than those for the present analyses of Odessa.

The krypton concentrations in the mineral separates of Odessa are more than two orders of magnitude greater than in the metal phase, and the troilite phase shows very strong enrichments at the light krypton isotopes ^{78}Kr and ^{80}Kr. The troilite data are very similar in Odessa and

Deelfontein except at ^{83}Kr/^{84}Kr. Troilite appears to be the host mineral for selenium in meteorites (Pelly and Lipschutz, 1971), and the large excess in Deelfontein at ^{83}Kr was attributed to neutron capture on ^{83}Se by Fireman and DeFelice (1968).

The ^{83}Kr/^{84}Kr ratio in the Odessa troilite is much smaller than that measured in Deelfontein. Assuming the ^{83}Kr/^{84}Kr ratio in the troilite phase of Odessa was originally the solar wind-atmospheric value of 0.202, the concentration of selenium necessary for neutron capture on ^{82}Se to produce the presently measured ratio of ^{83}Kr/^{84}Kr = 0.231 can be calculated. If the ^{84}Kr abundance is the same as it was initially, the flux of neutrons is taken as that expected from secondary spallation reactions of approximately 5 neutrons/cm^{2}s and the irradiation interval equals the average cosmic ray exposure age of Odessa, then the selenium concentration required for neutron capture on ^{82}Se to produce the excess ^{83}Kr seen is 270 parts per million. This concentration fits into the range of values reported by Pelly and Lipschutz (1971) for the troilite phase of iron meteorites (130-300 ppm).

Assuming the ^{82}Kr/^{84}Kr ratio in the Odessa troilite initially equaled the solar wind-armospheric value of 0.202, the bromine concentration necessary in that phase to produce the excess ^{82}Kr from neutron capture on ^{81}Br may be deduced by a similar calculation. With the same assumptions as above, the bromine concentration required is 0.48 parts per million. As noted earlier in section IV. C., the bromine abundance in the metal phase of iron meteorites was estimated as being on the order

of 0.1 ppm (Reed, 1971). Its abundance in a troilite inclusion of an iron meteorite has never been measured, but in contrast to selenium, it is thought to be in minor, inhomogeneously distributed phases of meteorites (Dodd, 1969). Thus the smaller concentration of bromine than selenium and the consequent smaller enrichment of ^{82}Kr relative to ^{83}Kr is understandable.

Using this derived bromine abundance of 0.48 parts per million, the amount by which ^{80}Kr will be enriched by neutron capture on ^{79}Br may be predicted. Assuming the initial $^{80}Kr/^{84}Kr$ value equaled the solar wind-atmospheric ratio of 0.0396 and the conditions above, the predicted present $^{80}Kr/^{84}Kr$ value is 0.102. Within the errors of the calculation, this is in good agreement with the measured ratio of 0.106 ± 0.004.

The ^{78}Kr results from Deelfontein were discarded by Fireman and DeFelice (1968) because they felt contamination from handling was strongly evident in their data. In Odessa $^{78}Kr/^{84}Kr = 1.19$, which is extraordinarily large. The enrichments in ^{78}Kr and ^{80}Kr in the metal phase of a number of meteorites were noted in section IV. C. The excess in ^{78}Kr seen here is unlikely to be from the same source because it is not correlated with a like excess in ^{80}Kr. Ignoring the possibility of contributions to ^{80}Kr from neutron capture on ^{79}Br, the excess ^{78}Kr seen in the troilite of Odessa is about 56 times that seen in the metal phase whereas the excess ^{80}Kr seen in troilite is only about 3.2 times that seen in the metal phase. If there is a contribution to ^{80}Kr from neutron capture on ^{79}Br in the troilite, the disparity in the excesses would be even greater.

Thus, my conclusion is that the ^{78}Kr data from the troilite of Odessa has a large hydrocarbon component.

The xenon in the metal phases of Odessa and Deelfontein differ at every mass except ^{129}Xe. Despite the uncertainties in their measurements, Fireman and DeFelice (1968) see large excesses in the metal phase at ^{124}Xe, ^{126}Xe, ^{128}Xe, and ^{131}Xe, which they attribute to a large spallation component. Since these two meteorites have similar cosmic ray exposure ages, either the Odessa sample has distinctly different heavy trace elements as spallation targets, or it originated from a more well shielded location within its parent meteoroid. The pronounced heavy isotope enrichment at ^{134}Xe and ^{136}Xe in Odessa discussed earlier is absent from Deelfontein.

The xenon composition in the troilite phase of Odessa is the most anomalous of the three phases analyzed relative to the solar wind composition. The light isotopes ^{124}Xe, ^{126}Xe, and ^{128}Xe contain a spallogenic component in the troilite, with ^{124}Xe/^{132}Xe, ^{126}Xe/^{132}Xe, and ^{128}Xe/^{132}Xe values significantly greater than in the other phases. Also striking in the troilite is the high ^{134}Xe/^{132}Xe ratio, which does not have the correspondingly high ^{136}Xe/^{132}Xe ratio expected from the admixture of a heavy xenon isotope rich component such as ^{244}Pu fission xenon or H-Xe. It is not clear how such a large excess at ^{134}Xe could be produced without affecting ^{136}Xe by an even greater amount.

One possibility is the reaction ^{133}Cs$(n,\gamma)^{134}$Cs$(\beta^+)^{134}$Xe, since the resonant integral for neutron capture on ^{133}Cs (the only stable

cesium isotope) is a relatively large 421 barns. Unfortunately, no determinations of the concentration of this element have been made in any iron meteorite or iron meteorite inclusion, so whether there could be sufficient cesium in the troilite phase to produce such an excess at ^{134}Xe is speculative.

The troilite from Deelfontein is extremely anomalous at ^{129}Xe and ^{131}Xe. The ^{129}Xe/^{132}Xe ratio of 3.45 is one of the largest observed in meteorites. The excess ^{129}Xe can arise from extinct ^{129}I or from neutron capture on ^{128}Te since both iodine and tellurium are concentrated in troilite (Goles and Anders, 1962). Since the excess ^{129}Xe is 5 times larger than the excess ^{131}Xe despite the ^{128}Te and ^{130}Te abundances and neutron capture cross sections being approximately equal, Fireman and DeFelice (1968) conclude that at least four-fifths of the ^{129}Xe excess must be due to ^{129}I decay. The ^{129}Xe excess is also largest in the Odessa troilite phase , and surprisingly, the excess is also 5 times larger than the excess ^{131}Xe, so one may arrive at the same conclusions as to their source as in Deelfontein.

3) Graphite

The data from the mineral separate labeled as "graphite from sawings" in Table 3 are questionable for the following reason. The graphite recovered by acid treatment of the Odessa sawings was an extremely fine powder. Some of the data from this sample agree well with the graphite sample mined directly from the inclusions, but there are

distinct indications that the large surface area of this powder absorbed a significant amount of atmospheric gas during its handling. Due to this admixed component, this sample will not be considered further.

In the graphite phase of Odessa the concentration of ^{3}He is approximately the same as in the metal and about one-fourth of that seen in the troilite. Assuming the graphite separate to be pure carbon and the helium to be entirely cosmogenic in origin, the ^{4}He/^{3}He ratio of 8.07 indicates that spallation on carbon will produce ^{4}He approximately 2.2 times more frequently than ^{3}He, relative to "boiled off" helium resulting from spallation reactions on iron and nickel in the metal phase where ^{4}He/^{3}He = 3.60.

However, the neon data from the graphite separate suggest that there is a trapped light inert gas component as well as a spallogenic one. Spallation neon and argon cannot arise from the carbon in graphite, so any cosmogenic component for these two gases must be the result of nickel-iron and/or trace minerals embedded in the graphite or gas implanted by recoil from the surrounding phases. The graphite was washed in acid to remove any of these other phases attached to the outside of the excavated graphite chunks, but obviously some impurities were located within these chunks.

The ^{20}Ne/^{22}Ne and ^{22}Ne/^{21}Ne ratios are substantially larger in the graphite than in the troilite or metal phases in both Odessa and Deelfontein, which could be due to either atmospheric contamination or an indigenous component. Figure 11 shows that the neon composition in

Odessa graphite plots exactly on the solar wind--spallogenic neon mixing line, so a two component mix of trapped primordial solar wind neon and spallogenic neon is the most reasonable interpretation of the data. A two component mix of 16% solar wind neon and 84% cosmogenic neon yields the neon composition measured in the Odessa graphite.

If the helium data are altered by assuming 16% of the helium is due as well to a trapped primordial solar wind component, the resulting cosmogenic $^4He/^3He$ carbon production ratio is 6.78. This is a lower limit since the graphite separate is obviously not pure carbon if 84% of the neon is due to spallation.

By examining the argon data it is possible to obtain further information on this non-spallogenic component. The high $^{36}Ar/^{38}Ar$ ratio of 3.98 in Odessa graphite strongly indicates an indigenous inert gas component in this phase, since the cosmogenic $^{36}Ar/^{38}Ar$ ratio equals 0.64. It is not as clear as in neon what argon component (or components) should be mixed with spallogenic gas to give the observed argon composition, especially since both the solar wind and atmospheric $^{36}Ar/^{38}Ar$ ratios are about 5.3. However, on the assumption that all the ^{40}Ar in Odessa is the result of atmospheric contamination ($^{40}Ar \cong 0$ in the solar wind), the corrected $^{36}Ar/^{38}Ar$ ratio is 2.05. If this ratio is the result of a two component mix of solar wind and spallogenic argon, the derived compositional mix is 30% solar wind and 70% spallogenic argon.

The inconsistency between the percentage of primordial inert gas derived from the neon and argon data could be resolved by the presence of

minerals in the graphite which favor the spallogenic production of neon over argon. One mineral which would accomplish this, and which is almost certainly embedded in the graphite, is troilite. As noted in the discussion of the troilite separate, cosmic rays on sulfur are approximately 17 times more effective in producing neon than cosmic rays on iron, and since the graphite and troilite inclusions were adjacent in Odessa, it is likely troilite impurities will be present in the graphite phase.

If one assumes that the percentages of spallogenic neon and argon deduced above are correct for those gases, the amounts of cosmogenic ^{21}Ne and ^{38}Ar can be calculated:

$$^{21}Ne_c(\text{graphite}) = 1.30 \times 10^{-8} \text{ cm}^3\text{STP/g}$$

$$^{38}Ar_c(\text{graphite}) = 1.06 \times 10^{-8} \text{ cm}^3\text{STP/g}.$$

These abundances make it possible to derive the weight percentages of iron, nickel, and sulfur in the graphite mineral separate, assuming these are the only elements present other than carbon.

The production ratios of cosmogenic ^{21}Ne and ^{38}Ar are given by Mazor et al. (1970):

$$^{21}Ne_c = 2.2(\text{Mg}) + 1.35(\text{Al}) + \text{Si} + 0.29(\text{S}) + 0.17(\text{Ca})$$
$$+ 0.017(\text{Fe} + \text{Ni}) \qquad \text{IV. (14)}$$

and

$$^{38}Ar_c = 16.5(\text{Ca}) + (\text{Fe} + \text{Ni}) \qquad \text{IV. (15)}$$

where the elemental symbols represent the weight percent of the element in the sample. These production ratios are normalized to a class of stony meteorites called hypersthene chondrites, which have absolute production rates of:

$$P(^{21}Ne_c) \text{ (chondrites)} = 3.77 \times 10^{-9} \text{ cm}^3STPg^{-1}myr^{-1}$$

and

$$P(^{38}Ar_c) \text{ (chondrites)} = 5.26 \times 10^{-10} \text{ cm}^3STPg^{-1}myr^{-1}$$

(Mazor et al., 1970).

When the average hypersthene chondrite chemical composition in weight percent (Mason, 1965) is substituted into equations IV. (14) and IV. (15), the results are $^{21}Ne_c$ = 55.15 and $^{38}Ar_c$ = 45.14. Multiplying the absolute cosmogenic production rates of $P(^{21}Ne_c)$ (chondrites) and $P(^{38}Ar_c)$ (chondrites) by the average Odessa cosmic ray exposure age of 530 million years:

$$\frac{^{21}Ne_c \text{(graphite)}}{P(^{21}Ne_c) \text{ (chondrites)} \times 530 \text{ myr}} = \frac{0.29(S) + 0.017(Fe + Ni)}{55.15} \qquad \text{IV. (16)}$$

and

$$\frac{^{38}Ar_c \text{(graphite)}}{P(^{38}Ar_c) \text{ (chondrites)} \times 530 \text{ myr}} = \frac{(Fe + Ni)}{45.14} \quad . \qquad \text{IV. (17)}$$

Equation IV. (17) gives the iron plus nickel weight percentage in graphite as 1.71%. Substituting that result in equation IV. (16) gives the sulfur weight percentage in the graphite as 1.13%.

The ratio of the atomic weights of iron and sulfur is 1.75, so if troilite is the only trace mineral in the graphite, the ratio of their weight percents should also be 1.75. However, (1.71/1.13) = 1.51, so even assuming no metallic nickel-iron, the initial assumption of only troilite and nickel-iron impurities in the graphite phase is incorrect. Unless there is free sulfur in the graphite, to lower the derived sulfur content the abundance of $^{21}Ne_c$(graphite) requires trace abundances of any or all of the elements magnesium, aluminum, and silicon.

The addition of calcium would decrease the weight percentage of nickel-iron, so unless there was a substantial amount of magnesium, aluminum, and silicon, adding calcium would cause a poorer fit assuming no free sulfur. It should be noted that whatever the calcium content might be in the graphite sample, the maximum weight percentage of elements which can produce ^{38}Ar by spallation remains at 1.71% in this analysis. Since heavy elements such as nickel and iron are not unlikely to be present, this suggests the purity of the graphite sample is quite high.

The krypton data in the metal and graphite phases of Odessa resemble one another and the composition of the atmosphere closely. However, again there are ^{78}Kr and ^{80}Kr enrichments. The Deelfontein krypton measurements are reported as being within 10% of the atmospheric ratios for the metal and graphite phases, so the only possible differences

between the two meteorites might be at ^{78}Kr and ^{80}Kr.

The ^{82}Kr/^{84}Kr and ^{83}Kr/^{84}Kr ratios have atmospheric-solar wind values within experimental error, so neutron capture on bromine and selenium does not appear to have produced significant amounts of krypton in the graphite phase. This suggests that the light isotope enrichment seen in graphite might prove a good estimate of the composition of that component. Assuming the krypton data from the graphite inclusion to result from a two component mix of atmospheric-solar wind and the proposed light isotope (^{78}Kr and ^{80}Kr) rich krypton component, the ^{78}Kr/^{80}Kr ratio calculated for this light component is 0.375. Of course, this component is not necessarily the same one as that seen in the metal phase.

In both Odessa and Deelfontein the graphite phase has the greatest concentration of xenon. The graphite from Odessa resembles that of the metal phase, except here there are enrichments in the spallation produced isotopes ^{124}Xe, ^{126}Xe, and ^{128}Xe. Although the ^{129}Xe excess is only about one-fourth that seen in the troilite sample, since there is about four times as much xenon in the graphite, the concentrations of excess ^{129}Xe are approximately equal. This is somewhat unusual if the ^{129}Xe excess in graphite is due to in situ decay of ^{129}I since the iodine should be concentrated in the troilite. If the excess ^{129}Xe is not due to in situ decay of ^{129}I in the graphite, the most plausible interpretation is that the graphite phase trapped a primordial xenon component from a reservoir in which ^{129}I had decayed quantitatively.

The metal, troilite, and graphite phases of Odessa all seem enriched in ^{134}Xe, but only the metal phase also has a ^{136}Xe overabundance relative to atmospheric xenon. Since all the heavy isotope rich xenon components favor ^{136}Xe over ^{134}Xe, these data from the graphite and troilite inclusions are very puzzling.

V. CONCLUSIONS

A. General Results

The inert gas compositions of the meteorites analyzed were sur-
prisingly complex. The samples from meteorites known to have long cosmic
ray exposure ages tended to follow the predicted spallogenic patterns,
but where the spallogenic gas was not so overwhelming, it was possible to
see trends suggesting other inert gas sources. Mineral separates from
Odessa inclusions brought out prominent compositional differences in
side-by-side samples.

A number of conclusions can be reached with regard to all the
inert gases in these meteorites:

(a) All of the meteorites contain evidence of having a spallogenic
gas component. This is unsurprising, especially in helium, neon, and
argon. Since iron meteorites are composed of approximately 90% iron and
10% nickel, the interaction of galactic cosmic rays with the parent mete-
oroids will produce an abundance of those inert gases lighter than these
target elements. Cosmogenic krypton and xenon in the metal phase will be
the result of spallation reactions on the heavy trace elements. This
leads to a second general conclusion.

(b) The trace element abundances (both light, i.e. less than nickel-
iron, and heavy) and the siting of any sample are crucial to the cosmic ray
produced inert gas composition and concentration. Many of the smaller vari-
ations seen may be attributable to these two factors. Unfortunately, the

trace element abundances most likely to produce inert gases by spallation reactions are not well known in iron meteorites, especially for krypton and xenon. The amount of cosmic ray shielding each sample has had is also unknown.

(c) Due to the average cosmic ray exposure age of the present meteorites being significantly shorter than that of a random sample of iron meteorites, indications of non-spallogenic compositions may be seen which might otherwise have been obscured. This behavior tends to correlate with the exposure age in that those showing the greatest deviations from spallogenic compositions have the shortest exposure ages.

(d) The data from many of my samples indicate an atmospheric-like trapped gas component. It is not possible to definitively state whether or not this gas is primordial or has been introduced to the meteorite by contamination. There are instances where supporting evidence can be given for the primordial interpretation, but despite this and the experimental precautions taken, contamination can never be ruled out entirely as a means of at least providing some of the evolved "atmospheric" gas.

(e) Those meteorites which show anomalous behavior for one inert gas tend to be anomalous for the others as well. This is true not so much in the cases where a specific mechanism for producing the anomaly is known (i.e. ^{129}Xe from extinct ^{129}I), but where there is a general disagreement throughout the given gas with an expected gas composition such as solar wind or cosmogenic.

B. Metal Samples

1) Helium, Neon, and Argon

Although the main purpose of this project was to study krypton and xenon compositions in the metal phase of iron meteorites, the variations seen extended to the light inert gases as well. A significant difference exists between cosmogenic composition models for helium, neon, and argon and the data seen in the analyzed samples. The results point out the wide disparity of isotopic compositions and concentrations measured by different investigators of the same meteorite, and even the same investigator analyzing different samples of the same meteorite.

In helium the meteorites Babb's Mill, Braunau, Cedartown, and Sierra Gorda had the ^{3}He deficit seen previously in many iron meteorite metal samples. Braunau, Cedartown, and Sierra Gorda are all hexahedrites, a structural classification noted for commonly having this anomaly. One hexahedrite, Tombigbee River, did not follow this trend, although in previous analyses it had.

Neon data provide the most conformity to the predicted spallogenic ratios. Twelve of the 15 iron meteorite metal samples cluster around the cosmogenic ^{20}Ne/^{22}Ne and ^{21}Ne/^{22}Ne ratios. The Babb's Mill and Braunau neon data definitely indicate a solar wind and/or atmospheric admixed component with the spallogenic neon, but the errors in the measurements preclude a choice between the two components. Most remarkable is that the Cedartown neon data trend in the direction of a component

previously observed only in carbonaceous chondrites--pure ^{22}Ne.

Argon abundances were anomalously low in a number of meteorites relative to the concentrations expected from the helium and neon concentrations. The most plausible explanation appears to be that these samples with low argon concentrations contain an unusual amount of trace minerals and possibly a chondritic-like trapped light inert gas component. Again, the most anomalous meteorites (i.e. those having the highest ^{36}Ar/^{38}Ar ratios) were those with the shortest cosmic ray exposure ages, Babb's Mill and Braunau.

The only meteorite studied which did not have its cosmic ray exposure age previously determined was Edmonton (Kentucky). The data for this meteorite plot consistently with that of Tombigbee River for the light inert gas isotopes, so the prediction is that Edmonton will prove to have a similar exposure age of approximately 500 million years.

2) Krypton

Many of the iron meteorites have krypton data which is consistent with a mixture of solar wind-atmospheric krypton and spallogenic gas. However, about half the samples show excesses at ^{78}Kr, ^{80}Kr and possibly ^{82}Kr over that expected from such a mix. There are a number of alternative explanations for these anomalies:

(a) The light isotope enrichments seen in krypton are consistent with a two component mixing model of solar wind-atmospheric and spallo-genic krypton with a deficit of ^{83}Kr in the spallogenic component.

A ^{83}Kr deficit may be produced by a fluence of thermal neutrons on the order of 10^{21} neutrons/cm^2. This mechanism requires the irradiation take place prior to trapping the krypton in the sample, because neutron capture effects on other elements would cause more than four orders of magnitude more krypton than that measured if the irradiation occured in situ. Such high fluences of neutrons are generally associated with supernovae remnants.

(b) Assuming bromine abundances similar to those measured in iron meteorites and a flux of neutrons consistent with that expected from secondary spallation reactions, neutron capture over the cosmic ray exposure age of the meteorite on ^{79}Br and ^{81}Br can produce enrichments on the order of those seen in ^{80}Kr and ^{82}Kr. The ^{82}Se abundance and neutron capture cross section are too low to cause an anomaly in ^{83}Kr in the metal phase. However, this interpretation does not explain the observed ^{78}Kr enrichments, which are significant despite large errors.

(c) An alternative possibility is that the light krypton isotope (both ^{78}Kr and ^{80}Kr) excesses measured relative to a solar wind-atmospheric and spallogenic krypton mix are from trapped gas produced during nucleosynthesis deep in a massive star, specifically in the silicon burning shell. Theoretical calculations predict large over-production factors of ^{78}Kr and ^{80}Kr in this case, but it is not clear how such matter could have gotten into an iron meteorite metal sample.

3) Xenon

The conclusions which can be reached for the xenon data from the iron meteorite metal samples are perhaps the most important of this work:

(a) The majority of meteorites contain xenon compositions which may be most easily explained as a mixture of solar wind, atmospheric, and spallation xenon, precisely the same conclusion as that drawn for the krypton data. This is in itself a new result of this study, since prior investigators assumed only that atmospheric and cosmogenic xenon were present in iron meteorite metal samples.

Most samples have small ^{129}Xe excesses attributable to the decay of ^{129}I. Other xenon compositions were also seen in specific meteorites, as will be noted in the following results.

(b) Four meteorites, Babb's Mill, Cedartown, Dayton, and Odessa show evidence of having excesses at ^{134}Xe and ^{136}Xe due to fission xenon from ^{238}U or ^{244}Pu, or an admixture of the H-Xe component. These heavy isotope rich components had only been seen previously in mineral separate samples from iron meteorites.

(c) The Sierra Gorda meteorite is remarkable in having anomalies consistent with a mixture of solar wind, spallation, and s-Xe components. The s-Xe component had been deduced from the carbon-rich residue of a carbonaceous chondrite, a vastly different environment than a bulk meteorite sample. This evidence for an s-Xe like component is also a new result of this study.

(d) The Braunau meteorite is abnormal in that it contains a xenon component not hitherto seen in any meteorite, stony or iron. The xenon composition is most anomalous in having a large ^{128}Xe deficit relative to any known components.

4) Babb's Mill and Braunau

Two of the metal phase samples deserve further discussion. The Babb's Mill and Braunau samples had the highest ^{4}He/^{3}He, ^{20}Ne/^{22}Ne, and ^{36}Ar/^{38}Ar ratios of all the meteorites. Each of these ratios indicated the presence of a non-spallogenic light inert gas component. In krypton and xenon these two samples also had unique compositions.

Babb's Mill is striking in its krypton composition in that it showed little or no evidence of an excess or spallation component at any isotope. Thus its composition mimics the atmospheric and solar wind values closely. It is plausible that this is its primordial composition since it has an extremely short cosmic ray exposure age. Babb's Mill also has distinctive xenon data which follow the pattern expected for a mixture of solar wind gas with a heavy isotope rich (^{134}Xe and ^{136}Xe) component. Again the data indicate very little spallation produced gas.

The inert gas data from Braunau suggest it trapped gas from a reservoir which had undergone a strong neutron irradiation. This could explain the observed underabundance of ^{3}He and its odd krypton and xenon compositions. The required neutron fluences are very large, so this irradiation cannot be an _in situ_ production mechanism. The neutron capture

cross sections of ^{128}Xe, ^{129}Xe, ^{130}Xe, ^{131}Xe, and ^{132}Xe permit the tentative hypothesis of neutron capture as the reason for Braunau's anomalous composition, but the suitable pre-irradiation composition is not an obvious one. An initial composition resembling that of the s-process seed in a massive star is promising, but requires further investigation.

C. Odessa Inclusions

1) Troilite

The data from the Odessa inclusions provide an illuminating contrast in inert gas compositions. The helium, neon, and argon in the troilite phase are dominated by spallation, but the neon data are indicative of a possible component of pure ^{22}Ne. Overall, the spallation spectrum seen in the troilite is slightly different than that in the metal due to small changes in the spallation target element abundances. In krypton the troilite phase has positive anomalies at ^{80}Kr, ^{82}Kr, and ^{83}Kr relative to the atmospheric composition. These enhancements are consistant with neutron capture on ^{79}Br, ^{81}Br, and ^{82}Se, respectively, where the neutrons are provided from secondary spallation reactions during the cosmic ray exposure age of the meteorite. The ^{78}Kr data were unreliable in the troilite phase, presumably due to hydrocarbon interference.

In xenon spallation is prominent in the troilite as is an excess at ^{129}Xe. Since iodine is expected to be enriched in the troilite phase, extinct ^{129}I appears to be the cause of the ^{129}Xe excess, although neutron capture on ^{128}Te may be partly responsible.

2) Graphite

Although spallation can produce helium in pure graphite, neon and argon spallation components can only be derived from impurities in that phase. Because of this, trapped components were clearly evident in

the neon and argon data from the graphite inclusion. These two inert gases were consistent with a two component mix of trapped solar wind and spallogenic gas, but the argon data required a small atmospheric component to account for the ^{40}Ar concentration. A comparison of the spallogenic neon and argon components allows an estimate of the trace mineral concentrations in the graphite phase.

In krypton the graphite data resemble that of the metal phase and the atmospheric composition, except at ^{78}Kr and ^{80}Kr. This permits an estimate of the light krypton component composition: ^{78}Kr/^{80}Kr = 0.375.

In xenon, despite the ^{129}Xe excess being smaller in the graphite phase than in the troilite, because the graphite has a greater concentration of xenon, the total concentrations of excess ^{129}Xe are approximately the same. This could be indicative of the Odessa inclusions having a primordial trapped xenon component with a ^{129}Xe enrichment. If all three phases of Odessa derived their inert gases from a reservoir where there was an excess of ^{129}Xe, the graphite would trap a primordial composition enriched in ^{129}Xe beyond that expected from its iodine content because xenon has its greatest concentration in graphite. Thus essentially all the ^{129}Xe in the graphite would not have arisen from in situ decay of ^{129}I, whereas the reverse would be true in the troilite phase.

All three phases of Odessa have a positive ^{134}Xe anomaly relative to atmospheric xenon, but only the metal phase also has a ^{136}Xe excess consistent with that expected from a heavy isotope rich component. Possibly the ^{134}Xe excess seen could also be derived from a primordial reservoir.

D. Summary

While there is evidence of non-spallogenic gas components in virtually all the meteorite samples, there are anomalies within the metal phase of Babb's Mill, Braunau, and Sierra Gorda which strongly suggest that iron meteorites do contain trapped, primordial inert gases. The data from the Braunau sample in particular are inconsistent with a mix of spallogenic gas and gas of either atmospheric or solar composition. At least these three meteorites should have further, more precise, determinations made of their inert gas compositions.

VI. REFERENCES

Alexander E. C. Jr., Bennet J. H. and Manuel O. K. (1968) On noble gas anomalies in the Great Namaqualand Troilite. Z. Naturforsch. 23a, 1266-1271.

Alexander E. C. Jr., Lewis R. S., Reynolds J. H. and Michel M. C. (1971) Plutonium-244: confirmation as an extinct radioactivity. Science 172, 837-840.

Alexander E. C. Jr. and Manuel O. K. (1967) Isotopic anomalies of krypton and xenon in Canyon Diablo graphite. Earth Planet. Sci. Lett. 2, 220-224.

Alexander E. C. Jr. and Manuel O. K. (1968) Xenon in the inclusions of Canyon Diablo and Toluca iron meteorites. Earth Planet. Sci. Lett. 4, 113-117.

Anders E. and Heymann D. (1969) Elements 112 to 119: were they present in meteorites? Science 164, 821-823.

Arnold J. R., Honda M. and Lal D. (1961) Record of cosmic-ray intensity in meteorites. J. Geophys. Res. 66, 3519-3531.

Arrol W. J., Jacobi R. B. and Paneth F. A. (1942) Meteorites and the age of the solar system. Nature 149, 235-238.

Basford J. R., Dragon J. C., Pepin R. O., Coscio M. R. Jr. and Murthy V. R. (1973) Krypton and xenon in lunar fines. Proc. Lunar Sci. Conf. 4th, 1915-1955.

Bate G. L., Potratz H. A. and Huizenga J. R. (1958) Thorium in iron meteorites: a preliminary investigation. Geochim. Cosmochim. Acta 14, 118-125.

Bauer C. A. (1947) Production of helium in meteorites by cosmic radiation. Phys. Rev. 72, 354-355.

Bauer C. A. (1948a) The absorption of cosmic radiation in meteorites. Phys. Rev. 74, 225-226.

Bauer C. A. (1948b) Rate of production of helium in meteorites by cosmic radiation. Phys. Rev. 74, 501-503.

Bauer C. A. (1963) The helium contents of metallic meteorites. J. Geophys. Res. 68, 6043-6057.

Begemann F. (1965) Edelgasmessungen an Eisenmeteoriten und deren Einschlussen. Z. Naturforsch. 20a, 950-960.

Black D. (1972) On the origins of trapped helium, neon and argon isotopic variations in meteorites II. Carbonaceous chondrites. Geochim. Cosmochim. Acta 36, 377-394.

Bogard D. D., Huneke J. C., Burnett D. S. and Wasserburg G. J. (1971) Xe and Kr analyses of silicate inclusions from iron meteorites. Geochim. Cosmochim. Acta 35, 1231-1254.

Buchwald V. F. (1966) The iron-nickel-phosphorus system and the structure of iron meteorites. Acta Polytech. Scand.,Chem. Incl. Met. Ser. 51, 1-46.

Buchwald V. F. (1975) Handbook of Iron Meteorites. University of California Press, Los Angeles, California.

Cameron A. G. W. (1973) Abundances of the elements in the solar system. Space Sci. Rev. 15, 121-146.

Cameron A. G. W. and Truran J. W. (1977) The supernova trigger for formation of the solar system. Icarus 30, 447-461.

Clarke W. B. and Thode H. G. (1964) The isotopic composition of krypton in meteorites. J. Geophys. Res. 69, 3673-3679.

Cobb J. C. (1966) Iron meteorites with low cosmic ray exposure ages. Science 151, 1524.

Dodd R. T. (1969) Metamorphism of the ordinary chondrites: A review. Geochim. Cosmochim. Acta 33, 161-203.

Dziczkaniec M. (1980) Isotopic anomalies from nuclear processes in stars. Ph. D. Dissertation, Rice University.

Eberhardt P., Eugster O. and Marti K. (1965) A redetermination of the isotopic composition of atmospheric neon. Z. Naturforsch. 20a, 623-624.

Eberhardt P., Geiss J., Graf H., Grögler N., Krähenbühl U., Schwarzmüller J., Schwaller H. and Stettler A. (1970) Trapped solar wind noble gases, exposure age and K/Ar age in Apollo 11 lunar fine material. Proc. Apollo 11 Lunar Sci. Conf., 1037-1070.

Eberhardt P., Geiss J., Graf H., Grögler N., Mendia M. D., Mörgeli M., Schwaller H. and Stettler A. (1972) Trapped solar wind noble gases in Apollo 12 lunar fines 12001 and Apollo 11 breccia 10046. Proc. Lunar Sci. Conf. 3rd, 1821-1856.

Eugster O., Eberhardt P. and Geiss J. (1967) Kr and Xe isotopic composition in three carbonaceous chondrites. Earth Planet. Sci. Lett. 3, 249-257.

Eugster O., Eberhardt P. and Geiss J. (1969) Isotopic analyses of krypton and xenon in fourteen stone meteorites. J. Geophys. Res. 74, 3874-3896.

Fireman E. L. and DeFelice J. (1968) Rare gases in phases of the Deelfontein meteorite. J. Geophys. Res. 73, 6111-6116.

Fisher D. E. (1967) Cosmogenic tritium problem in iron meteorites. J. Geophys. Res. 72, 1351-1354.

Fisher D. E. and Schaeffer O. A. (1960) Cosmogenic nuclear reactions in iron meteorites. Geochim. Cosmochim. Acta 20, 5-14.

Geiss J., Buehler F., Cerutti H., Eberhardt P. and Filleux Ch. (1972) Solar wind composition experiment. Apollo 16 Preliminary Science Report, Section 14, NASA SP-315.

Gentner W. and Zähringer J. (1957) Argon und Helium als Kernreaktionsproducte in Meteoriten. Geochim. Cosmochim. Acta 11, 60-71.

Goldstein J. I. and Short J. M. (1967) The iron meteorites, their thermal history and parent bodies. Geochim. Cosmochim. Acta 31, 1733-1770.

Goles G. G. and Anders E. (1962) Abundances of iodine, tellurium, and uranium in meteorites. Geochim. Cosmochim. Acta 26, 723-737.

Hennecke E. W. and Manuel O. K. (1977) Argon, krypton and xenon in iron meteorites. Earth Planet. Sci. Lett. 36, 29-43.

Herzog G. F., Lipschutz M. E., Jain A. V. and Rodman T. E. (1976) Noble gases and shock effects in the Odessa octahedrite. J. Geophys. Res. 81, 3583-3586.

Heymann D. (1967) On the origin of hypersthene chondrites: ages and shock-effects of black chondrites. Icarus 6, 189-221.

Heymann D. and Dziczkaniec M. (1980) A first roadmap for kryptology. Submitted to Proc. Lunar Planet. Sci. Conf. XI.

Heymann D. M., Lipschutz E., Nielson B. and Anders E. (1966) Canyon Diablo meteorite: Metallographic and mass spectrometric study of 56 fragments. J. Geophys. Res. 71, 619-641.

Hintenberger H., Schultz L., Wänke H. and Weber H. (1967) Helium und Neonisotope in Eisenmeteoriten und der Tritiumverlust in Hexaedriten. Z. Naturforsch. 22a, 780-787.

Hintenberger H., Schultz L. and Weber H. (1969) Rare gases in the iron and in the inclusions of the Campo del Cielo meteorite, El Taco. In Meteorite Research, (editor P. Millman). Reidel, Dordrecht, 895-900.

Hintenberger H. and Wänke H. (1964) Helium und Neonisotope in Eisenmeteoriten. Z. Naturforsch. 19a, 210-218.

Hohenberg C. M., Munk M. N. and Reynolds J. H. (1967) Spallation and fissiogenic xenon and krypton from stepwise heating of the Pasamonte achondrite; the case for extinct plutonium-244 in meteorites; relative ages of chondrites and achondrites. J. Geophys. Res. 72, 3139-3177.

Huntley H. E. (1948) Production of helium by cosmic rays. Nature 161, 356.

Kaiser W. and Zähringer J. (1968) K/Ar age determinations of iron meteorites IV. New results with refined experimental procedures. Earth Planet. Sci. Lett. 4, 84-88.

Kelly W. R. and Larimer J. W. (1977) Chemical fractionations in meteorites VIII. Iron meteorites and the cosmochemical history of the metal phase. Geochim. Cosmochim. Acta 41, 93-111.

Kiesl W. and Hecht F. (1969) Meteorites and the high-temperature origin of terrestrial planets. In Meteorite Research, (editor P. Millman). Reidel, Dordrecht, 67-74.

Kolesnikov E. M., Lavrukhina A. K., Fisenko A. V. and Levsky L. K. (1972) Radiation ages of different fragments of the Sikhote-Alin meteorite fall. Geochim Cosmochim. Acta 36, 573-576.

Krummenacher D., Merrihue C. M., Pepin R. O. and Reynolds J. H. (1962) Meteoritic krypton and barium versus the general isotopic anomalies in meteoritic xenon. Geochim. Cosmochim. Acta 26, 231-249.

Kuroda P. K. (1960) Nuclear fission in the early history of the earth. Nature 187, 36-38.

Lamb S. A., Howard W. M., Truran J. W. and Iben I. Jr. (1977) Neutron-capture nucleosynthesis in the helium-burning cores of massive stars. Astrophys. J. 217, 213-221.

Lewis R. S., Srinivasan B. and Anders E. (1975) Host phase of a strange Xe component in Allende. Science 190, 1251-1262.

Libby L. M., Libby W. F. and Runcorn S. K. (1979) The possibility of superheavy elements in iron meteorites. Nature 278, 613-617.

Lipschutz M. E., Signer P. and Anders E. (1965) Cosmic ray exposure ages of iron meteorites by the $^{21}Ne/^{26}Al$ method. J. Geophys. Res. 70, 1473-1489.

Mann D. P., Watson W. W., Chrien R. E., Zimmerman R. L. and Schwartz R. B. (1959) Total neutron cross section of xenon and krypton. Phys. Rev. 116, 1516-1520.

Manuel O. K., Hennecke E. W. and Sabu D. D. (1972) Xenon in carbonaceous chondrites. Nature Phys. Sci. 240, 99-101.

Marti K. (1967) Isotopic compositions of trapped krypton and xenon in chondrites. Earth Planet. Sci. Lett. 3, 243-248.

Marti K., Eberhardt P. and Geiss J. (1966) Spallation, fission, and neutron capture anomalies in meteoritic krypton and xenon. Z. Naturforsch. 21a, 398-413.

Martin G. R. (1953) The origin of meteoritic helium and the age of meteorites. Geochim. Cosmochim. Acta 3, 288-309.

Mason B. (1965) The chemical composition of olivine-bronzite and olivine-hypersthene chondrites. American Museum Novitates No. 2223.

McCorkell R. H., Fireman E. L., D'Amico J. and Thompson S. O. (1968) Radioactive isotopes in Hoba West and other iron meteorites. Meteoritics 4, 113-122.

Meier F. O., Jungck M. H. A. and Eberhardt P. (1980) Evidence for pure neon-22 in Orgueil and Murchison. Lunar Planet. Sci. Conf. XI. (abstract), 723-725.

Morgan J. W. (1971) Uranium. In Handbook of Elemental Abundances in Meteorites, (editor B. Mason). Gordon and Breach, 529-548.

Munk M. N. (1967a) Spallation neon, argon, krypton, and xenon in an iron meteorite. Earth Planet. Sci. Lett. 2, 301-309.

Munk M. N. (1967b) Neon, argon, krypton, and xenon compositions of the Misteca and Carbo iron meteorites. Earth Planet. Sci. Lett. 3, 133-138.

Nier A. O. (1950) A redetermination of the relative abundances of the isotopes of neon, krypton, rubidium, xenon and mercury. Phys. Rev. 79, 450-454.

Nyquist L. E., Huneke J. C., Funk H. and Signer P. (1972) Thermal release characteristics of spallogenic He, Ne, and Ar from the Carbo iron meteorite. Earth Planet. Sci. Lett. 14, 207-215.

Paneth F. A., Reasbeck P. and Mayne K. I. (1953) Production by cosmic rays of helium-3 in meteorites. Nature 172, 200-201.

Pelly I. Z. and Lipschutz M. E. (1971) Selenium. In Handbook of Elemental Abundances in Meteorites, (editor B. Mason). Gordon and Breach, 271-278.

Pepin R. O. and Phinney D. (1980) Components of xenon in the solar system. Submitted to Moon and Planets.

Podosek F. A. (1978) Isotopic structures in solar system materials. Ann. Rev. Astron. Astrophys. 16, 293-334.

Podosek F. A., Huneke J. C., Burnett D. S. and Wasserburg G. J. (1971) Isotopic composition of xenon and krypton in the lunar soil and in the solar wind. Earth Planet. Sci. Lett. 10, 199-216.

Reasbeck P. and Mayne K. I. (1955) Cosmic radiation effects in meteorites. Nature 176, 733-734.

Reed G. W. Jr. (1971) Bromine. In Handbook of Elemental Abundances in Meteorites, (editor B. Mason). Gordon and Breach, 279-284.

Reynolds J. H. (1956) High sensitivity mass spectrometer for noble gas analysis. Review of Scientific Instruments 27, 928-934.

Reynolds J. H. (1960) Determination of the age of the elements. Phys. Rev. Lett. 4, 8-10.

Reynolds J. H., Merrihue C. M. and Pepin R. O. (1962) Extinct radioactivity and primordial rare gases in iron meteorites (abstract). Bull. Am. Phys. Soc. 7, 35.

Rowe M. W., Bogard D. D., Brothers C. E. and Kuroda P. K. (1965) Cosmic-ray-produced xenon in meteorites. Phys. Rev. Lett. 15, 843-845.

Rowe M. W. and Kuroda P. K. (1965) Fissiogenic xenon from the Pasamonte meteorite. J. Geophys. Res. 70, 709-714.

Rudstam G. (1966) Systematics of spallation yields. Z. Naturforsch. 21a, 1027-1041.

Schaeffer O. A. and Fisher D. E. (1959) Cosmogenic noble gases in the Washington County meteorite. Nature 183, 660-661.

Schaeffer O. A. and Zähringer J. (1960) Helium, neon and argon isotopes in some iron meteorites. Geochim. Cosmochim. Acta 19, 94-99.

Schultz L. (1967) Tritium loss in iron meteorites. Earth Planet. Sci. Lett. 2, 87-89.

Schultz L., Funk H., Nyquist L. and Signer P. (1971) Helium, neon and argon in separated phases of iron meteorites. Geochim. Cosmochim. Acta 35, 77-88.

Schultz L., Funk H. and Signer P. (1971) On the radiogenic argon in iron meteorites. Chemie der Erde 30, 297-304.

Schultz L. and Hintenberger H. (1967) Edelgasmessungen an Eisenmeteoriten. Z. Naturforsch. 22a, 773-779.

Schultz L., Huneke J. C., Nyquist L. E. and Signer P. (1969) Spallogenic rare gases in taenite separated from iron meteorites. In Meteorite Research, (editor P. Millman). Reidel, Dordrecht, 887-894.

Scott E. R. D. (1978) Primary fractionation of elements among iron meteorites. Geochim. Cosmochim. Acta 42, 1447-1458.

Scott E. R. D. and Wasson J. T. (1975) Classification and properties of iron meteorites. Rev. Geophys. Space Phys. 13, 527-546.

Signer P. and Nier A. O. C. (1960) The distribution of cosmic-ray-produced rare gases in iron meteorites. J. Geophys. Res. 65, 2947-2964.

Signer P. and Nier A. O. C. (1962) The measurement and interpretation of rare gas concentrations in iron meteorites. In Researches on Meteorites, (editor C. Moore). Wiley, 7-35.

Srinivasan B. and Anders E. (1978) Noble gases in the Murchison meteorite: Possible relics of s-process nucleosynthesis. Science 201, 51-56.

Stauffer H. and Honda M. (1962) Cosmic ray produced stable isotopes in iron meteorites. J. Geophys. Res. 67, 3503-3512.

Tilles D. (1962) Primordial gas in the Washington County meteorite. J. Geophys. Res. 67, 1687-1689.

Vilcsek E. and Wänke H. (1962) Cosmic ray exposure ages and terrestrial ages of stone and iron meteorites derived from ^{36}Cl and ^{39}Ar measuremnts, in Radioactive Dating (International Atomic Energy Agency, Athens).

Voshage H. (1967) Bestrahlungsalter und Herkunft der Eisenmeteorite. Z. Naturforsch. 22a, 477-506.

Voshage H. (1978) Investigations on cosmic-ray-produced nuclides in iron meteorites, 2. New results on ^{41}K/^{40}K-^{4}He/^{21}Ne exposure ages and the interpretation of age distributions. Earth Planet. Sci. Lett. 40, 83-90.

Voshage H. and Feldman H. (1978) Investigations on cosmic-ray-produced nuclides in iron meteorites, 1. The measurement and interpretation of rare gas concentrations. Earth Planet. Sci. Lett. 39, 25-36.

Wetherill G. W. (1953) Spontaneous fission yields from uranium and thorium. Phys. Rev. 92, 907-912.